



**HAL**  
open science

# Polarisation of quarks and gluons inside the nucleon

Vincent Andrieux

► **To cite this version:**

Vincent Andrieux. Polarisation of quarks and gluons inside the nucleon. High Energy Physics - Experiment [hep-ex]. Université Paris Sud - Paris XI, 2014. English. NNT : 2014PA112244 . tel-01126893

**HAL Id: tel-01126893**

**<https://theses.hal.science/tel-01126893>**

Submitted on 6 Mar 2015

**HAL** is a multi-disciplinary open access archive for the deposit and dissemination of scientific research documents, whether they are published or not. The documents may come from teaching and research institutions in France or abroad, or from public or private research centers.

L'archive ouverte pluridisciplinaire **HAL**, est destinée au dépôt et à la diffusion de documents scientifiques de niveau recherche, publiés ou non, émanant des établissements d'enseignement et de recherche français ou étrangers, des laboratoires publics ou privés.



UNIVERSITÉ PARIS-SUD

ÉCOLE DOCTORALE 517 : PARTICULES-NOYAUX-COSMOS

LABORATOIRE CEA/DSM/IRFU: SERVICE DE PHYSIQUE NUCLÉAIRE

DISCIPLINE : PHYSIQUE HADRONIQUE

THÈSE DE DOCTORAT

Soutenue le 30 septembre 2014 par

**M. Vincent ANDRIEUX**

**Polarisation of quarks and gluons  
inside the nucleon**

**Composition du jury :**

Directeur de thèse :	Mme Fabienne KUNNE	Docteur (CEA-Saclay, Fr.)
Président du jury :	M. Claude VALLÉE	Directeur de recherche (CNRS de Marseille, Fr.)
Rapporteurs :	M. Abhay DESHPANDE	Professeur (Stony brook, USA)
	M. Werner VOGELSANG	Professeur (Tuebingen University, De.)
Examineurs :	M. Etienne AUGÉ	Professeur (LAL-Orsay, Fr.)
	M. Franco BRADAMANTE	Professeur (Universita' degli studi di Trieste, It.)



---

To my father

---



# Acknowledgements

My first words go to my jurors that I sincerely thank for their participation to my thesis defence, it was an honour for me. I thank DR Claude VALLÉE for accepting to preside over the members of my jury of viva voce and the interest he showed in my research. I want to thank warmly my two referees, PROF. Abhay DESHPANDE and PROF. Werner VOGELSANG, for their very attentive reading of my manuscript and their detailed reports. I assure PROF. Franco BRADAMANTE and PROF. Etienne AUGÉ of my gratitude for counting them among the members of my jury. Finally, I want to especially thank DR Fabienne KUNNE for overseeing my work for these three years of PhD. I am grateful for her trust and her support. She gave me a large degree of independence in my way of dealing with my research topic but was also always present to ask the relevant questions. I am also thankful for the consideration she gave to my opinions concerning the analyses performed within the group and her encouragement in my teaching activities during the laboratory work of the master students.

I want to thank the former head of service and his assistant, DR Michel GARÇON and DR Françoise AUGER, for kindly welcoming me in the service of nuclear physics. I also cordially thank DR Héloïse GOUTTE and DR Jacques BALL for their interest in my work and my development as a researcher and the confidence they showed to me on several occasions.

This work also benefited from wise advice of all the members of the COMPASS group of Saclay. I want to thank first DR Yann BEDFER for the valuable discussions I had with him. I am happy he shared his great scientific knowledge and his expertise on the COMPASS spectrometer with me and it was a reward for me to work with him. I also want to express my gratitude to DR Claude MARCHAND for his involvement in my thesis that he has followed with care, and his great support. Despite his strong personality, he has a jovial character and it was a pleasure to work with him. I also highly appreciated my interaction with DR Damien NEYRET. His intuitive approach of physics and his external vision of my work was always of great interest to me. I thank him for that, and for many other practicalities. I also thank DR Stéphane PLATCHKOV for his interest in my work and his comments concerning this manuscript, and DR Étienne BURTIN for the time he gave me to discuss the measurement of the beam polarisation. I am also grateful to DR Nicole D'HOSE and DR Andrea FERRERO for their support and encouragement. I want to express my gratitude to DR Alain MAGNON for his mindfulness of my work, for our discussion at CERN and for his devotion to the COMPASS spectrometer. I cannot forebear to mention the help I received from DR Luigi CAPOZZA, who looked after me when I joined the COMPASS collaboration, DR Heiner WOLLNY, who taught me with kindness his skills in studying the stability of the spectrometer, and DR Erin SEDER who, just arrived, accepted to review my thesis and shared her experience in polarised target. May they all be grandly thanked for that.

Many thanks go out to all the members of the nuclear physics service but I wish to particularly thank DR Stefano PANEBIANCO who was my tutor in the service. He always took

time to discuss with me about my work, to help me elaborate my thoughts and to provide advice. He cared about my scientific development as well as my physical integration within the service. I acknowledge him for all he has done for me. I also want to thank DR Hervé MOUTARDE for taking time to answer with indulgence my naive questions and DR Sébastien PROCUREUR for his curiosity in my work and the time he gave me. Finally, I am grateful to DR Maxence VANDENBROUCKE for his advice and his support.

I thank all members of the COMPASS collaboration but in particular a few people who contributed to the outcome of the results presented in this thesis. My first thoughts go to PROF. Eva KABUSS, who chaired the group meetings. I thank her for following with care my work and for guiding and supporting me in the analysis. I am also very grateful to DR Marcin STOLARSKI, who makes you learn greatly on physics, for his valued remarks on the analysis. I am thankful for the instructive discussion I exchanged with PROF. Barbara BADELEK and I want to assure her about my gratitude. This work could not have been possible without the help of PROF. Roland WINDMOLDERS who provided me the fitting code and explained it to me conscientiously. May he be thank for that. I thank DR Lau GATIGNON for his explanations on the simulation of the beam line and his Monte-Carlo productions to determine the beam polarisation. Last but not the least, I warmly thank my two fellow students, MR Malte WILFERT and MR Artem IVANOV, for the friendly and solid atmosphere of work we had and their valuable participation to this analysis.

I gratefully acknowledge PROF. Dimiter D. STAMENOV and PROF. Marco STRATMANN for their comments on my results and their wise advice.

I also deeply thank the several people who took care of me in more practical aspects. I am thankful to MRS Danielle CORET. I want to assure MRS Isabelle RICHARD and MRS Valérie POYETON about my great gratitude for their help, for their kindness, and the enjoyable moments I had with them. I am grateful to MRS Anne LISSAJOUX for the attentions she payed and her kindness. Finally, I also want to thank MR Gilles TRICOCHÉ for his IT support and MR Patrick CHAMPION for his technical support.

I cannot forget to thank all the members of the technique departments and above all those from IRFU (SEDI, SIS and SACM) for their technical achievements, without which the data I analysed would not have been recorded.

I also want to warmly thank some of my fellows from Saclay to whom I had very fruitful discussion and great support. Thank you, DR Lucie GRENTE, DR Florian THIBAUD, DR Antoine COLLIN and DR Quiela CURIÉL for the great moments I had with you. I also thank DR Eric FUCHEY, and MR Maxime LEVILLAIN and MR Maxime PEQUIGNOT to whom I also wish good luck for the future.

I finally want to express my deep and invaluable gratitude for the support I received from my family and especially from my mother Marinette, my sister Nathalie, my brother-in-law Manuel and my uncle Guy. I also want to warmly thank my friends, Alice, Manuel, Pauline, Thalia, David and Christina.

I want to finish these acknowledgements by thanking DR Claire MEYER for her trust and belief in my potential and who, I think, initialised my path to here.

# Contents

<b>Introduction</b>	<b>1</b>
<b>1 Nucleon spin structure</b>	<b>3</b>
1.1 Deep inelastic scattering . . . . .	3
1.1.1 DIS cross-section and nucleon structure functions . . . . .	5
1.1.2 Virtual-photon-nucleon scattering . . . . .	5
1.2 Physical interpretation of structure functions . . . . .	7
1.2.1 Parton model . . . . .	7
1.2.2 QCD improved parton model . . . . .	9
1.2.3 Parton distribution functions . . . . .	10
1.3 Operator product expansion and spin sum rules . . . . .	12
1.3.1 Ellis-Jaffe sum rule SU(3) . . . . .	13
1.3.2 Bjorken sum rule SU(2) . . . . .	14
1.4 COMPASS new $g_1^p$ proton spin structure function data at 200 GeV . . . . .	15
<b>2 The COMPASS experiment</b>	<b>17</b>
2.1 Polarised beam . . . . .	17
2.2 Polarised target . . . . .	20
2.3 Spectrometer . . . . .	22
2.3.1 Tracking detectors . . . . .	24
2.3.2 Particle identification . . . . .	27
2.4 Data recording . . . . .	27
2.4.1 Trigger system . . . . .	27
2.4.2 Data acquisition system . . . . .	31
2.4.3 Event reconstruction . . . . .	31
<b>3 Extraction of spin asymmetries and spin structure function of the proton</b>	<b>33</b>
3.1 Stability of the apparatus . . . . .	33
3.1.1 Identification of bad spills . . . . .	33
3.1.2 Run by run stability . . . . .	34
3.1.3 Data grouping . . . . .	36
3.2 Target position . . . . .	36
3.3 Target filling . . . . .	37
3.4 Data selection . . . . .	38
3.5 Computation of the spin asymmetry . . . . .	40
3.5.1 Intuitive Asymmetry extraction . . . . .	42
3.5.2 Second order weighting method . . . . .	42
3.5.3 Radiative corrections . . . . .	43
3.5.4 $^{14}\text{N}$ polarisation correction . . . . .	44
3.6 Systematic studies: Search for biases and false asymmetries . . . . .	45

3.6.1	Estimates based on a Monte-Carlo simulation . . . . .	45
3.6.2	Estimates based on real data . . . . .	47
3.6.3	External contributions . . . . .	53
3.6.4	Summary and calculation of the systematic error . . . . .	54
3.7	Results on the longitudinal spin structure of the proton . . . . .	57
3.7.1	Double spin asymmetry $A_1^p$ . . . . .	57
3.7.2	The proton spin dependent structure function $g_1^p$ . . . . .	61
<b>4</b>	<b>NLO QCD analysis: Extraction of polarised PDFs and Bjorken sum rule</b>	<b>63</b>
4.1	NLO QCD fits . . . . .	63
4.1.1	Method . . . . .	64
4.1.2	Uncertainties affecting the QCD fit . . . . .	68
4.1.3	Results and conclusions from the QCD fits of world data . . . . .	75
4.1.4	Comparison of $\Delta g$ from the NLO QCD fits to direct measurements . . . . .	80
4.1.5	Comparison of the present NLO QCD fits to other global QCD analysis . . . . .	81
4.1.6	Further steps for QCD analysis . . . . .	83
4.2	Bjorken sum rule . . . . .	84
4.2.1	$Q^2$ evolution and data combination . . . . .	85
4.2.2	Fit of $g_1^{NS}$ . . . . .	85
4.2.3	Extraction of $g_A/g_V$ from the fit . . . . .	86
4.2.4	Extraction of $g_A/g_V$ from the data . . . . .	87
4.2.5	Comparison of the Bjorken sum rule to other analysis . . . . .	89
4.3	Key information of the chapter . . . . .	90
	<b>Conclusion</b>	<b>91</b>
	<b>Bibliography</b>	<b>100</b>
	<b>A Influence of <math>F_1</math> on NLO QCD fit</b>	<b>101</b>
	<b>B QCD fits parameters</b>	<b>103</b>

# Introduction

In 1922, the Stern-Gerlach experiment, built to test the Bohr-Sommerfeld hypothesis, highlighted a surprising result concerning the space of states of the electron. Electrons behave as if they had an intrinsic angular-momentum. In 1926, Goudsmit and Uhlenbeck introduced a new quantum number to describe those states: the concept of spin was born. Nucleons (proton and neutron), like the electrons, are spin-1/2 particles and considered to be elementary particles.

As time went by, numerous “elementary” particles sensitive to the strong force (hadrons) were discovered ( $\sim 100$ ), while the number of leptons (particles insensitive to the strong force) remained very small (nowadays, only 6 are known). This fact suggested an underlying layer of more fundamental particles. Gell-Mann evoked the idea in 1964 that the hadrons were composite particles made out of quarks. However, the existence of gluons as vector bosons of the strong interaction had to be postulated to explain the apparent violation of the Pauli exclusion principle in the  $\Delta^{++}$  hadron. That was the emergence of the Quantum ChromoDynamics (QCD).

The quarks are spin 1/2 particles of different flavours. Currently, six flavours are known: up ( $u$ ), down ( $d$ ), strange ( $s$ ), charm ( $c$ ), top ( $t$ ) and bottom ( $b$ ). They are electrically charged and the  $u$ ,  $c$  and  $t$  quarks carry a  $+2/3 \cdot e$  charge whereas the  $d$ ,  $s$  and  $b$  quarks carry a  $-1/3 \cdot e$ .

In the quark model, all the hadrons are described by either a three-quark combination (the baryons) or a quark-antiquark combination (the mesons). The proton in this case is written as a  $uud$  state that gives a  $+1 \cdot e$  electrical charge and a spin 1/2 using the  $SU(2)_{spin}$  algebra. Thus the quark polarisation,  $\Delta\Sigma$  (fraction of the proton spin carried by the quarks), is expected in this model to be 1 or 0.75 if relativistic effects are taken into account.

The experimental study of nucleon spin structure was initialised by E130 at SLAC (*Stanford Linear Accelerator Center*) in the early 1980’s and followed by EMC (*European Muon Collaboration*) at CERN (*Centre Européen de Recherche Nucléaire*) in the mid 1980’s, via measurements of polarised deep inelastic scattering. The latter derived  $\Delta\Sigma = 0.12 \pm 0.09 \pm 0.14$  from an estimation of the first moment of the proton spin structure function  $\Gamma_1^p$ . Such a small value of  $\Delta\Sigma$ , compatible with zero, was completely unexpected. The smallest prediction, derived from the Ellis-Jaffe sum rule, gives  $\Delta\Sigma_{E-J} = 0.58$ . This was at the origin of the so-called “spin crisis”. It opened a new era of spin physics and an enthusiasm to find out what the nucleon spin is made up of. The EMC results have been confirmed with a better accuracy by several other experiments using different facilities and experimental techniques. However, one of the limitations in this derivation is the evaluation of the integral contribution to  $\Gamma_1^p$  outside the measured range, especially at low  $x$  values.

In a more general approach, the spin of the nucleon can also be carried by gluons and angular momenta of quarks and gluons:

$$\frac{1}{2} = \frac{1}{2}\Delta\Sigma + \Delta G + L_q + L_g.$$

Currently, experimental efforts are put on all terms but the present analysis concentrates on the first two terms,  $\Delta\Sigma$  and  $\Delta G$  (fraction of the proton spin carried by the gluons). COMPASS

contributes to these efforts and had a specific data taking campaign in 2011 with a polarised muon beam at 200 GeV. With the world's highest energy polarised muon beam, COMPASS extends the measured range in addition to contributing to improving statistical precision. The results obtained with these new data are presented in this thesis as follows.

Chapter 1: The physics framework and motivations for this work are introduced. This includes a brief description of the neutral current deep inelastic scattering reaction (DIS) as well as definitions of the physical variables used in this manuscript. Structure functions, which describe the internal content of the proton, are also introduced in this chapter along with their physical interpretation in theoretical models. The Ellis-Jaffe SU(3) and Bjorken SU(2) sum rules and their role in highlighting the “spin crisis” are also discussed in detail.

Chapter 2. An overview of the experimental setup used to collect the data related to the measurement presented in this manuscript is provided. Special consideration is taken in the description of the longitudinally polarised muon beam and proton target, as these are the defining attributes of the analysed experiment. Brief descriptions and relevant characteristics of the COMPASS detectors used in particle tracking are also provided.

Chapter 3. The extraction of the spin dependent structure function of the proton,  $g_1^p$ , from the data is presented. This includes studies of the quality of data taking and target position determination, the selection of physical events, and the experimental technique of the asymmetry measurement. An extensive investigation of the sources of systematic uncertainties is also provided. Finally, the results for the  $g_1^p$  measurement and the comparison with previous experimental measurements are given.

Chapter 4. A Next to Leading Order (NLO) QCD fit of  $g_1$  world data including the present results is performed. The fitting procedure is described and polarised PDFs are extracted. Several sources of uncertainties in the extraction method are investigated, including sources related to the data themselves as well as to the analysis method. The results of the fit are compared to other polarised PDF extractions achieved by other authors.

An experimental evaluation of the first moment of the spin dependent structure function of the proton, deuteron and neutron based on the COMPASS data alone evolved using the global world QCD fit results is also presented. Finally, a dedicated QCD fit based solely on the combined results of this analysis with the previous COMPASS measurements (proton and deuteron) is performed to check the Bjorken sum rule. The result is compared to previous COMPASS evaluation and to a recent similar analysis.

# Chapter 1

## Nucleon spin structure

The nucleon spin structure can be accessed experimentally by several channels including polarised neutral or charged current deep inelastic scattering and polarised proton-proton collision. COMPASS uses the neutral current deep inelastic scattering with muon as scattered lepton. This channel is particularly clean, because it is dominantly an electromagnetic interaction, calculable using perturbation theory in QED. An advantage though, that vanishes when it comes to probe the gluons inside the nucleon. This chapter starts with the description of the neutral current deep inelastic scattering of charged leptons and the definition of the nucleon structure functions including spin dependent structure functions. The physical interpretation of those functions is then given in two models and spin sum rules, derived from the operator product expansion formalism, are introduced.

### 1.1 Deep inelastic scattering

In the basic deep inelastic scattering (DIS) experiment, a beam of leptons scatters off a nucleon target,  $l + N \rightarrow l' + X$ . The momenta of the incident and scattered leptons are measured, but the final hadronic state (denoted by  $X$ ) is disregarded. We then talk of an *inclusive* DIS reaction, as opposed to the *semi-inclusive* case which we will mention later. The interaction results from the exchange of a virtual photon  $\gamma^{*1}$  between the lepton and one of the constituents of the nucleon. The Feynman diagram of the reaction is shown in Fig. 1.1. Two independent kinematic variables describe the process. They are usually taken from the Lorentz invariant variables which are computed from the four-momenta of the incident lepton  $k = (E, \vec{k})$ , the scattered lepton  $k' = (E', \vec{k}')$  and the target nucleon  $P = (M, \vec{0})$  at rest for fixed target experiments. The most commonly used are:

---

<sup>1</sup> $Z^0$  exchange is neglected in the following because it is suppressed by a factor of  $\frac{Q^2}{Q^2 + M_{Z^0}^2}$ , where  $Q^2$  and  $M_{Z^0}$  are respectively the virtuality of the boson and the mass of the boson. This factor is always below 1% in the COMPASS kinematics.

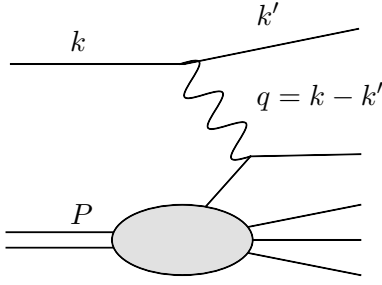


Figure 1.1: Diagram of the inclusive deep inelastic scattering of a lepton off a nucleon:  $lN \rightarrow l'X$ .

$$Q^2 = -q^2 = -(k - k')^2 \quad (1.1)$$

$$\nu = \frac{P \cdot q}{M} \stackrel{lab.}{=} E - E' \quad (1.2)$$

$$y = \frac{P \cdot q}{P \cdot k} \stackrel{lab.}{=} \frac{E - E'}{E} \quad (1.3)$$

$$x = \frac{Q^2}{2P \cdot q} \stackrel{lab.}{=} \frac{Q^2}{2M\nu} \quad (1.4)$$

$$W^2 = (P + q)^2 \stackrel{lab.}{=} M^2 + \frac{Q^2(1 - x)}{x} \quad (1.5)$$

The virtuality of the photon,  $Q^2$ , defined in Eq. (1.1) is the squared invariant mass of the virtual photon. It represents the resolution of the probe and gives the scale of the interaction. The virtual photon energy,  $\nu$ , is defined in Eq. (1.2) and the dimensionless variable  $y$  in Eq. (1.3), is the fraction of the lepton energy transferred to the virtual photon. The Bjorken scaling variable,  $x$  in Eq. (1.4), varying within  $[0;1]$  measures the elasticity of the events. It can be interpreted in the parton model (section 1.2.1) as the fraction of the nucleon momentum carried by the struck constituent. Finally,  $W^2$  is the squared invariant mass of the hadronic final state (see Eq. (1.5)). One usually exclude the low  $W^2$  region by an appropriate cut on this quantity, typically a few  $(\text{GeV}/c)^2$ , to avoid subdominant effects (so-called higher twist terms, see [1]). This can be view as excluding the region of baryon resonances. From the theoretical point of view, the DIS regime corresponds to the limit  $Q^2 \rightarrow \infty$  at fixed  $x$  values and in practice  $Q^2$  is required<sup>1</sup> to be larger than 1  $(\text{GeV}/c)^2$ . The variables used in this manuscript and describing DIS are summarised in Table 1.1.

Table 1.1: Definition of the kinematic variables used in the deep inelastic scattering.

Kinematic variable	Definition
$E$	Energy of the incident lepton
$E'$	Energy of the scattered lepton
$k$	Four-momentum of the incident lepton
$k'$	Four-momentum of the scattered lepton
$q$	Four-momentum of the virtual photon
$P$	Four-momentum of the target nucleon
$\Omega$	Solid angle into which the outgoing lepton is scattered
$Q^2$	Virtuality of the photon (scale of the interaction)
$\nu$	Lepton energy transfer to the virtual photon $\gamma^*$
$y$	Fraction of the lepton energy transferred to the virtual photon
$x$	Bjorken scaling variable (fraction of momentum of the nucleon carried by the struck quark)
$W^2$	Squared invariant mass of the hadronic system

<sup>1</sup>Reactions are considered deeply inelastic as long as the photon wavelength  $\lambda \sim 1/\sqrt{Q^2} \ll 1$  fm, to resolve the proton content.

### 1.1.1 DIS cross-section and nucleon structure functions

The differential cross-section of the inclusive DIS process can be expressed as the contraction of the leptonic tensor  $L_{\mu\nu}$  and the hadronic one  $W^{\mu\nu}$  [2]:

$$\frac{d^2\sigma}{dE'd\Omega} = \frac{\alpha^2}{Q^4} \frac{E'}{E} L_{\mu\nu} W^{\mu\nu} \quad (1.6)$$

where  $\alpha = e^2/4\pi$  is the electromagnetic coupling constant. As leptons are point-like particles, the leptonic tensor  $L_{\mu\nu}$  is completely calculable in Quantum ElectroDynamics (QED) and describes the emission of a virtual photon by the incident lepton. It comprises a symmetric part,  $\mu \leftrightarrow \nu$ , which is independent of the polarisation of the lepton, and an antisymmetric part depending on its polarisation:

$$L_{\mu\nu} = 2 \left[ k_\mu k'_\nu + k'_\mu k_\nu - g_{\mu\nu}(k \cdot k' - m^2) \right] - 4im\epsilon_{\mu\nu\rho\sigma} s^\rho k'^\sigma \quad (1.7)$$

where  $m$  refers to the lepton mass,  $g_{\mu\nu}$  is the metric tensor,  $\epsilon_{\mu\nu\rho\sigma}$  the Levi-Civita tensor and  $s^\mu$  the spin four-vector of the lepton. Here, the leptonic tensor is summed over the polarisation of the scattered lepton as its polarisation is not measured.

The absorption of the virtual photon is described by the hadronic tensor  $W^{\mu\nu}$ . However, unlike  $L_{\mu\nu}$ , it cannot be calculated in Quantum ChromoDynamics (QCD) because of non-perturbative effects in the strong interaction. Instead,  $W^{\mu\nu}$  is written in the most general form that fulfils the Lorentz invariance, parity and time reversal invariances as well as the conservation of the electromagnetic current. For a nucleon (spin 1/2 particle of spin four-vector noted  $S^\mu$ ) it is expressed as:

$$W_{\mu\nu} = \left( \frac{q_\mu q_\nu}{q^2} - g_{\mu\nu} \right) \frac{F_1(x, Q^2)}{M} + \left( P_\mu - \frac{P \cdot q}{q^2} q_\mu \right) \left( P_\nu - \frac{P \cdot q}{q^2} q_\nu \right) \frac{F_2(x, Q^2)}{M^2} \\ + i\epsilon_{\mu\nu\rho\sigma} \frac{q^\rho}{P \cdot q} \left[ S^\sigma g_1(x, Q^2) + \left( S^\sigma - \frac{S \cdot q}{P \cdot q} P^\sigma \right) g_2(x, Q^2) \right] \quad (1.8)$$

The symmetric factors in  $\mu \leftrightarrow \nu$  before  $F_1$  and  $F_2$  are spin independent while the antisymmetric part corresponds to the spin dependent terms. The non calculable part of the hadronic tensor is hidden in four unknown dimensionless functions  $F_1$ ,  $F_2$ ,  $g_1$  and  $g_2$  which describe the internal structure of the nucleon. They can only depend on Lorentz invariants and are usually expressed as a function of  $x$  and  $Q^2$ . They are called respectively spin-independent,  $F_1$ ,  $F_2$  and spin-dependent,  $g_1$ ,  $g_2$  nucleon structure functions.

In the case of unpolarised leptons or nucleons, the antisymmetric terms in the tensors cancel and only the structure functions  $F_1$  and  $F_2$  can be determined by measuring the cross-section. To access  $g_1$  and  $g_2$ , both leptons and nucleons need to be polarised.

In this thesis,  $g_1$  is the spin structure function we want to extract. To that end, DIS cross-sections of a longitudinally polarised nucleon anti-parallel  $\sigma^{\uparrow\downarrow}$  and parallel  $\sigma^{\uparrow\uparrow}$  to the lepton polarisation are used to compute a double spin asymmetry:

$$A_{\parallel} = \frac{\sigma^{\uparrow\downarrow} - \sigma^{\uparrow\uparrow}}{\sigma^{\uparrow\downarrow} + \sigma^{\uparrow\uparrow}} = \frac{(2 - y - \frac{\gamma^2 y^2}{2})g_1(x, Q^2) - \gamma^2 y g_2(x, Q^2)}{x^2 y^2 F_1(x, Q^2) + x(1 - y - \frac{\gamma^2 y^2}{4})F_2(x, Q^2)} \quad (1.9)$$

where  $\gamma = 2Mx/\sqrt{Q^2}$ .

### 1.1.2 Virtual-photon-nucleon scattering

The interpretation of the double longitudinal spin asymmetry is simpler in the virtual photon-nucleon system. Using the optical theorem, it is possible to relate the absorption of the virtual

photon to the imaginary part of the forward Compton scattering amplitudes  $\mathcal{A}_{\Lambda,\lambda,\Lambda',\lambda'}$  with  $\Lambda$  ( $\lambda$ ) and  $\Lambda'$  ( $\lambda'$ ) the helicity of the virtual photon (nucleon) in the initial state and in the final state respectively. This is illustrated in Fig. 1.2 where the DIS cross section (left) is rewritten as the multiplication of the graph by its complex conjugate (centre) which is equivalent to the imaginary part of the forward Compton scattering amplitude after summing over all the intermediate states (right). Imposing the helicity conservation as well as time and parity

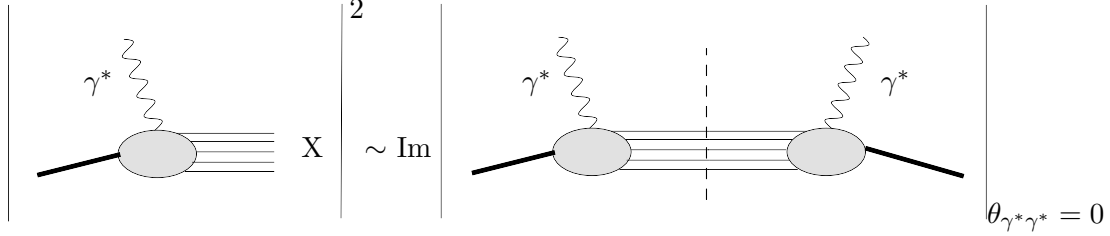


Figure 1.2: Optical theorem which connects the total virtual photon cross-section to the imaginary part of the forward Compton scattering amplitude.

symmetries, four independent amplitudes remain and are combinations of the four structure functions:

$$\sigma_{3/2}^T = \frac{4\pi^2\alpha}{K} \mathcal{A}_{1,\frac{1}{2},1,\frac{1}{2}} = \frac{4\pi^2\alpha}{MK} (F_1 + g_1 - \gamma^2 g_2) \quad (1.10)$$

$$\sigma_{1/2}^T = \frac{4\pi^2\alpha}{K} \mathcal{A}_{1,-\frac{1}{2},1,-\frac{1}{2}} = \frac{4\pi^2\alpha}{MK} (F_1 - g_1 + \gamma^2 g_2) \quad (1.11)$$

$$\sigma^{TL} = \frac{4\pi^2\alpha}{K} \mathcal{A}_{1,-\frac{1}{2},0,\frac{1}{2}} = \frac{4\pi^2\alpha}{MK} \gamma (g_1 + g_2) \quad (1.12)$$

$$\sigma^L = \frac{4\pi^2\alpha}{K} \mathcal{A}_{0,\frac{1}{2},0,\frac{1}{2}} = \frac{4\pi^2\alpha}{MK} \left[ (1 + \gamma^2) \frac{F_2}{2x} - F_1 \right] \quad (1.13)$$

where  $K$  is equal to  $\nu + q^2/2M$  according to the Hand convention [3]. The transverse virtual photon absorption cross-sections for respectively a spin projection of 3/2 and 1/2 in the initial state are noted  $\sigma_{3/2}^T$  and  $\sigma_{1/2}^T$ . Finally,  $\sigma^{TL}$  corresponds to an interference term between the transverse and the longitudinal cross-section and  $\sigma^L$  a longitudinal virtual photon absorption cross-section. One usually also introduces the total transverse virtual photon absorption cross-section:

$$\sigma^T = \frac{1}{2} (\sigma_{1/2}^T + \sigma_{3/2}^T) = \frac{4\pi^2\alpha}{MK} F_1 \quad (1.14)$$

which is completely spin independent as well as the ratio of the transverse to longitudinal virtual photon absorption cross-section:

$$R = \frac{\sigma^L}{\sigma^T} = (1 + \gamma^2) \frac{F_2}{2xF_1} - 1. \quad (1.15)$$

Two virtual photon-nucleon asymmetries are defined:

$$A_1 = \frac{\sigma_{1/2}^T - \sigma_{3/2}^T}{\sigma_{1/2}^T + \sigma_{3/2}^T} = \frac{g_1 - \gamma^2 g_2}{F_1} \quad (1.16)$$

$$A_2 = \frac{\sigma^{TL}}{\sigma^T} = \gamma \frac{g_1 + g_2}{F_1}. \quad (1.17)$$

They contain the information on the nucleon spin structure. Inserting Eqs. (1.15) to (1.17) into Eq. (1.9), the double longitudinal spin asymmetry can be rewritten as:

$$A_{||} = D(A_1 + \eta A_2) \quad (1.18)$$

where  $D$  is the depolarisation factor which makes the link between the lepton-nucleon and the virtual photon-nucleon asymmetry. It represents the transfer of polarisation from the lepton to the virtual photon and it is expressed in terms of  $y$  and  $R$ .

In COMPASS kinematics, the  $\gamma = 2Mx/\sqrt{Q^2}$  and  $\eta = 2\gamma(1-y)/(2-y)$  factors are small as well as the value of  $A_2$  [4, 5, 6] and the double longitudinal spin asymmetry  $A_{||}$  can be approximated by:

$$A_{||} \approx DA_1 = D \frac{g_1}{F_1}. \quad (1.19)$$

Using Eq. (1.15) with the same approximation,  $g_1$  can be expressed as:

$$g_1 \approx \frac{A_{||}}{D} \frac{F_2}{2x(1+R)} \quad (1.20)$$

where  $F_2$  and  $R$  are taken from previous measurements on unpolarised data.

## 1.2 Physical interpretation of structure functions

As the structure functions are not perturbative quantities, they cannot be determined from perturbative QCD. However, they can be interpreted with a model, the quark parton model, which can be improved by perturbative QCD. A more fundamental approach, also based on QCD, the operator product expansion, allows to derived model-free relationships, experimentally testable, called sum rules. In the following, examples of interpretation are given in the parton model and in the QCD improved one.

### 1.2.1 Parton model

This approach is usually formulated in a reference frame, called *infinite momentum frame*, where the nucleon moves with a large momentum in one direction. Consequently, the nucleon can be considered as composed of massless particles (*partons*) without transverse momenta (with respect to the motion of the nucleon). Considering the deep inelastic limit, the partons seen by the probe appear as free particles due to the asymptotic freedom of the strong interaction. The partons are identified to the quarks as they are the only constituents<sup>1</sup> which can interact with the probe. They carry a fraction  $\xi$  of the longitudinal nucleon momentum  $P$ . Comparing the invariant mass of the initial state ( $(\xi P + q)^2$ ) to the final one (0), the Bjorken scaling variable  $x$  is identified in this frame to the longitudinal nucleon momentum fraction carried by the struck quark:

$$0 = (\xi P + q)^2 \Rightarrow \xi = \frac{-q^2}{2P \cdot q} = x \quad (1.21)$$

In this framework, the hadronic tensor  $W_{\mu\nu}$  can be expressed as an incoherent sum of elementary tensors  $w_{\mu\nu}(\xi, s)$  weighted by the parton densities  $q_f^s(\xi)$  with electromagnetic charges  $e_f$ :

$$W_{\mu\nu} = \sum_{f,s} e_f^2 \int_0^1 q_f^s(\xi) \cdot w_{\mu\nu}(\xi, s) d\xi. \quad (1.22)$$

The sum runs over the quark flavours ( $f = u, d, s, c, b, t$ , and the charge conjugates) and the quark spin states ( $s = 1/2, -1/2$ ). The elementary tensors represent the absorption of the virtual photon by the quarks for the two spin projections. As the quarks are considered as

<sup>1</sup>Glueons do not carry electromagnetic charge.

point-like particles with two helicities, the structure of each elementary tensor can be written, by analogy to the leptonic tensor Eq. (1.7), as:

$$w_{\mu\nu}(\xi, s) = \frac{1}{2\xi P \cdot q} \delta(\xi - x) \left( 2\xi^2 P_\mu P_\nu - g_{\mu\nu} \xi P \cdot q + i\epsilon_{\mu\nu\rho\sigma} q^\rho s^\sigma \right). \quad (1.23)$$

Here, the incident lepton momentum  $k$  is replaced by the nucleon momentum fraction  $\xi P$  and the momentum of the parton in the final state (corresponding to the scattered lepton momentum) is integrated over the phase-space since it cannot be detected.

Integrating Eq. (1.22), the hadronic tensor becomes:

$$W_{\mu\nu} = \sum_f e_f^2 \left[ \frac{P_\mu P_\nu}{P \cdot q} x q_f(x) - g_{\mu\nu} q_f(x) + i\epsilon_{\mu\nu\rho\sigma} \frac{q^\rho S^\sigma}{2P \cdot q} \Delta q_f(x) \right] \quad (1.24)$$

where  $q_f(x)$  and  $\Delta q_f(x)$  are defined as:

$$q_f(x) \equiv q_f^+(x) + q_f^-(x) \quad (1.25)$$

$$\Delta q_f(x) \equiv q_f^+(x) - q_f^-(x) \quad (1.26)$$

In Eq. (1.25),  $q_f$  represents the number of quarks with flavour  $f$  which carry a fraction of nucleon momentum  $x$ . It is the sum of the quarks with a spin parallel  $q_f^+$  and anti-parallel  $q_f^-$  to the nucleon spin. The  $q_f(x)$  are called the Parton Distribution Functions (PDF). Equation (1.26) is the counterpart of  $q_f(x)$  for the difference of quarks with spin parallel and anti-parallel to the nucleon spin. As the  $\Delta q_f(x)$  depend upon the polarisation, they are called polarised PDFs.

The structure functions can be derived from Eq. (1.24) in the parton model:

$$F_1(x, Q^2) = \frac{1}{2} \sum_f e_f^2 q_f(x) \quad (1.27)$$

$$F_2(x, Q^2) = x \sum_f e_f^2 q_f(x) \quad (1.28)$$

$$g_1(x, Q^2) = \frac{1}{2} \sum_f e_f^2 \Delta q_f(x) \quad (1.29)$$

$$g_2(x, Q^2) = 0 \quad (1.30)$$

The first feature in this model is the scaling of the structure functions, *i.e.* they do not depend on the scale of the interaction. This is a direct consequence of the free point-like characteristic of the model. It was predicted by Bjorken in 1968 and observed by SLAC [7], which validated the parton model.

The second feature is the Callan-Gross relation:

$$2xF_1(x) = F_2(x). \quad (1.31)$$

In addition to the free point-like particle aspect of the quarks, it relies on the assumption of spin 1/2 particles. It was evidenced by SLAC in 1970 [8] which confirmed the spin 1/2 characteristic of the quarks.

In this picture, the sum of all quark fractions of the longitudinal nucleon momentum,  $\sum_f \int_0^1 x q_f(x) dx$ , must be one. Measurements of  $F_1$  and  $F_2$  yield instead a contribution of about 0.5. Surprisingly, half of the proton momentum fraction was missing. It turned out that the missing contribution was the one from the gluons. Gluons cannot directly couple to the virtual photon, as they are neutral particles, and they are not accounted for in the parton model. This model corresponds to the lowest order of QCD.

### 1.2.2 QCD improved parton model

In section 1.2.1, the deep inelastic limit  $Q^2 \rightarrow \infty$  ( $\alpha_s = 0$ ) was assumed and no interaction between quarks was possible. In order to take into account the gluon constituents of the nucleon, the parton model is improved in the sense of describing the DIS at finite  $Q^2 \gg M^2$ . In this limit,  $\alpha_s$  is small but non zero so that perturbative QCD can be applied.

QCD is a renormalisable gauge theory of the strong interaction based on a non-abelian group,  $SU(3)_c$ . Quarks interact via the exchange of a colour field carried by the gluons. Unlike in QED, gluons carry themselves a colour charge and can interact between each others. One of the consequences is the dependence of the strong coupling  $\alpha_s$  upon the scale of the interaction. It comprises two properties: a property of “confinement”, where single quark or gluon cannot be isolated at long distance and is always arranged in colourless hadron structures; and a property of “asymptotic freedom”, where quarks and gluons appear as free particles at short distances. At low energy scales (long distances), the strong coupling  $\alpha_s$  is of the order of unity and perturbative developments cannot be applied. Phenomena occurring in this regime are called “soft” and can only be parametrised from results of experiments. On the other hand, at large energy scales (short distances),  $\alpha_s$  is small and perturbative calculations can be carried out for such so called “hard” processes. For many measurable processes, including DIS, it has been proved that the cross-section can be factorised in terms of a calculable infrared safe quantity (hard part: quark-quark scattering cross sections, Wilson coefficients for instance) and a non-calculable universal quantity (soft part: PDF and polarised PDF for instance).

In addition to the renormalisation scale, a new scale  $\mu_f$  and a factorisation scheme are introduced to separate long and short distance parts. The factorisation scale  $\mu_f$  defines the borderline between the long and short distances, while the scheme reshuffles finite pieces between the two parts. However, cross-sections are measurable quantities that must neither depend on the factorisation scheme nor on the factorisation scale. The scheme independence of the cross-section is guaranteed as long as the hard and the soft parts are combined in the same factorisation scheme [9]. The factorisation scale independence of the cross-section is ensured by a compensating dependence on the factorisation scale of the soft and hard part [10]. In this improved parton model, the PDFs exhibit a dependence upon the scale (*i.e.* a scaling violation).

In DIS, this scale is usually identified to  $Q^2$ . The applicability of the model is commonly taken in the limit of  $Q^2 > 1$  (GeV/c)<sup>2</sup>  $\gg \Lambda_{QCD}^2 \sim 0.04$  (GeV/c)<sup>2</sup>. The  $Q^2$  dependence is interpreted as follows. By increasing the resolution of the virtual photon, the probe starts to be sensitive to the quark interactions. This is illustrated in Fig. 1.3, where the virtual photon probes a quark with a fraction of momentum  $x$  at  $Q_0^2$  (left). At higher  $Q^2$  (right), it would have seen a quark with a momentum fraction  $x - x_g$  since the virtual photon could resolve the gluon emission.

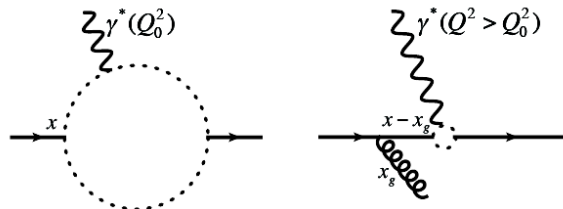


Figure 1.3: Illustration of the PDFs  $Q^2$  evolution. The dotted circles represent the resolution of the virtual photon at  $Q_0^2$  (left) and  $Q^2 > Q_0^2$  (right).

As a consequence, the number of partons carrying a small (large) fraction of the nucleon

momentum increases (decreases) with  $Q^2$ . The  $Q^2$  evolution of the PDFs follow the Dokshiter-Gribov-Lipatov-Altarelli-Parisi (DGLAP) equations. They are written in Eqs. (1.32) and (1.33) assuming  $SU(3)_f$  flavour symmetry of the light quarks and antiquarks. One flavour singlet<sup>1</sup> distribution  $q_S = u + \bar{u} + d + \bar{d} + s + \bar{s}$  which is coupled to the gluon distribution  $g$  via the splitting functions  $P_{qg}$ ; two non-singlet<sup>2</sup> distributions  $q_{NS}$ :  $q_3 = u + \bar{u} - d - \bar{d}$  and  $q_8 = u + \bar{u} + d + \bar{d} - 2(s + \bar{s})$  evolve separately from the gluons since  $P_{qg}$  are the same for the massless  $u$ ,  $d$  and  $s$  quarks and antiquarks. The number of active flavours is denoted  $n_f$ .

$$\frac{d}{d \ln Q^2} \begin{pmatrix} q_S(x, Q^2) \\ g(x, Q^2) \end{pmatrix} = \frac{\alpha_s(Q^2)}{2\pi} \begin{pmatrix} P_{qq} & 2n_f P_{qg} \\ P_{gq} & P_{gg} \end{pmatrix} \otimes \begin{pmatrix} q_S(x, Q^2) \\ g(x, Q^2) \end{pmatrix} \quad (1.32)$$

$$\frac{d}{d \ln Q^2} q_{NS}(x, Q^2) = \frac{\alpha_s(Q^2)}{2\pi} P_{qq} \otimes q_{NS}(x, Q^2) \quad (1.33)$$

The splitting functions  $P_{ij}(x/y)$  represent the probability for a parton  $j$  with a momentum fraction  $y$  to radiate a parton  $i$  with a momentum fraction  $x$  (see Fig. 1.4). The convolution

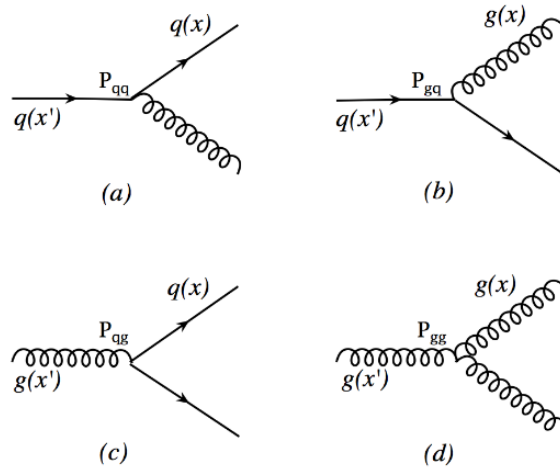


Figure 1.4: Splitting functions  $P_{ij}(z)$  of a parton  $j$  into a parton  $i$  with a momentum fraction  $z = \frac{x}{x'}$ .

product ( $h \otimes f = \int_x^1 h(\frac{x}{y}) f(y) \frac{dy}{y}$ ) sums all the contributions of gluon emission or quark creation to find a parton with a momentum fraction  $x$  in the final state.

The same  $Q^2$  evolution equations of PDFs (Eqs. (1.32) and (1.33)) are also available for the polarised case where the splitting function  $P_{ij}$  are replaced by their polarisation dependent counterparts,  $\Delta P_{ij}$ .

### 1.2.3 Parton distribution functions

According to the factorisation theorem, the long distance physics can be separated from the short distance processes. This factorisation implies the universality of the PDFs and their independence on the physical process involved. Therefore the extraction of the PDFs and the polarised PDFs is based on a global QCD analysis of all available data in a kinematic range as wide as possible. The power of such a global analysis is illustrated in this section for the unpolarised data, which cover a wide  $(x, Q^2)$  kinematic domain. The polarised case is discussed

<sup>1</sup>A symmetric combination of the quarks in  $SU(3)_f$ .

<sup>2</sup>Non-symmetric combinations of the quarks in  $SU(3)_f$ .

in chapter 4. Note that its data, provided by fixed target experiment, cover a much narrower kinematic domain.

A global QCD analysis consists in fitting simultaneously various measurements in diverse kinematic domains from different processes and provided by several experiments. The determination of the PDFs is currently based on data from charged and neutral current DIS, Drell-Yan process, inclusive jet, charm, bottom,  $W$  and  $Z$  production in  $e^\pm p$  and  $p\bar{p}$  collisions. Extra information coming from number and momentum sum rules is considered to constrain the PDFs [11].

According to the DGLAP evolution equations, the PDFs can be completely determined once they are known at a given scale. For that reason, functional forms are assumed for the different quark flavours at a reference scale  $Q_0^2$ . Commonly, simple but very flexible functional forms are postulated to limit the number of parameters to fit with a minimum introduced bias<sup>1</sup>. The reference scale is usually defined at the lowest scale limit where the DGLAP equations are valid, *i.e.*  $Q_0^2 \simeq 1 \text{ (GeV}/c)^2$ . The PDFs are evolved to the scales of the measurements and convoluted to the coefficient functions or the partonic cross-sections to obtain “predictive” observables. A  $\chi^2$  function is minimised to determine the value of the parameters of the functional forms to describe the data.

The proton structure function  $F_2^p$  which represents 30% of the input data of the global QCD analysis<sup>2</sup> is shown in Fig. 1.5 left. A very wide kinematic domain is covered in  $x$  and  $Q^2$  thanks to the combined measurements from fixed target experiments at a typical centre of mass energy of 20 GeV and from the electron-proton collider experiments at 300 GeV in the centre of mass frame. As expected from the improved parton model, the structure function appears to be weakly dependent on  $Q^2$  for intermediate values of  $x$ . On the other hand, the scaling violation of the structure function is clearly visible at both low and high values of  $x$  due to gluon radiations.

The PDFs extracted by A.D Martin, W.J. Stirling, R.S. Thorne and G. Watt (MSTW collaboration) from a global NNLO-QCD analysis, including the  $F_2^p$  measurements, are shown at 10  $(\text{GeV}/c)^2$  in Fig. 1.5 right. The high- $x$  region is dominated by valence up ( $u_v$ ) and down ( $d_v$ ) quarks but rapidly the gluon contribution becomes significant when going to intermediate- $x$  and the low- $x$  region is exclusively dominated by gluon distribution. The PDFs are rather well constrained by the unpolarised data as visible from the coloured bands corresponding to uncertainties at the 68% confidence level (C.L.). A good agreement between extractions from different collaborations is obtained. Strangeness still suffers from a larger indeterminacy though, for lack of precise and reliable data constraining it.

<sup>1</sup>Some collaborations like NNPDF, define a large number of parameters and use a neural network approach to fit the data in order to prevent the PDFs from the bias due to the choice of functional forms.

<sup>2</sup>The rest of the input data are provided by the different channels listed in the second paragraph of this section.

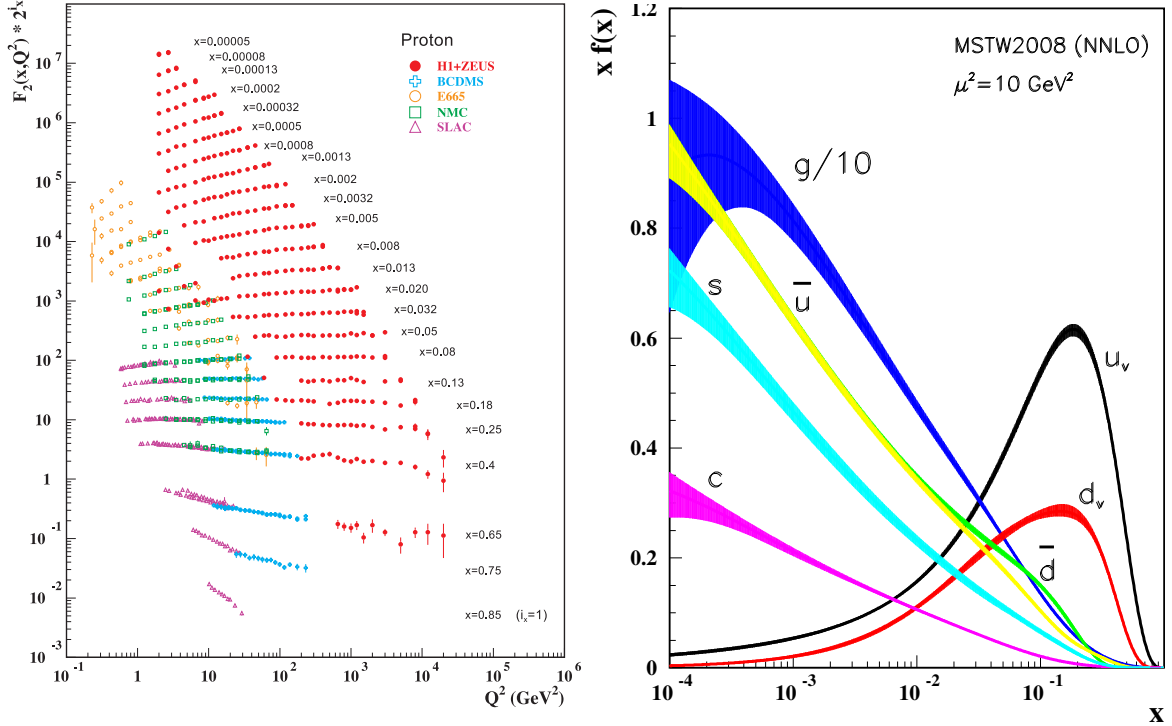


Figure 1.5: Proton structure function  $F_2^p$  as a function of  $Q^2$  for various  $x$  starting from  $5 \cdot 10^{-5}$  to 0.85 (left). Unpolarised parton distribution functions with their 68% C.L. uncertainties extracted by the MSTW collaboration [11] (right). Figures are taken from [12].

### 1.3 Operator product expansion and spin sum rules

The parton model including QCD correction in its improved version constitutes a framework in which the structure functions can be interpreted. Nevertheless, sum rules for the structure functions can be derived from a more fundamental approach based directly on QCD. They provide crucial tests of the theory as they do not depend on any model of hadronic structure.

Using the formalism of Operator Product Expansion (OPE) in the limit  $Q^2 \gg M^2$ , the first moment of the structure functions can be related to the nucleon matrix elements of local operators and Wilson coefficients, which can be derived from perturbative QCD. A description of the OPE formalism can be found in [2]. Only the outline of the approach at leading twist<sup>1</sup> applied to the first moment of the  $g_1$  functions are recalled since they are related to the spin puzzle of the nucleon.

The operators  $A_{q\mu} = \bar{\psi}\gamma_\mu\gamma_5\psi$  are the axial-vector currents. Applied on a quark  $q$ , the matrix elements of the operators correspond to the components of the quark spin vector  $s_\mu$ :

$$\langle q, s | \bar{\psi}\gamma_\mu\gamma_5\psi | q, s \rangle = 2s_\mu \quad (1.34)$$

At leading order, it can be shown that the matrix element of the operator applied on a nucleon with a momentum  $P$ , and a longitudinal spin  $S$  can only be proportional to  $S_\mu$  via non perturbative elements  $a_q$ :

$$\langle P, S | \bar{\psi}\gamma_\mu\gamma_5\psi | P, S \rangle \stackrel{LO}{=} 2a_q S_\mu \quad (1.35)$$

<sup>1</sup>The twist of an operator is defined as the mass dimension of the operator minus its spin. Higher twist ( $t > 1$ ) operators expand in powers of  $(M/Q)^{t-2}$ .

Using the OPE, the first moment of  $g_1$  can be written as:

$$\Gamma_1 = \int_0^1 g_1(x) dx \stackrel{LO}{=} \frac{1}{2} \sum_q e_q^2 a_q \quad (1.36)$$

for the light quark flavours  $u$ ,  $d$  and  $s$ . It is usual to introduce the  $SU(3)_f$  flavour symmetry and to gather the  $a_q$  elements in three combinations corresponding to the three diagonal Gell-Mann matrices,  $\lambda_0$ ,  $\lambda_3$  and  $\lambda_8$ :

$$\begin{cases} a_0 &= a_u + a_d + a_s \\ a_3 &= a_u - a_d \\ a_8 &= a_u + a_d - 2a_s \end{cases} \quad (1.37)$$

$a_0$  corresponds to the axial-vector singlet of  $SU(3)_f$ , while  $a_3$  and  $a_8$  are two non-singlet combinations of  $SU(3)_f$ . In this case,  $\Gamma_1$  reads:

$$\Gamma_1 = \frac{1}{9}a_0 + \frac{1}{12}a_3 + \frac{1}{36}a_8 \quad (1.38)$$

Within the parton model (*i.e.* collinear quarks and gluon non interacting between themselves), the matrix elements  $a_q$  are expressed as the first moment of the quark and antiquark polarised distribution functions<sup>1</sup>:

$$a_q \equiv \Delta(q + \bar{q}) \equiv \int_0^1 \Delta q(x) + \Delta \bar{q}(x) dx \quad (1.39)$$

where  $\Delta(q + \bar{q})$  counts for the difference between the quarks and antiquarks of flavour  $q$  aligned and anti-aligned to the nucleon spin. It implies that  $a_0 = \Delta(u + \bar{u}) + \Delta(d + \bar{d}) + \Delta(s + \bar{s})$  represents the total contribution of the quark spins to the nucleon spin  $\Delta\Sigma$ .

Going beyond the leading order, the first moment  $\Gamma_1$  is  $Q^2$  dependent and the Wilson coefficients,  $C_1^S$  and  $C_1^{NS}$ , are introduced to take higher order of QCD into account:

$$\Gamma_1(Q^2) = \frac{1}{9}C_1^S(Q^2) a_0(Q^2) + C_1^{NS}(Q^2) \left[ \frac{1}{12}a_3 + \frac{1}{36}a_8 \right]. \quad (1.40)$$

The matrix element  $a_3$  and  $a_8$  are still  $Q^2$  invariant in the extend of  $SU(3)_f$  due to current conservation[13, 14]. However, the singlet current is not conserved as a consequence of the axial anomaly [15, 16] and the matrix element  $a_0$  is  $Q^2$  dependent. Depending on the scheme of factorisation,  $a_0$  can be related in  $\overline{MS}$  (Modified Minimal Subtraction) scheme directly to a  $\Delta\Sigma_{\overline{MS}}(Q^2)$ , that depends on the scale<sup>2</sup> or to an ‘‘intrinsic quark spin contribution’’ (independent of the scale) together with an explicit gluon spin component (scale dependent)  $a_0 = \Delta\Sigma - \frac{3\alpha_s}{2\pi} \Delta G(Q^2)$  in the AB (Adler-Bardeen) scheme.

### 1.3.1 Ellis-Jaffe sum rule $SU(3)$

One of the remarkable fact of the  $SU(3)_f$  flavour symmetry is that the octet of current, involved in the weak  $\beta$ -decay of the neutron and the spin 1/2 hyperons, is related to the axial-vector current used to obtain the matrix elements  $a_3$  and  $a_8$ . Moreover, in  $SU(3)_f$ , those  $\beta$ -decay can be described by two parameters  $F$  and  $D$  so that:

$$a_3 = \Delta u - \Delta d = F + D \quad (1.41)$$

$$a_8 = \Delta u + \Delta d - 2\Delta s = 3F - D \quad (1.42)$$

<sup>1</sup>The notation is slightly confusing since in literature  $\Delta q$  can also refer either to  $\Delta q(x)$  or to  $\int_0^1 \Delta q(x) + \Delta \bar{q}(x) dx$ .

<sup>2</sup> $\overline{MS}$  is the scheme used in chapter 4.

Using the values of the matrix elements of the axial-vector currents in Eq. (1.40), one obtains the *Ellis-Jaffe* sum rule:

$$\Gamma_1^p = C_1^S(Q^2) \left[ \frac{3F - D + 3\Delta s}{9} \right] + C_1^{NS}(Q^2) \left[ \frac{3F + D}{18} \right]. \quad (1.43)$$

Within the parton model and with the additional assumption that the strange quarks do not contribute to the spin of the nucleon,  $a_0$  can identify with  $a_8$ , Eq. (1.44). In this case, the *Ellis-Jaffe* sum rule predicts a value for the first moment of the proton  $\Gamma_1^p$ , see Eq. (1.45) [17].

$$\Delta s \simeq 0 \Rightarrow a_0 \simeq a_8 \quad (1.44)$$

$$\Gamma_1^p = \frac{5}{36}a_8 + \frac{1}{12}a_3 = 0.188 \pm 0.004 \quad (1.45)$$

From Eq. (1.44), one can also derive a value for the quark spin contribution:

$$\Delta\Sigma_{E-J} \sim 0.6 \quad (1.46)$$

First extraction of  $\Delta\Sigma$  obtained from  $\Gamma_1^p$  was given by EMC (*European muon collaboration*) [18], which reported a *Ellis-Jaffe* sum rule violation in the approximation of Eq. (1.44) and a compatible value of  $\Delta\Sigma$  with zero:

$$\Gamma_1^p = 0.123 \pm 0.013 \pm 0.019 \quad \text{at} \quad \langle Q^2 \rangle = 10 \text{ (GeV}/c)^2 \quad (1.47)$$

$$\Delta\Sigma = 0.12 \pm 0.09 \pm 0.14 \quad (1.48)$$

These results are at the origin of the "spin crisis" or more appropriately "spin surprise" according to [19]. The EMC measurements imply that if the  $SU(3)_f$  symmetry stays valid the strange quark polarisation contribution,  $\Delta s$ , is sizeable and negative, else  $\Delta s=0$  but  $\Delta\bar{u} \simeq \Delta\bar{d} < 0$ . In both cases, sea quark contribution is significant. The other explanation comes from a confusion in the results. EMC actually did not measure  $\Delta\Sigma$  but the observable  $a_0$ . In that case, the relation between  $a_0$  and the "true" quark polarisation  $\Delta\Sigma$  is given by:

$$a_0(Q^2) = \Delta\Sigma - 3\frac{\alpha_s}{2\pi}\Delta G(Q^2) \quad (1.49)$$

where  $a_0$  receives a direct contribution from the gluon polarisation due to the axial anomaly. Finally, the evaluation of  $\Gamma_1^p$  from the unmeasured region at  $x < 10^{-2}$  was questionable. For the latter, an evaluation of  $\Gamma_1^p$  with a reduced unmeasured range  $x < 0.0036$  is presented in section 4.1.3.

However, the "spin surprise" came from the fact that the parton model was expected to be correct, since successful descriptions of the static properties of the hadrons were obtained (like charge and anomalous magnetic moments for instance [19, 20]) but the EMC measurements do not constitute a contradiction of QCD.

### 1.3.2 Bjorken sum rule $SU(2)$

A way to test QCD is to evaluate the *Bjorken* sum rule [21, 22]. This sum rule assumes only  $SU(2)_f$  flavour symmetry. This symmetry also known as the isospin symmetry is more fundamental in QCD than  $SU(3)_f$ .

The matrix element of the proton can be related to the one of the neutron according to:

$$a_0^p = a_0^n \quad (1.50)$$

$$a_3^p = -a_3^n \quad (1.51)$$

$$a_8^p = a_8^n \quad (1.52)$$

Moreover,  $a_3$  can be taken from the neutron weak  $\beta$ -decay constant  $g_A/g_V$ , which is measured with a high accuracy:  $g_A/g_V = 1.2701$  [12]. The *Bjorken* sum rule reads at leading twist:

$$\Gamma_1^p(Q^2) - \Gamma_1^n(Q^2) = \frac{1}{6} \cdot \frac{g_A}{g_V} C_1^{NS}(Q^2) \quad (1.53)$$

where  $C^{NS}(Q^2)$  is the non-singlet Wilson coefficient. It has been calculated up to the third order in  $\alpha_s$ . A verification of this sum rule via the extraction of  $g_A/g_V$  from the first moment of the proton and deuteron spin structure functions is presented in section 4.2.

## 1.4 COMPASS new $g_1^p$ proton spin structure function data at 200 GeV

In 2011, COMPASS took data using the 200 GeV polarised muon beam from CERN SPS and a polarised proton target ( $\text{NH}_3$ ) to complement the existing set of polarised DIS data. Other data in a similar kinematic range had been taken by SMC at 190 GeV with a lower luminosity, and at COMPASS at 160 GeV on proton ( $\text{NH}_3$ ) and deuteron ( ${}^6\text{LiD}$ ) polarised targets. The 200 GeV energy had been chosen to provide new constraints in a wider kinematic domain, as well as to improve the statistical accuracy of the existing measurements.

The new 200 GeV data set, which is the object of the work presented in this thesis, allows to perform a verification of the Bjorken sum rule with better balance statistics between previous COMPASS proton and deuteron data.

Those data are also included in a global NLO QCD fit of  $g_1$  proton, deuteron and neutron world data to extract the polarised PDFs.



## Chapter 2

# The COMPASS experiment

COMPASS is a fixed target experiment located at CERN on the SPS. The experiment is dedicated to the study of nucleon spin structure and hadron spectroscopy as meant by its name "COmmon Muon and Proton Apparatus for Structure and Spectroscopy". Structure has been addressed with a polarised muon beam and polarised targets, while spectroscopy has relied on hadron beams. The proposal [23, 24] was accepted in 1998. One of the main goals of the spin structure programme was to measure directly the gluon polarisation [25, 26]. In parallel, using the same data a large improvement in the statistical accuracy of DIS, both inclusive and semi-inclusive, polarised measurements was at hand [27, 28, 29].

A second phase began in 2012 [30] and is devoted among others to the study of generalised parton distributions through deeply virtual Compton scattering, nucleon transverse momentum dependent distributions through the polarised Drell-Yan process and chiral perturbation theory through Primakoff reactions.

In this chapter, the experimental setup used for polarised DIS measurements is presented. It comprises the description of the polarised muon beam, the polarised target and some elements of the COMPASS spectrometer.

### 2.1 Polarised beam

The beam is supplied to COMPASS hall through the M2 extraction line of the Super Proton Synchrotron (SPS). The SPS provides a high intensity proton beam ( $\sim 10^{13}$  protons in typically 5 s spill for a SPS cycle of 17 s) with a momentum of about 400 GeV/c. This primary beam (Fig. 2.1) impinges on a 500 mm thick Beryllium target (T6) and produces mainly pions and secondarily kaons. A set of quadrupoles and dipoles guides the positive pions with a nominal momentum of  $217 \pm 10\%$  GeV/c along a 500 m long decay tunnel. In this channel, a large fraction of pions decays into a muon and a neutrino. At the end of the tunnel, a large Beryllium hadron absorber takes in the remaining pions, while the muons go through it with an energy loss of about 1%. The muon beam is steered to the experimental setup through a series of dipoles and magnetic collimators that selects the energy band and through quadrupoles that keep it focused.

The muon momentum is measured by four hodoscopes and two scintillating fibre stations surrounding three dipoles and four quadrupoles which constitute the beam momentum station (BMS - Fig. 2.2). For the nominal intensity of  $1.6 \cdot 10^8 \mu^+$ /spill at 200 GeV/c, the BMS measures each incident muon with an accuracy of 0.5%. The main characteristics of the detectors composing the BMS are given in Table 2.1.

In the pion rest frame, the muons are naturally polarised by parity violation of the weak decay. As the neutrinos are only left-handed and the pions are spinless particles, the produced

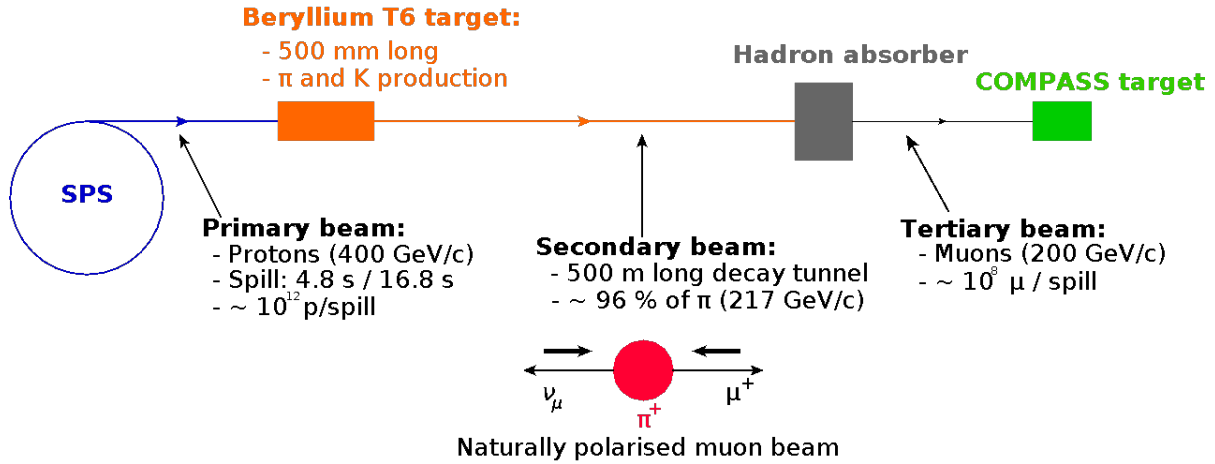


Figure 2.1: Sketch of the M2 beam line with the polarised muon beam production.

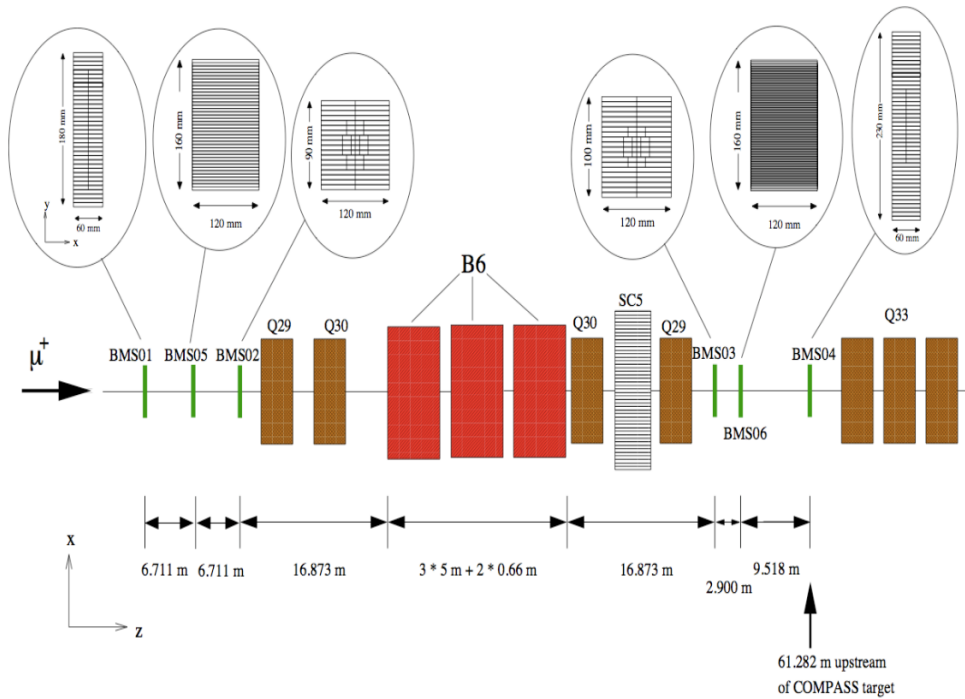


Figure 2.2: Layout of the beam momentum station (Fig. taken from [31]). The hodoscopes are denoted BM01 to BM04, the scintillating fibre stations BM05 and BM06, the dipoles B6 and the quadrupoles Q29 to Q32.

Table 2.1: Main features of the hodoscopes making up the BMS [32].

Detector	Active area $X \times Y$ (cm <sup>2</sup> )	Resolution
BM01-04	6-12 $\times$ 9-23	$\sigma_s = 1.3\text{-}2.5$ mm, $\sigma_t = 0.3$ ns
BM05	12 $\times$ 16	$\sigma_s = 0.7$ mm, $\sigma_t = 0.5$ ns
BM06	12 $\times$ 16	$\sigma_s = 0.4$ mm, $\sigma_t = 0.5$ ns

muons have negative helicities. Since the helicity is not a Lorentz invariant, after applying the Lorentz boost, the muon helicity depends on the decay angle defined in the centre of mass frame with respect to the pion direction in the laboratory frame. Forward produced muons keep a negative helicity while backward muons obtain a positive helicity (Fig. 2.3). Similar conclusions can be drawn for kaons which constitute a small component of the secondary beam. For highly relativistic particles, the angle dependence can be expressed by the ratio of the muon momentum,  $p_\mu$ , to the parent momentum,  $p_{hadron}$ , in the laboratory frame. The dependence of the muon polarisation on the ratio of momenta  $p_\mu/p_{hadron}$  is shown in Fig. 2.4a for both pion and kaon decay. A high value of this ratio ensures a high value of muon polarisation and no degradation from kaon contamination. The value 0.92 is chosen for  $p_\mu/p_{hadron}$  to maximise the figure of merit  $I \cdot P^2$  (see Fig. 2.4a for the polarisation  $P$  and Fig. 2.4b for the intensity  $I$ ).

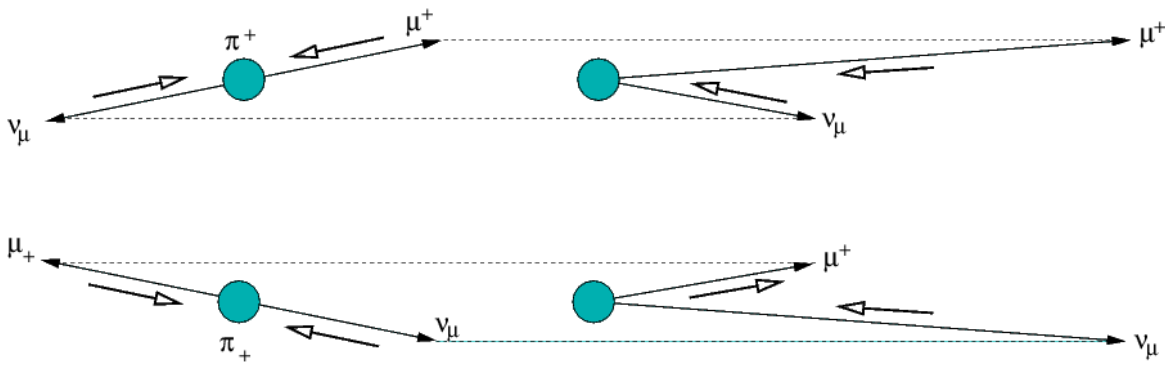


Figure 2.3: Pion decay into a muon-neutrino pair in c.m. (left) and laboratory (right) frame. Upper (lower) figure is for forward (backward) muon production.

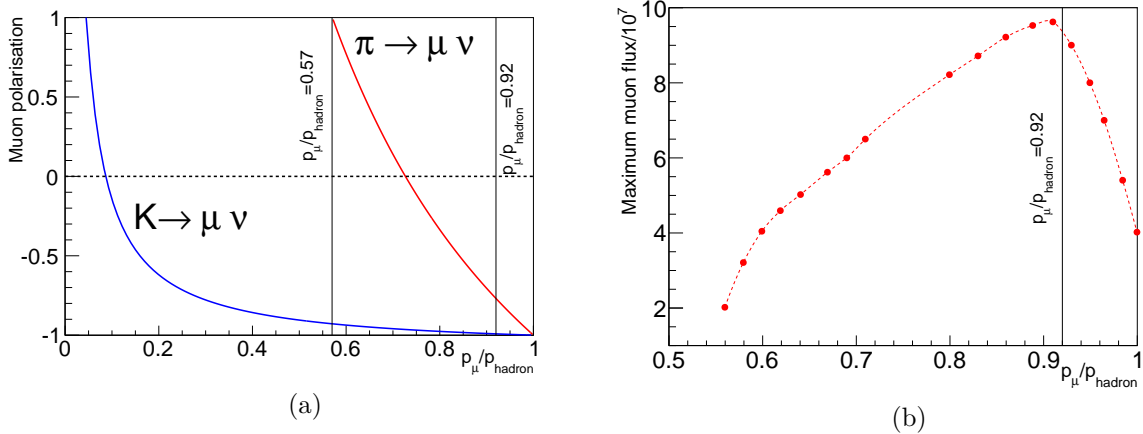


Figure 2.4: a-Average muon polarisation as a function of  $p_\mu/p_{hadron}$ . b-Maximum muon flux for  $10^{12}$  protons on the T6 target versus  $p_\mu/p_{hadron}$ . Figures a and b are taken from [32, 33]. The lines  $p_\mu/p_{hadron} = 0.57$  and  $p_\mu/p_{hadron} = 1.0$  represent the two extreme cases (backward and forward) muon production from pion decay. The figure of merit  $I \cdot P^2$  is maximised for  $p_\mu/p_{hadron} = 0.92$ .

The beam polarisation could be in principle analytically computed, however as the hadron beam is not monochromatic the muon beam polarisation has to be corrected for momentum spread and acceptance effects as well as for energy losses, especially in the hadron absorber. For these reasons, a parametrisation of the muon beam polarisation as a function of the muon

momentum is built using a Monte-Carlo simulation named Halo [34]. This program comprises a detailed description of the beam optics including field maps inside and outside the magnet apertures and including the material of potential scatterers, such as collimators and tunnel walls. It is run separately for pion and kaon beams.

The individual muon polarisation is determined at the decay position, while the muon energy is evolved along the beam line. Muons lost during the transport are discarded, those leaving the nominal aperture, going through material and regaining the nominal aperture before the target are kept and tagged as “halo” muons. The beam polarisation is the weighted average of the polarisation of “direct” muons and “halo” muons coming from both pion and kaon decays and going through the COMPASS target. Figure 2.5a shows the beam polarisation for the different contributions as a function of the beam momentum. As expected from the weak dependence on  $p_\mu/p_{hadron}$  around 0.92 in Fig. 2.4a, the polarisation of the “direct” and “halo” muons from kaons is very flat and close to  $-1$ . For pions, as the slope of the muon polarisation is much steeper as a function of  $p_\mu/p_{hadron}$  (Fig. 2.4a), the beam polarisation shows a stronger dependence on the beam momentum. For the “halo” muons from pion decays, a plateau is visible at low momenta and can be explained by energy losses during the trajectory of the particle out of the nominal aperture. This causes a reduction of the particle momentum, while the polarisation has been determined before the energy losses. The final beam polarisation

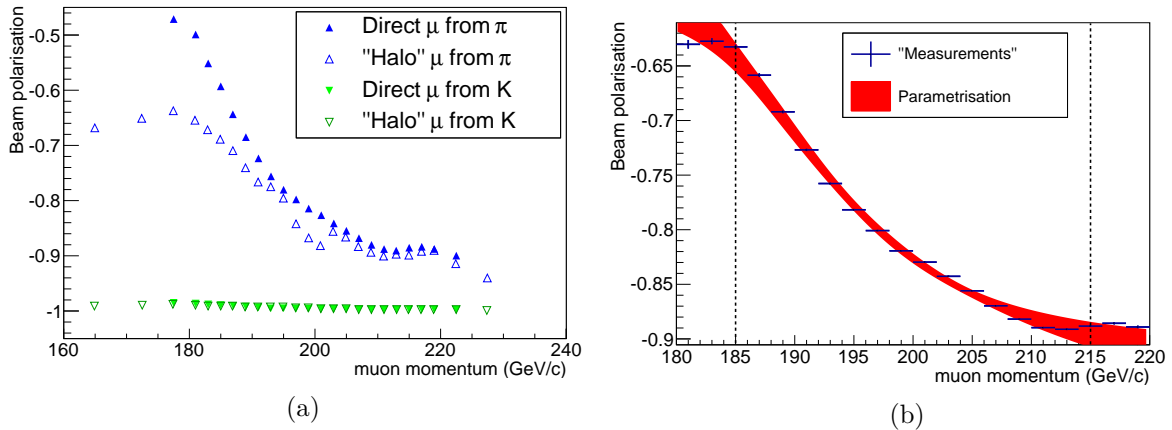


Figure 2.5: a-Muon beam polarisation versus momentum for the four components of the beam (parent hadron). The halo refers to hadrons which left the nominal aperture at some point but went through the COMPASS target. b-Final beam polarisation summing over all contributions. The vertical error bars correspond to the statistical uncertainty on the beam polarisation within a slice of beam momentum (horizontal error bar) and the red band shows the results of a fit to an arc tangent function at 95% C.L.

is calculated as a weighted average of all the contributions. The points are fitted using an arc tangent function to extrapolate the beam polarisation to any momentum (Fig. 2.5b). The statistical accuracy of the Monte-Carlo simulation is well below 1‰ and the systematics of the order of 4%. They include repeatability of the beam settings and alignment drift. The reliability of the Monte-Carlo simulation was demonstrated by the Spin Muon Collaboration (SMC) which measured also the beam polarisation on the same beam line by two different techniques: muon elastic scattering asymmetry off an electron target and muon decay in flight  $\mu^+ \rightarrow e^+ \nu_e \bar{\nu}_\mu$ . Both results were in agreement with the Monte-Carlo simulation [35, 36, 33].

## 2.2 Polarised target

The material for the solid state polarised target is either deuterated lithium ( $^6\text{LiD}$ ) or ammonia ( $\text{NH}_3$ ) crystals for measurements on the deuteron or proton respectively. The polarisation

of the material relies on the Zeeman effect which allows a splitting of the spin state in the presence of an intense and homogeneous magnetic field. Such a magnetic field is provided by a superconducting solenoid supplying a 2.5 T field along the beam direction with a homogeneity  $\delta B/B < 4 \cdot 10^{-5}$ . The polarisation achieved at thermal equilibrium is given by the Curie law which reads for a spin 1/2 particle:

$$P_{1/2} = \tanh\left(\frac{\mu B}{kT}\right) \quad (2.1)$$

where  $\mu$  is the magnetic moment of the nucleus,  $B$  is the value of the magnetic field,  $T$  is the temperature and  $k$  is the Boltzmann constant. Due to the tiny value of the proton magnetic moment, only a small polarisation of about 0.5% can be reached even at a few Kelvins while in the same conditions a polarisation above 99% is obtained for electrons.

In order to increase the target polarisation, the dynamic nuclear polarisation (DNP) technique is used. It consists of transferring dynamically the polarisation of the electrons to the nucleus. The material is first irradiated by an electron beam at low temperature to create paramagnetic centres in the crystal lattice (around  $10^{-4} - 10^{-3}$  per nucleus) which can be filled with single polarisable electrons. In the presence of the strong magnetic field of the solenoid, the electron spin couples to the nucleus hyperfine structures accessible by Zeeman effect. Therefore a polarisation state can be induced by microwave radiations (Fig. 2.6a).

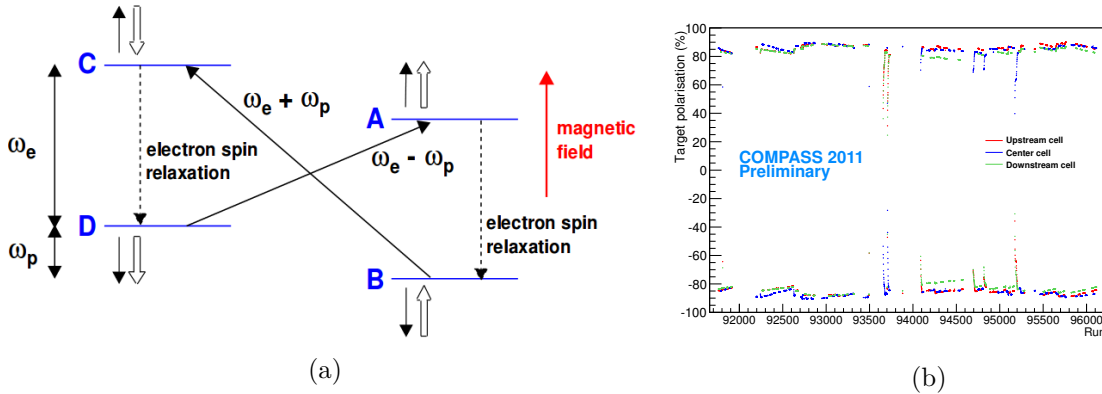


Figure 2.6: a-The four energy levels defined by the spin projections of an electron-nucleus system. Transitions between the levels are possible using microwave frequencies at  $\omega_e + \omega_p$  and  $\omega_e - \omega_p$ . Single (double) arrows stand for the spin projection of the electron (nucleus). b-Target polarisations for the upstream (red), downstream (green) and central (blue) cells versus the run number.

At equilibrium, only the B and D states are populated by roughly the same amount. Applying a microwave radiation with a frequency  $\omega_e + \omega_p$  ( $\omega_e - \omega_p$ ), a transition from the B(D) state to the C(A) state is induced. It consists of a simultaneous flip of the spin state of the electron and of the nucleus to anti-align,  $B \rightarrow C$ , (align,  $D \rightarrow A$ ) the nucleus spin with the magnetic field direction. Promptly ( $\sim 1$  ms) the electron spin relaxation occurs which leaves the target in a D(B) state. As the electron gets back to its initial state, it can be used to polarise several nuclei in its vicinity. Nuclei far from the paramagnetic centres are polarised by spin diffusion [37, 38]. As the time of relaxation of the nucleus is very long ( $\sim 1$  min), the target remains in that polarisation state. By operating in a so-called frozen spin mode, *i.e.* at very low temperature of about  $\sim 50$  mK, the time of relaxation can be of several months. Such a low temperature is reached thanks to a  $^3\text{He}$ - $^4\text{He}$  refrigerator system.

A peculiarity of the COMPASS target is its composition in three cells of 4 cm diameter and 30 cm, 60 cm and 30 cm long, *i.e.* 1.2 m long in total: the longest polarised target in the world. The most upstream and downstream cells are shone with one of the two microwave

frequencies (for instance  $\omega_e + \omega_p$ ) whereas the central cell is radiated with the other frequency ( $\omega_e - \omega_p$ ) so that the central cell is always polarised in opposite direction with respect to the upstream and downstream cells. This unique configuration better ensures that the two target spin states are supplied with the same beam flux.

The target polarisation is measured by Nuclear Magnetic Resonance [39] (NMR) by means of 10 coils along the target cells. The NMR signals are calibrated from measurements of thermal equilibrium signals at 1 K [40, 41]. Almost constant target polarisations of about 0.8 and -0.8 with an accuracy of 3.5% are reached during the data taking (see Fig. 2.6b). Every day, the spin states of the cells are reversed adiabatically without any polarisation loss by means of a dipole magnet. The magnet produces a transverse field of about 0.5 T with respect to the beam direction, which combined with the inversion of the current in the solenoid rotates continuously the magnetic field within the target as well as the spin states within the cells. The dipole can also be used to polarise the target transversely with respect to the beam axis. A sketch of the target is shown in Fig. 2.7.

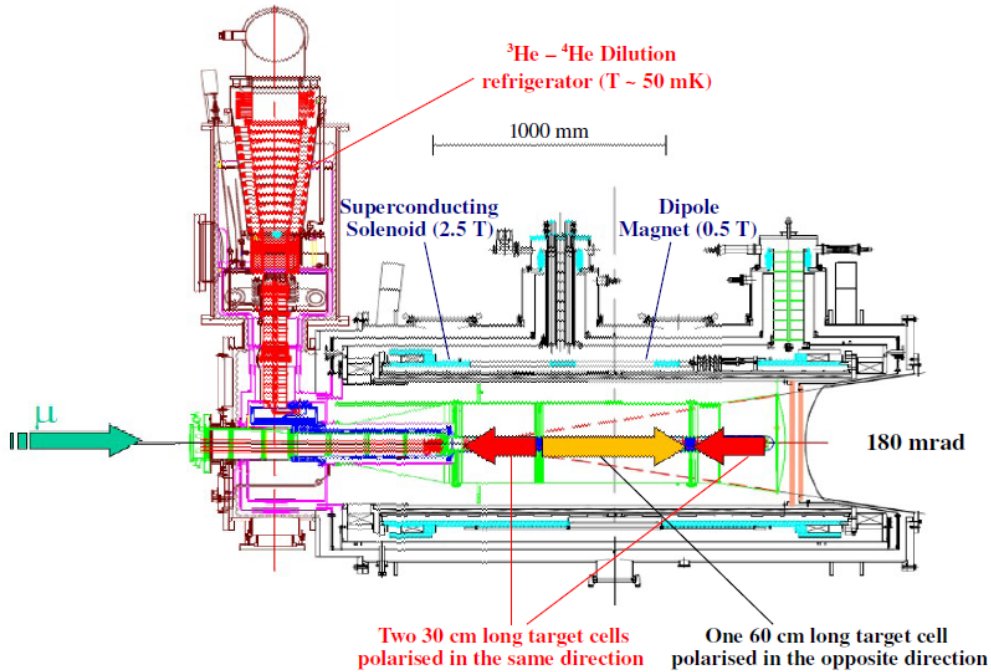


Figure 2.7: Sketch of refrigerated polarised target. The arrows indicate the orientation of the polarisation for each target cell. The geometrical acceptance of the target is limited to  $\pm 180$  mrad defined by the radius of the solenoid.

## 2.3 Spectrometer

The spectrometer is composed of two stages each including a dipole magnet (Fig. 2.8). The first stage, named LAS for Large Angle Spectrometer, is dedicated to low energy particles or particles emitted at large angle. The main element is the dipole magnet SM1 with a wide aperture of  $\pm 180$  mrad which matches the angular acceptance of the target. The main component of the field is vertical from top to bottom with a field integral of 1 Tm [42]. SM1 is located 4 m downstream of the target and ensures the measurement of particle momenta up to a few dozen GeV/c.

The second stage, Small Angle Spectrometer (SAS), covers particle momenta from 5 GeV/c

to a few hundred  $\text{GeV}/c$  and can detect all particles emitted in a cone of 30 mrad in opening angle. The dipole SM2 present in this stage is located 18 m downstream of the target and has a field integral of 4.4 Tm. As for SM1, the main field component of SM2 is vertical.

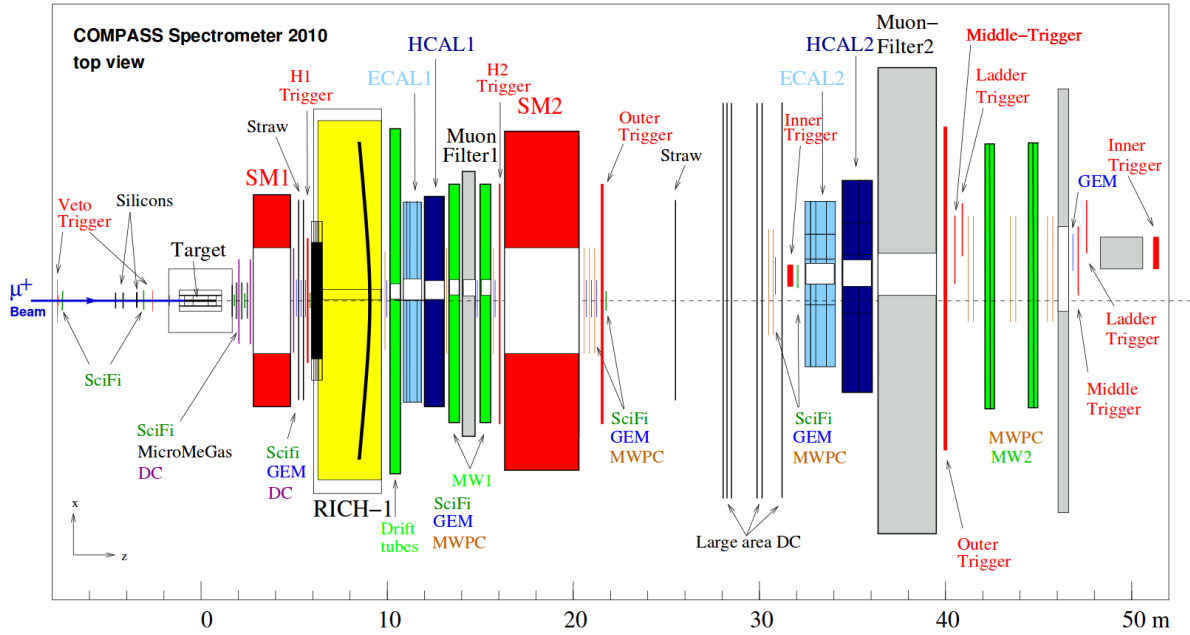


Figure 2.8: Sketch of the top view of the COMPASS muon setup (as built in 2010, no change compared to 2011).

Whether it be in the LAS or in the SAS, each dipole is preceded and followed by telescopes of trackers and ends with electromagnetic and hadronic calorimeters as well as a muon filter. The momentum resolutions achieved for those two stages are shown in Fig. 2.9. Due to the difference in bending power of the two dipoles, the relative momentum resolution  $\sigma_p/p$  is about 0.5% in the SAS and 1.2% for the tracks reconstructed in the LAS alone. It is also possible to retrieve some particles escaping the SM1 magnet using its fringe field but the momentum resolution in this case is of about 10%. A description of the main detectors of the spectrometer is given in the next section.

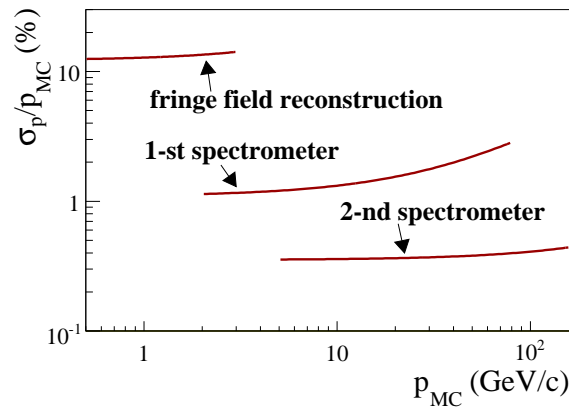


Figure 2.9: Relative track momentum resolution  $\sigma_p/p$  versus  $p$ .

### 2.3.1 Tracking detectors

The trajectories of charged particles are determined on both sides of the dipoles so that their deviation through the magnetic field allows for a measurement of the ratio of their charge  $q$  to their momentum  $p$ . The achieved resolution depends on the resolution of the angle of deviation  $\theta$  which depends on the multiscattering along the particle path and on the detector resolutions. As the particle flux decreases rapidly along the radial distance from the beam, different technologies are used to build the detectors depending on their angular acceptance. Three angular regions are identified and covered by the very small area trackers, the small area trackers and the large area trackers to which corresponds a maximal particle flux of  $5 \cdot 10^7$  Hz/cm<sup>2</sup>,  $3 \cdot 10^5$  Hz/cm<sup>2</sup> and  $1 \cdot 10^4$  Hz/cm<sup>2</sup>, respectively. A summary of the different detectors with some relevant characteristics for each region is given in Table 2.2 and below.

Table 2.2: Segmentation of the COMPASS spectrometer acceptance into three angular regions [32].

Very small area trackers (maximal flux: $5 \cdot 10^7$ Hz/cm <sup>2</sup> )			
Detector	# of det.	Spatial resolution ( $\mu\text{m}$ )	time resolution (ns)
Scintillating fibres	23	120-210	0.35-0.45
Silicon microstrip	6	8-11	2.5
Small area trackers (maximal flux: $3 \cdot 10^5$ Hz/cm <sup>2</sup> )			
Detector	# of det.	Spatial resolution ( $\mu\text{m}$ )	time resolution (ns)
Micromegas	12	90	9
GEM	22	70	12
Large area trackers (maximal flux: $1 \cdot 10^4$ Hz/cm <sup>2</sup> )			
Detector	# of det.	Spatial resolution ( $\mu\text{m}$ )	time resolution (ns)
Drift Chamber	3	190	-
Straw	9	190	-
MWPC	14	1600	-

#### Very Small Area Trackers

- Scintillating fibres:  
They consist of 14 planes of detection with an active area from  $4 \times 4$  cm<sup>2</sup> to  $12 \times 12$  cm<sup>2</sup> and are placed along the beam axis in the LAS as well as in the SAS. Each plane measures one coordinate (vertical, horizontal or inclined by  $45^\circ$ ) and is organised in 7 layers of strands bringing 7 fibres together.
- Silicon microstrips:  
They are organised in 3 stations of 2 detectors with an active area of  $5 \times 7$  cm<sup>2</sup>. Each detector can measure two components at the same time thanks to perpendicular readout strips between the n-side and the p-side. All the stations are located before the target and measure 4 projections (vertical, horizontal and inclined by  $\pm 5^\circ$  with respect to the horizontal axis).

The excellent spatial and time resolutions make those detectors suitable for beam particle tracking. They can be used to propagate the incoming muon track back to the BMS and the association of the extrapolated track in coincidence with the measurement of the BMS solve possible ambiguities between several beam track candidates.

### Small Area Trackers

- Micromegas:

They are Micro Pattern Gaseous Detectors (MPGD) and are based on a MICRO MESH Gaseous Structure ensuring a low material budget [43]. They consist of a conversion gap placed on top of an amplification gap separated by a micro-mesh Fig. 2.10. Primary electrons are created by ionisation in the conversion gap. They drift to the mesh and enter the amplification gap where due to the strong electric field an avalanche occurs. The ions produced during the avalanche are collected by the mesh in order to keep a fast time response while the electrons are gathered by readout strips. They have an active area of  $40 \times 40 \text{ cm}^2$  with a blind centre of 5 cm diameter. They are located between the solenoid and the SM1 magnet in 3 stations of 4 detectors (one for each projection: horizontal, vertical and inclined by  $\pm 45^\circ$ ).

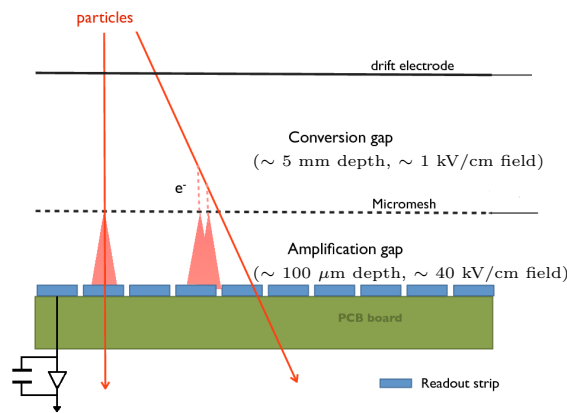


Figure 2.10: Principle of a Micromegas detector.

- GEM:

They are MPGD consisting of three Gas Electron Multiplier (GEM) foils which split the gas chamber into 3 amplification stages as shown in Fig. 2.11 [44]. Each foil is  $50 \mu\text{m}$  thick and drilled with holes of  $70 \mu\text{m}$  diameter. Each side of the foil is submitted to a different potential to create a strong electric field in the holes. Primary electrons are created in the drift gap and multiplied in each GEM foil when passing a hole which ensures the amplification and the collection of ions. The sharing of the amplification over several stages guarantees low possibilities of electrical discharges. They have an active area of  $31 \times 31 \text{ cm}^2$  with a deactivated centre of 5 cm diameter. They are distributed along the beam axis after the SM1 magnet in 11 stations of two detectors (one measuring 2 projections).

### Large Area Trackers

- Drift chambers:

They are large gaseous volumes comprised between two cathodes made of Mylar coated with graphite between which is placed alternately a potential wire of  $100 \mu\text{m}$  diameter and a readout wire of  $20 \mu\text{m}$  diameter as shown in Fig. 2.12. A cascade of electrons is created when an ionising particle crosses a drift cell and is collected by the readout wires. Three detectors, DC00, DC01 and DC04, composed of eight layers of wires with 4

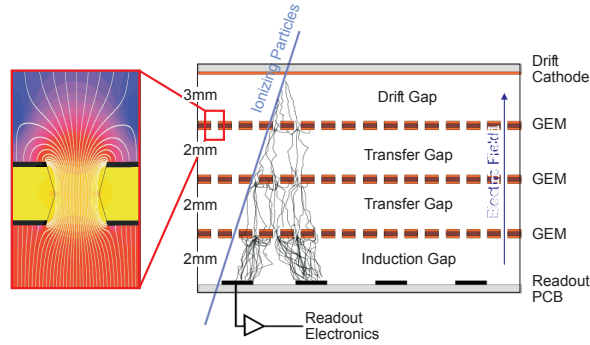


Figure 2.11: Schematic side view of a triple GEM detector. The inset shows the electric field configuration in the vicinity of a hole.

inclinations (vertical, horizontal and tilted by  $\pm 15^\circ$  and  $\pm 20^\circ$  for DC04 with respect to the vertical axis) are used. They have an active area of  $180 \times 127 \text{ cm}^2$  and  $240 \times 204 \text{ cm}^2$  for DC04 with a deactivated centre of 30 cm diameter. They are located before and after the SM1 magnet.

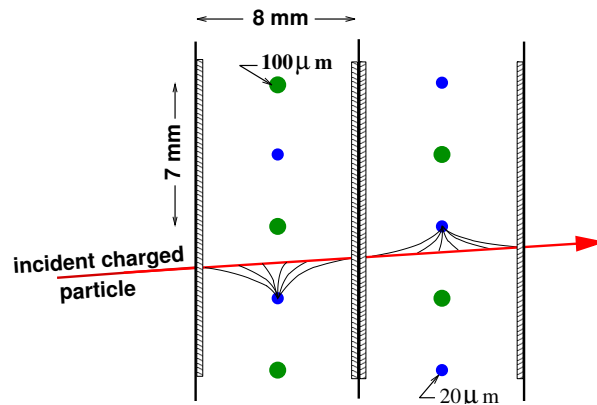


Figure 2.12: Drift cell geometry of the drift chambers as delimited by the two cathode foils and the two potential wires.

- Straw tube chambers:

These gaseous detectors are similar in working principle to the drift chambers. They consist of an assembly of Kapton tubes of 6 mm diameter. Each tube is plated with aluminium and used as a cathode. A thin anode wire of  $30 \mu\text{m}$  diameter made of gold-plated tungsten is placed in the centre of every tube and brought to a high potential. A cascade of electrons is created when an ionising particle crosses a tube and is collected by the central wire. The straw tube detector [45] consists of two layers of tubes and measures one component. Three stations of three detectors with an active area of  $323 \times 280 \text{ cm}^2$  are placed between the two dipoles.

- Multiwire proportional chambers:

The tracking at large radial distance in the SAS is mainly ensured by multiwire proportional chambers. They have an active area of  $178 \times 120 \text{ cm}^2$  and a blind centre of 16 cm to 22 cm diameter depending on their position in the spectrometer. Three stations of two detectors are placed along the beam axis.

### 2.3.2 Particle identification

Several devices are installed in the LAS and the SAS to ensure particle identification:

Two “muon filters” are used to identify the scattered muons. They consist of an absorber, made of a 60 cm thick iron plate in the LAS and a 2.4 m thick concrete wall in the SAS, sandwiched between two low resolution tracking detectors. The tracking is ensured by drift tube detectors having a spatial resolution of 3 mm in the LAS and from 0.6 mm to 0.9 mm in the SAS.

Two sets of electromagnetic and hadronic calorimeters realise the energy measurement of particles. They complete each stage of the spectrometer and are designed to match the acceptance of the LAS. As their use in terms of calorimetry is marginal in this analysis (except for quality checks in 3.1.2), they are not described. The main features of each of the calorimeters can be found in [32, 46].

Finally, a Ring Imaging CHerenkov detector is used to perform the hadron (pion, kaon, proton) identification with as low as possible material budget. This detector is particularly interesting when studying identified hadron spin asymmetries, which are not detailed in this thesis. The characteristics of the detector can be found in [46].

## 2.4 Data recording

### 2.4.1 Trigger system

The goal of the trigger system is to select event candidates in a very short time ( $< 500$  ns) and with a small dead time in a high rate environment. The triggers launch the data acquisition and provide the reference time of the event. Several components such as a veto system, fast hodoscope signals and energy deposits in calorimeters participate in the trigger system depending on the kinematic of the reactions [32, 47].

The veto system is composed by three scintillating counters located 20 m, 8 m and 3 m before the target with central holes of 10 cm, 4 cm and 4 cm in diameter, respectively. Those counters are in anti-coincidence with all others components of the trigger system to prevent events to be triggered by divergent beam particles (halo muon).

For deep inelastic scattering reactions, the trigger system is based mainly on hodoscope signals which rely on the information on scattered muons alone. The trigger is fired when the signal of two hodoscopes, which are made of slabs of fast scintillators are in coincidence and that the trajectory of the hit slabs points to the target<sup>1</sup>. The hodoscopes in coincidence are: H4L and H5L for the Ladder Trigger (LT), which covers low values of  $Q^2$  in the DIS regime; H4M and H5M for the Middle Trigger (MT), which extends the kinematic coverage up to few  $(\text{GeV}/c)^2$  in values of  $Q^2$ ; and completed by H3O and H4O for the Outer Trigger (OT), which significantly contributes to measuring values of  $Q^2$  up to  $30 (\text{GeV}/c)^2$ . Those three sub-triggers constitute the purely inclusive trigger component of the trigger system.

A second component of the trigger system is provided by hodoscope signals combined with a calorimetric condition. This is the case for the Inner Trigger (IT), which requires the coincidence of H4I with H5I and an energy deposit beyond the one expected of a single muon in one of the two hadronic calorimeters to reduce background triggers due to elastic or quasi-elastic scattering. This sub-trigger covers almost the same kinematic domain as the LT in the DIS regime and will contribute slightly to the final sample of this analysis. However, the LAS Trigger (LAST), which requires also an energy deposit in the calorimeters in addition to the

<sup>1</sup>The trigger system was actually designed to the requirement of both proper DIS and quasi-real photo-production at low  $Q^2$ . In the later case, as the muon scattering angle is small, instead of target pointing, the trigger is based on the energy loss of the scattered muon by measuring its deflection in the two spectrometer magnets. This is the case of the IT and LT which do not contribute much in this analysis.

coincidence between H1G and H2G hodoscopes contributes significantly in measuring events with  $Q^2$  above  $30 \text{ (GeV/c)}^2$  and up  $100 \text{ (GeV/c)}^2$ . Those sub-triggers form the semi-inclusive trigger component of the trigger system.

Finally, a standalone calorimeter signal can trigger the data acquisition when the scattered muon escapes the hodoscope-based trigger acceptance. This is particularly interesting at very large  $Q^2$  (in the absence of the LAST). In this case, the energy deposit must be well beyond the one expected by a single muon.

The schematic position of the hodoscopes as well as the kinematic domains covered are shown in Figs. 2.13 and 2.14 for a 160 GeV muon beam and the experimental setup up to 2007. In 2010 and for the 2011 data taking with a muon beam of 200 GeV, the additional hodoscope system (LAST) was added to better cover the large values of  $Q^2$ , H1G was installed before SM1 and H2G after SM2. The projection of the fraction of the different trigger component contributions as function of  $x$  and  $Q^2$  for a 200 GeV muon beam is given in Fig. 2.15.

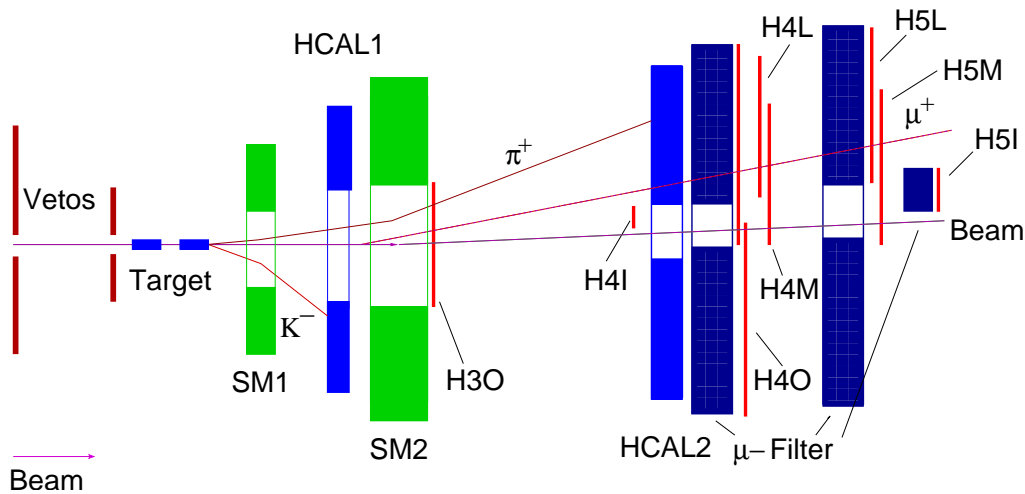


Figure 2.13: Schematic view of the trigger system. The most upstream veto and the H1G and H2G hodoscopes are not shown.

Table 2.3: Trigger component

		Target pointing	Energy loss of the scattered $\mu$	Low E deposit in calorimeters	High E deposit in calorimeters
inclusive	IncMT	✓	✓		
	OT	✓			
	LT		✓		
semi-inclusive	IT		✓	✓	
	MT	✓	✓	✓	
	LAST	✓		✓	
calorimetric	CT				✓

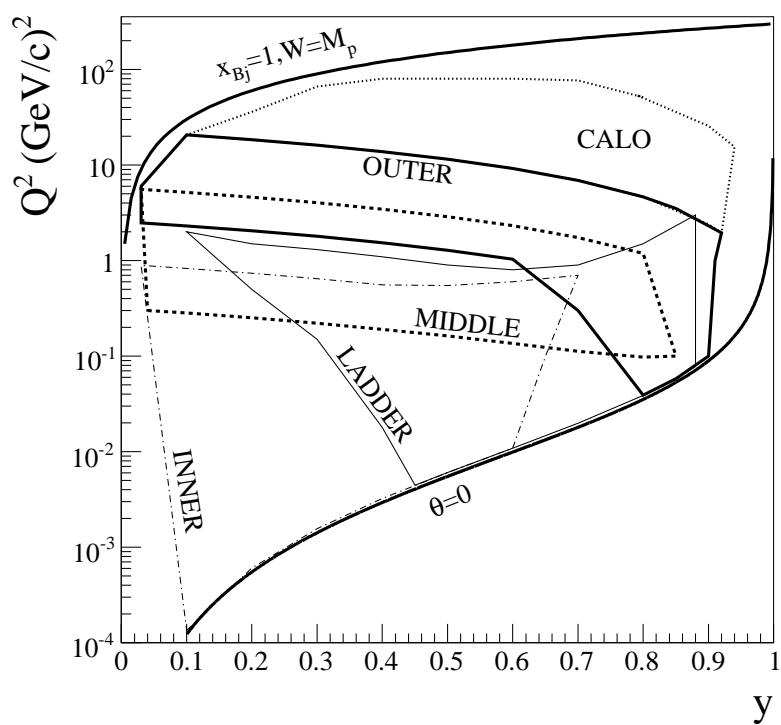
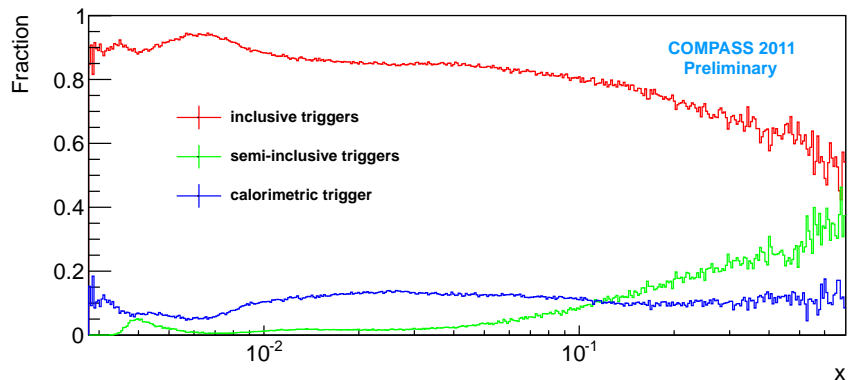
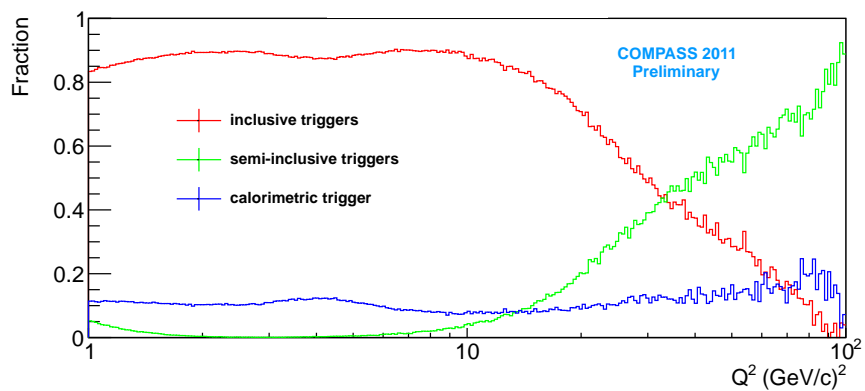


Figure 2.14:  $y$ - $Q^2$  coverage of the trigger subsystems for a 160 GeV muon beam. The two lines, ( $x_{Bj} = 1$ ,  $W = M_p$ ) and ( $\theta = 0$ ) show the kinematic limits of elastic scattering and forward scattering, respectively. The newly added LAS trigger spans the same domain as the calorimeter triggers in the DIS region.



(a)



(b)

Figure 2.15: Fraction of events triggered by three subsystems: a hodoscope signal alone (inclusive in red), by a hodoscope signal combined with a calorimeter signal (semi-inclusive in green) and by a calorimeter signal alone (calorimetric in blue) as a function of the Bjorken scaling variable (a) and  $Q^2$  (b) for a 200 GeV muon beam.

### 2.4.2 Data acquisition system

For each triggered event, the information of the detectors are recorded by the Data Acquisition (DAQ) system. Preamplified and discriminated signals of the detectors are digitised via analog or time to digital converters and sent to readout driver modules (CATCH or GeSiCA). Those modules ensure the transfer of data from the front-end cards of the detectors to readout-buffer PCs when a signal is emitted from the trigger control system. The aim of the readout-buffer is to store temporarily the data and merge them in partial events. Those pieces of events are then collected by event builders which create and save global events on raw data files containing the times and the amplitudes of the signals of the detectors' channels. Data files of about 1 GB size are automatically copied on the tapes of the CERN central computer centre. The architecture of the DAQ system is sketched in Fig. 2.16.

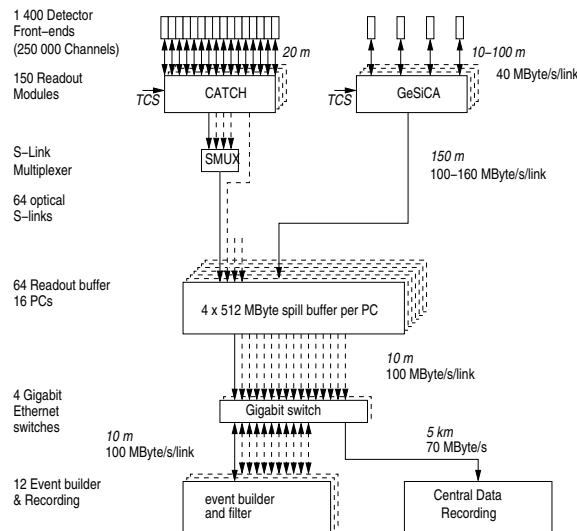


Figure 2.16: General structure of the DAQ system. It mainly consists on three stages: digital signals collection, the readout modules, partial events storage, the readout buffer PCs, and event records, the event builder (see text).

### 2.4.3 Event reconstruction

The transition from raw data information to physical analysable quantities is realised by the COmpass Reconstruction Algorithm Library (CORAL) software. It consists mainly in reconstructing the trajectories of the muon beam, the scattered muon and the final hadrons, as well as the position of the vertices. From a description of the position of the detectors (alignment file), magnetic field maps and calibration files, the raw data are converted into spatial hits in the detectors and energy deposit in the calorimeters. Specific algorithms merge adjacent hits into clusters which are fitted into trajectories. The converging trajectories are matched into vertices. The reconstructed information is stored in the form of Data Summary Tape (DST) which can be further analysed in a specific physics channel. The illustration of a reconstructed DIS event from CORAL is shown in Fig. 2.17.

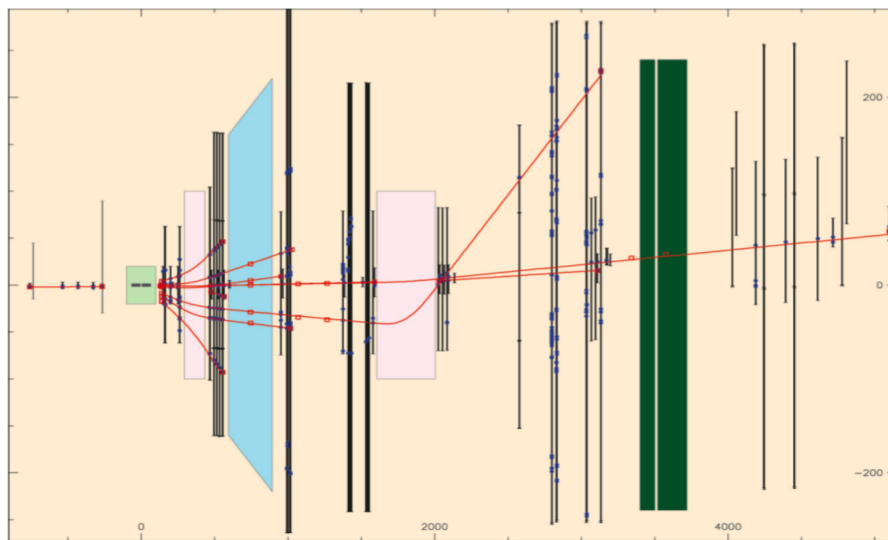


Figure 2.17: Typical reconstructed DIS event in the spectrometer. The target is in light green, the two dipoles are in pink, the detector planes in black with the associated clusters of hits in blue and the reconstructed charged particle trajectories in red.

## Chapter 3

# Extraction of spin asymmetries and spin-dependent structure function of the proton

In this chapter, the full chain of the analysis implemented to calculate the asymmetry is presented. As a first step, the stability of the apparatus is studied and the position of the target is determined. This stage is essential to prevent possible bias, especially when a small asymmetry (down to a few percents) is measured. Then the selection of data, the method of extracting the asymmetries and a review of the systematic effects are introduced. The chapter ends with the result of the proton spin dependent structure function  $g_1^p$ .

### 3.1 Stability of the apparatus

The operation of all detectors of the spectrometer was monitored during the whole data taking to ensure stability in data recording. However, failures and repairs of detectors happen sometimes and it is not easy to determine whether the issue encountered may impact the data because of the complexity and redundancy of the apparatus. For this reason, before extracting any physical quantity, the stability of relevant variables versus time is studied. First checks are performed on a spill by spill basis ( $\sim 10$  s) where the stability of variables directly correlated to the efficiency or reliability of the detectors is monitored. Then an analysis on a run by run ( $\sim 100$  spills) basis is carried out to monitor the stability of well known physical quantities. The latter case points to possible misalignments of the detectors or calibration issues.

#### 3.1.1 Identification of bad spills

In the spill by spill analysis the time scale is the spill. The stability of reconstructed variables over the spill number is analysed to evaluate the quality of the data taking. This analysis is performed by a modified version of the software developed by the COMPASS collaboration to make a study for each trigger independently<sup>1</sup>. The following variables are studied separately for each of the six triggers:

- Number of primary vertices per event
- Number of beam particles per primary vertex
- $\chi_r^2$  of the primary vertices per vertex
- Number of tracks per primary vertex

<sup>1</sup>Depending on the physics channel: trigger mix, use of calorimeter or RICH, a set of unstable spill lists is provided

- $\chi_r^2$  of the tracks per track
- Number of hits per track
- Trigger rate
- Number of charged clusters per event
- Charged cluster energy per event
- Likelihoods per track

Assuming that most of the recorded data are good, a fair estimator of the statistical fluctuations of the variables is the root-mean-square (RMS) of each distribution. The method used to identify the bad spills is the following: the value of each variable for a given spill is compared to the ones of its neighbours comprised in a gliding window of 1,200 spills. A spill is marked as bad, if for any of the distributions its number of neighbours within a certain amount of RMS is lower than a threshold. In case of a stable data taking, none of the spills differs significantly from its neighbours and a peak is expected around 1,200 neighbours; in case of a clear instability a peak is also present around zero.

An example for the case of the number of tracks per vertex distribution is shown in Fig. 3.1 left. The bad spills, marked in red, are derived after the cut on the neighbour distribution, Fig. 3.1 right. Pseudo-efficiencies of the 416 planes of detection are also studied. They are easily and

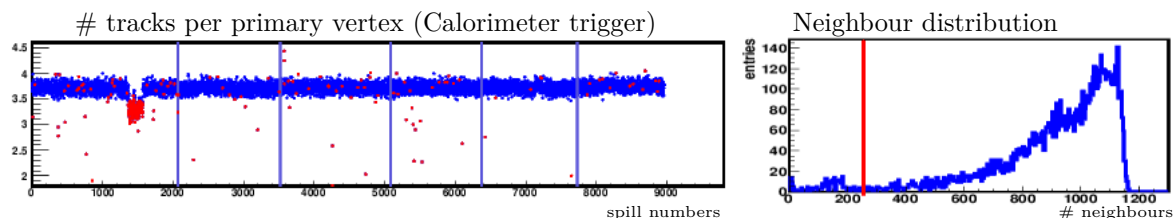


Figure 3.1: Left: Example of bad spill identification for the number of tracks per primary vertex versus the spill number for a period of data taking. The blue lines represent a rotation of the solenoid field. The identified bad spills are in red. Right: Neighbour distribution of the distribution on the left with an entry for each spill. The vertical red line represents the cut on the minimal number of neighbours.

rapidly available for the full data taking and are computed from the ratio of the number of hits detected in a plane to the number of hits expected during the reconstruction. As all the planes are used to reconstruct the data, including the plane which is being considered, those pseudo-efficiencies are always higher than the real efficiencies. However, they can still provide useful information on the stability of detection and problems in the reconstruction. No more spill rejection has been made at this stage because only temporary and limited losses of pseudo-efficiency of detectors were observed and were judged to be compensated by the redundancy of the tracking; otherwise the spill would have been rejected in the analysis described above. Nevertheless, the pseudo-efficiencies are considered for a grouping of data in stable short lapses of time (see section 3.1.3).

Table 3.1 shows the percentage of rejected spills after this stability study. A relatively large fraction of the recorded data are rejected in the period<sup>1</sup> W25 because of instabilities in one of the triggers which were impacting all the other triggers. W32 shows also a large rate of rejection because it underwent several trips of quadrupoles of the extraction beam line.

### 3.1.2 Run by run stability

Once the basic stability checks of the spectrometer are realised on a spill by spill basis, the stability of the apparatus in measuring physical quantities is carried out. This more sophisticated approach is more sensitive to alignment and magnetic field issues as well as to calorimeter

<sup>1</sup>A period corresponds to about a week of data taking with a dedicated offline alignment of the detectors. 12 periods have been taken in 2011.

Table 3.1: Percentage of rejected spills for each period of data taking.

Period	Percentage of rejected spills	Period	Percentage of rejected spills
W25	28.66%	W34	10.31%
W27	8.64%	W36	4.37%
W30	6.17%	W38	3.15%
W31	9.46%	W39	2.73%
W32	26.85%	W41	2.35%
W33	4.70%	W43	4.33%

calibrations. Three quantities were investigated: the value of the Bjorken scaling variable  $x$  for  $\mu - e$  elastic scattering events, the mass of the  $K^0$  and the missing energy in the reconstruction of exclusive  $\rho$ . As an illustration of the stability checks only the former two are presented below.

### Elastic $x_{\mu e}$ scattering stability

The Bjorken scaling variable  $x$  is usually defined for a proton target therefore in case of an elastic scattering with an electron ( $\mu e \rightarrow \mu' e$ ) its value is equal to the ratio of the mass of the electron,  $m_e$ , to that of the proton,  $m_p$ . The selection of  $\mu - e$  elastic scattering events is defined at  $Q^2 < 1 \text{ (GeV/c)}^2$  by a primary vertex with two outgoing tracks (the scattered muon and a negative charged particle). To identify the electron, the ratio of the energy deposited by the negative charged particle in the electromagnetic calorimeters to its momentum is required to be within 0.8 and 1.2. The exclusivity of the reaction is ensured by a constraint on the coplanarity of the scattering Eq. (3.1) and on the transverse momentum conservation Eq. (3.2).

$$\frac{\vec{p}_\mu \times \vec{p}_{\mu'}}{|\vec{p}_\mu \times \vec{p}_{\mu'}|} \cdot \frac{\vec{p}_\mu \times \vec{p}_e}{|\vec{p}_\mu \times \vec{p}_e|} < -0.9 \quad (3.1)$$

$$P_{\mu\perp} - P_{e\perp} < 0.02 \text{ GeV}/c. \quad (3.2)$$

Finally the angles of the two outgoing tracks with respect to the incoming muon have to be correlated and smaller than 6 mrad.

The  $x_{\mu e}$  distribution for each run is fitted by a Gaussian and the results are compared to  $\frac{m_e}{m_p}$  versus the run number (Fig. 3.2).

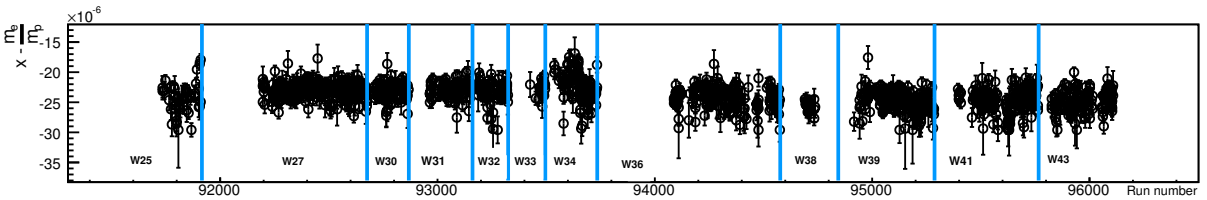


Figure 3.2: Stability of  $x$  for  $\mu - e$  elastic scattering events versus the run number for the whole year. The blue lines corresponds to different offline alignments of the detectors.

The mean value is shifted by 4.6% compared to the PDG value of  $m_e/m_p$  [12]. However the distribution is very stable and hence does not lead to further rejection.

### $K^0$ mass stability

$K^0$  are reconstructed using events with secondary vertices with two opposite-charged tracks. The invariant  $K^0$  mass is calculated assuming both particles are pions. The mass peak is fitted by two Gaussians and a linear function to describe the background. The result from the fit is compared to the PDG value and the difference is shown in Fig. 3.3 versus the run number. The distribution is very stable and the relative difference with the PDG value is of 0.2%.

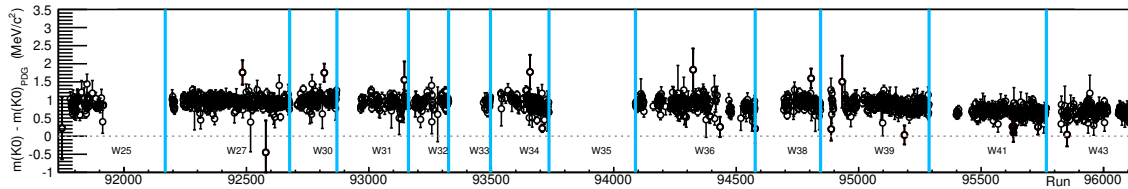


Figure 3.3: Stability of  $K^0$  mass versus the run number for the whole year. The blue lines illustrate the change in the offline alignment of the detectors.

### 3.1.3 Data grouping

The data are gathered into small groups of runs close in time and involving two opposite directions of the solenoid field. The idea is to prevent any false asymmetry from biasing the physics asymmetry. The groups are determined according to the stability of the spill by spill analysis and the detector pseudo-efficiencies. For acceptance considerations between the two spin states, groups are determined also by taking into account balanced statistics between two orientations of the solenoid field. This results in rejections of 4.5% of the runs because of badly balance statistics between the two solenoid fields. An additional 5.5% of the runs are rejected due to target polarisation losses during the data taking.

## 3.2 Target position

To determine precisely the position of the target, the full statistics accumulated during the data taking is needed. The idea is to identify some elements of the target such as the microwave stoppers between the target cells (for the z-position) and the mixing chamber (for x-y-position). All events having a vertex with an incoming muon and several outgoing particles are retained. In a first step, to determine the z-position, a cut on the radial position is imposed to remove most of the target material ( $r < 2$  cm) and the mixing chamber ( $r > 3.6$  cm). Moreover only events with a good resolution on the z-coordinate ( $\delta z < 0.75$  cm) are kept. The distribution of the z-position of vertices is plotted and an excess of events appears at the positions of the two microwave stoppers. Both peaks are fitted by a Gaussian to obtain the central position of the microwave stoppers. The fitted position of the two stoppers, together with the technical drawing of the target give the precise position of the target cells.

In a second step, the interactions with the mixing chamber in which the target is placed are studied. The cut on the resolution of the z-position of the vertices is released to  $\delta z < 2$  cm. The radial cut is set to remove only events in the target material ( $r < 1.5$  cm). The distribution of the position of vertices in the transverse plane lets the contour of the mixing chamber appear. A circle with a radius  $r_{mixing} = 36.45$  mm is fitted to the outer contour of the mixing chamber and gives the central position of the target. To determine the tilt of the target, the same procedure is repeated on 12 slices of target along the z-direction. A very small angle of  $1.04 \pm 0.07$  mrad is observed. Figure 3.4 shows the fits to the microwave stoppers on the left and an

example of the circle fitting the mixing chamber. The position of the target is summarised in Table 3.2.

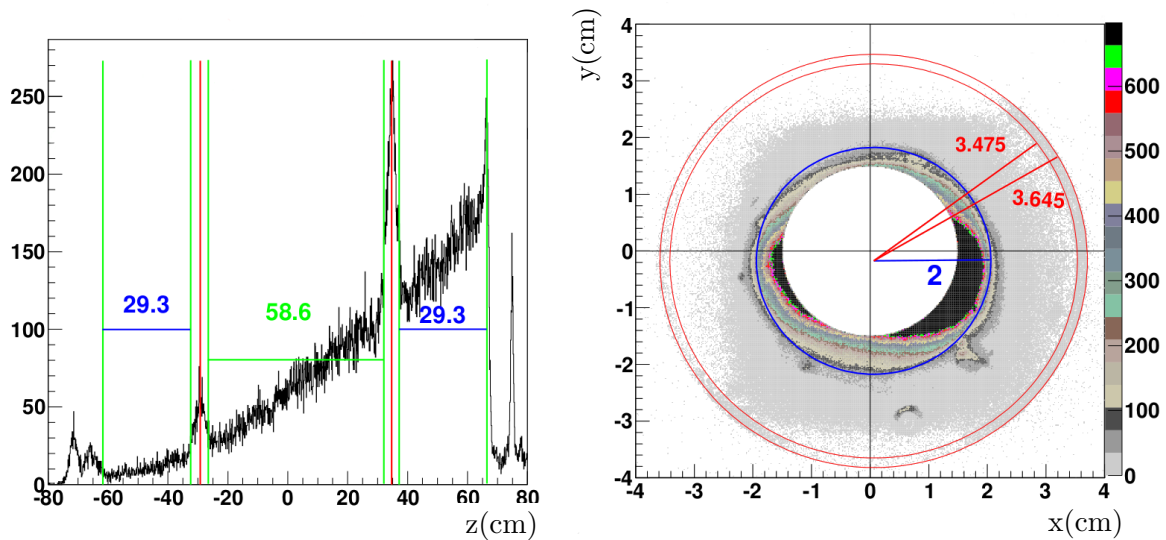


Figure 3.4: Position of the target along the beam axis on the left. The red lines show the centre of the microwave stoppers. The green line shows the edge of each target cell. The transverse plane of the target is shown on the right. The two red circles illustrate the contour of the mixing chamber, the blue circle shows the target cell position.

Table 3.2: Summary of the target position along the beam axis and in the transverse plan.

$z \in [-61.7, -32.4] \cup [-26.5, 32.1] \cup [37.2, 66.5]$		
Target centre given by:		
	upstream	downstream
x-centre	-0.0073 cm	0.1261 cm
y-centre	-0.1680 cm	-0.1796 cm
Target Radius: $r \leq 1.9$ cm		

### 3.3 Target filling

Knowing the position of the target, a study of its filling is performed. Since the number of interactions with the ammonia material is much higher than the interaction with the cooling helium, a lack of interactions within a part of the target indicates a deficit of ammonia in that region. The distribution of the transverse position of vertices within the target is studied for several slices of target. However, this distribution is a convolution of the target filling and the beam profile so a deconvolution of these two distributions has to be done before checking the uniform distribution of ammonia within the target. For that reason, the distribution of interacting vertices is normalised by the distribution of beam tracks. The latter quantity is determined by the position of the beam tracks recorded by a random trigger. No region of the target reveals any sign of bad filling, as shown in Fig. 3.5.

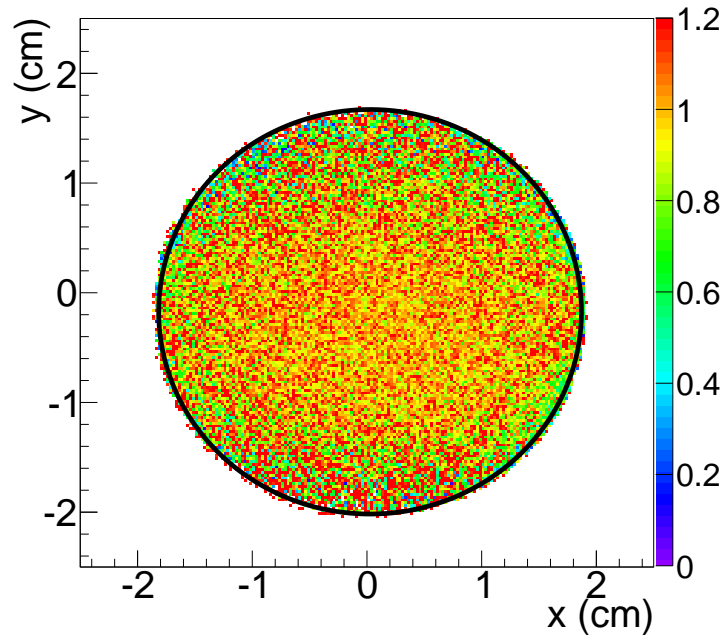


Figure 3.5: Check of the target filling in the transverse plane for the most downstream cell: ratio of the distribution of vertices to the number of beam tracks. The black curve shows the position of the target.

### 3.4 Data selection

The full statistics accumulated in 2011 after the removal of bad spills and taking into account the grouping list is used. About  $12 \cdot 10^9$  events were recorded but only a small fraction of them remains in the final physics sample. Any physical trigger is considered in this analysis, whether it be purely inclusive or have a calorimetric condition. The primordial selection of events demands the presence of an incoming muon reconstructed before the target and associated to a vertex containing at least one outgoing particle. The identification of one of the outgoing particles as a scattered muon requires that the outgoing particle has the same charge as the beam and goes farther than the first muon filter. The number of radiation lengths crossed by that particle has to be larger than 30 and its extrapolated trajectory must fall into the active area of the fired trigger. In case the event contains more than one outgoing track fulfilling these requirements, the event is discarded.

To guarantee the quality of the primary vertex, a fiducial cut on the reduced  $\chi^2$  is applied ( $\chi_r^2 < 10$ ) and, in addition, the sum of all fractional energies  $z_h$  of the outgoing particles has to be smaller than one. The position of the primary vertex has to be within one of the three cells of the target in order to determine the spin state of the material with which the incoming muon has interacted. Finally, the extrapolation of the incoming muon track must cross the entire target so as to keep constant the beam flux over the three cells.

The kinematic domain available for the analysis is selected by cuts on the virtuality of the photon,  $Q^2$ , and on the fractional energy transferred from the muon beam to the virtual photon,  $y$ . The former cut guarantees the hard scale of the process with  $Q^2 > 1$  (GeV/c)<sup>2</sup> while the latter one removes radiative events difficult to describe for  $y > 0.9$  and events difficult to handle in the reconstruction due to the low momentum for  $y < 0.1$ . The distributions of the retained DIS events are given in Table 3.3 and represent 0.6% of the initial statistics. The kinematic distribution are shown in Figs. 3.6 and 3.7 after all selection criteria but the one on

the displayed variables.

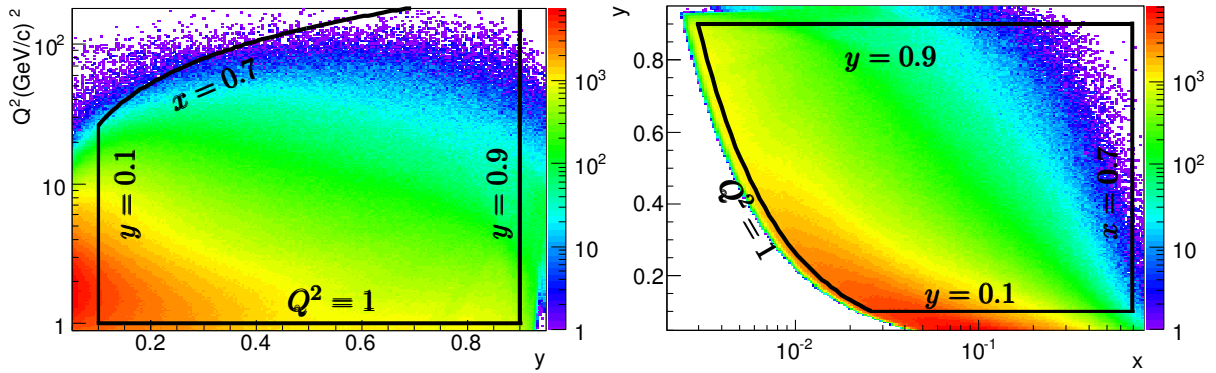


Figure 3.6: Distributions of  $Q^2$  vs  $y$  (left) and  $y$  vs  $x$  (right). Kinematic cuts for selecting DIS events are represented by the black lines.

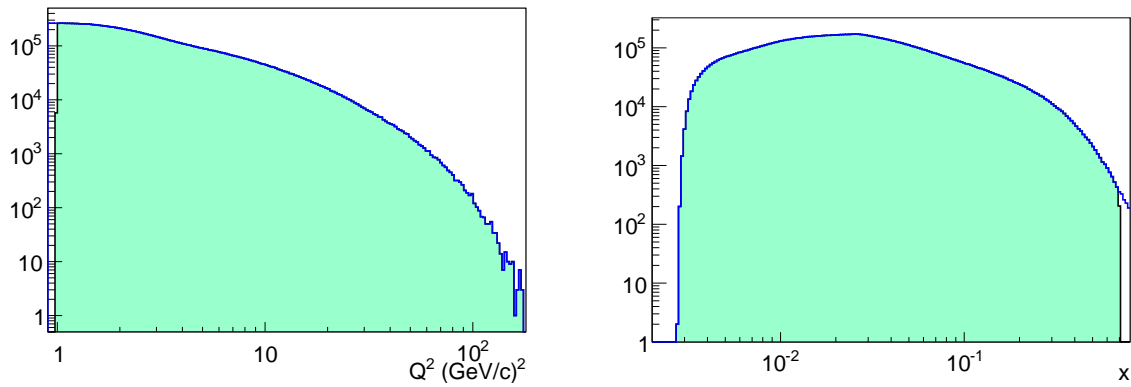


Figure 3.7: Distributions of  $Q^2$  (left) and  $x$  (right). Kinematic cuts for selecting DIS events are represented by the black lines.

Table 3.3: Summary of the suppression factors for the final sample. The last two rows indicate the trigger contributions.

Cut	Events/10 <sup>6</sup>	(%)
# Reconstructed events	12940	100.00
Presence of primary vertex	7921	61.21
Presence of a scattered muon	1955	15.10
$Q^2 > 0.9 \text{ (GeV}/c)^2$	202	1.56
Withdrawal of bad spills	174	1.34
Withdrawal of runs without target polarisation measurements	173	1.33
$ E_{beam} - 200  < 20 \text{ GeV}$	173	1.33
Beam particle without reconstructed momentum	171	1.32
$\sum_h z_h < 1$	170	1.31
$Q^2 > 1 \text{ (GeV}/c)^2$	159	1.23
$0.0025 < x < 0.7$	156	1.21
$0.1 < y < 0.9$	99	0.77
Extrapolated muon beam crosses all cells	96	0.74
Presence of the primary vertex inside the target	78	0.60
# events from purely inclusive triggers	65	84.4
# events from semi-inclusive triggers	12	15.6

### 3.5 Computation of the spin asymmetry

The number of events  $N_{cell}$  for each target polarisation is related to the asymmetry through Eq. (3.3). It consists of the beam flux  $\phi$ , the acceptance of the cell  $a_{cell}$ , the density of material in the cell  $n_{cell}$  and the unpolarised DIS cross-section  $\sigma_0$ . This first part in the right hand side describes the number of events averaged over polarisation states for a given cell. The second part consisting of the asymmetry describes the magnitude of the excess or of the deficit of events depending on the spin state. This asymmetry  $A_1^p$  is weighted by the beam polarisation  $P_b$  and the target cell polarisation  $P_{t_{cell}}$  to give the direction of the effect and its magnitude. A dilution factor  $f$  and a depolarisation factor  $D$  are also introduced to correct for the effective proton and photon polarisations.

$$N_{cell} = \phi a_{cell} n_{cell} \sigma_0 (1 + P_{t_{cell}} P_b f D A_1^p) \quad (3.3)$$

The dilution factor represents the fraction of polarisable material within the target. In order to evaluate this quantity in the most realistic way Eq. (3.4), the number of nuclei  $n_A$  (with mass number  $A$ ) present in the target is weighted by its total unpolarised cross-section  $\sigma_A^{tot}$ .

$$f = \frac{n_p \sigma_p^{tot}}{\sum_{A \in target} n_A \sigma_A^{tot}} \quad (3.4)$$

The total cross-section comprises the one-photon-exchange cross-section (Born approximation)  $\sigma^{1\gamma}$  and higher order QED radiation effects Eq. (3.5):

$$\sigma^{tot}(x, Q^2) = \nu \sigma^{1\gamma}(x, Q^2) + \sigma^{el}(x, Q^2) + \sigma^{qel}(x, Q^2) + \sigma^{inel}(x, Q^2) \quad (3.5)$$

where the  $\nu$  factor stands for the vertex and the vacuum polarisation radiation and  $\sigma^{el}$ ,  $\sigma^{qel}$  and  $\sigma^{inel}$  represent the elastic, quasi-elastic and inelastic scattering respectively. The Feynman

diagrams corresponding to Bremsstrahlung in the elastic and inelastic cross-section, vertex correction and vacuum polarisation are given in Fig. 3.8. For semi-inclusive triggers the second and third contributions ( $\sigma_A^{el}$  and  $\sigma_A^{qel}$ ) in Eq. (3.5) vanish, since the detected hadron in the final state ensures the inelasticity of the reaction. The effective dilution factor in Eq. (3.3) is

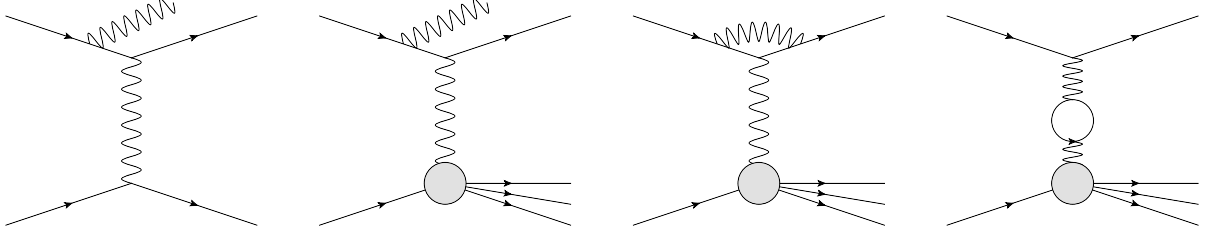


Figure 3.8: From left to right, Feynman diagrams of the radiative processes for the elastic tail, the inelastic tail, the vertex correction and the vacuum polarisation.

already corrected for those diluting radiative effects by the additional factor  $\rho$  from Eq. (3.6), which is evaluated from precalculated tables obtained with TERAD [48].

$$\rho(x,y) = \nu\eta = \nu \frac{\sigma_p^{1\gamma}}{\sigma_p^{tot}} \quad (3.6)$$

The dilution factor is trigger and kinematic dependent as shown in Fig. 3.9. At low values of  $x$  (*i.e.* low values of  $Q^2$ ), the dilution factor is larger for the semi-inclusive triggers than for the inclusive ones, since the hadron detected in the final state ensured the inelasticity of the reaction.

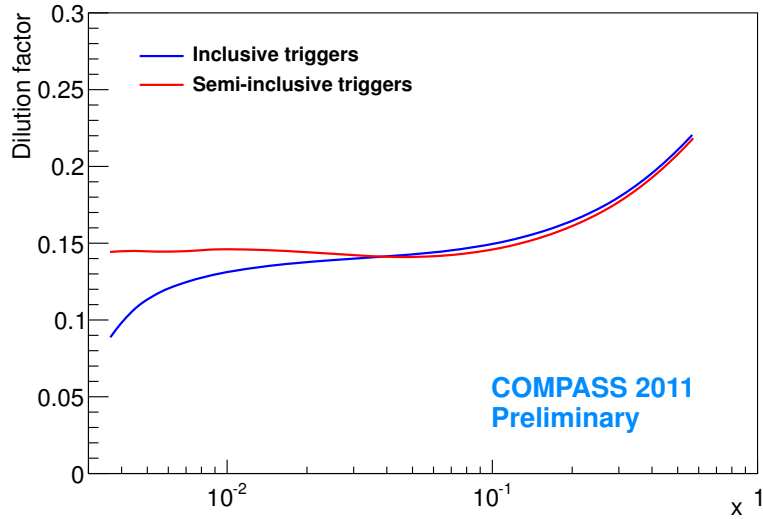


Figure 3.9: Dilution factor with radiative correction included as a function of  $x$  for inclusive and semi-inclusive triggers.

The depolarisation factor is defined as in Eq. (3.7):

$$D = \frac{y((1 + \gamma^2 y/2)(2 - y) - 2y^2 m^2/Q^2)}{y^2(1 - 2m^2/Q^2)(1 + \gamma^2) + 2(1 + R)(1 - y - \gamma^2 y^2/4)} \quad (3.7)$$

It represents the transfer of polarisation from the beam to the virtual photon [49, 50]. It mostly depends on the kinematic of the virtual photon and on the ratio of the longitudinal cross-section to the transverse one,  $R(x, Q^2)$  [51].  $D(y)$  increases with  $y$  which means that high photon energies correspond to high photon polarisations.

### 3.5.1 Intuitive Asymmetry extraction

By combining the numbers of events from Eq. (3.3) for the upstream and downstream cells  $N_{u+d}$  and those of the central cell  $N_c$ , which correspond to the two opposite target polarisations, one obtains Eq. (3.8):

$$\frac{N_{u+d} - N_c}{N_{u+d} + N_c} = \frac{r - 1 + w A_1^p (r|P_{u+d}| + |P_c|)}{r + 1 + w A_1^p (r|P_{u+d}| - |P_c|)} \quad (3.8)$$

where  $w = P_b f D$  and  $r = a_{u+d} n_{u+d} / a_c n_c$  is the ratio of the acceptance for the upstream and downstream cells to the acceptance of the central one. The unpolarised cross-section cancels in the ratio as well as the beam flux thanks to the cut on the extrapolation of the beam tracks along the target.

Typically  $w A_1^p \ll 1$  and  $|r - 1| < 0.1$  for inclusive measurements so that one can simplify Eq. (3.8) under reasonable assumptions to obtain:

$$\frac{1}{w \langle P \rangle} \cdot \frac{N_{u+d} - N_c}{N_{u+d} + N_c} = A_1^p + \underbrace{\frac{1}{w \langle P \rangle} \cdot \frac{r - 1}{r + 1}}_{\text{acceptance bias}} \quad (3.9)$$

where  $\langle P \rangle$  is the average value of the modulus of the target polarisation. The physical asymmetry appears to be biased by an asymmetry of acceptance. To overcome this bias, the spin states of the different target cells are regularly flipped by means of a rotation of the solenoid magnetic field as described in section 2.2. After a field rotation, the Eq. (3.9) can be written again with only an opposite sign before the physical asymmetry. By doing the difference between the measurements before and after a field rotation, the apparatus asymmetry cancels out. In fact, the difference is computed at the Eq. (3.3) level, before making the simplifying approximations which lead to Eq. (3.9), and results in Eq. (3.10) when only terms at first order in  $A_1^p$  are kept and assuming identical  $r$  factor before and after a field rotation.

$$A_1^p = \frac{1}{2} \cdot \frac{1}{1 - \alpha^2} \cdot \frac{1}{\langle P_B P_T f D \rangle} \cdot \left( \frac{N_{u+d} - N_c}{N_{u+d} + N_c} - \frac{N'_{u+d} - N'_c}{N'_{u+d} + N'_c} \right) \quad (3.10a)$$

$$\delta A_1^p = \frac{1}{2} \cdot \frac{1}{\sqrt{1 - \alpha^2}} \cdot \frac{1}{\langle P_B P_T f D \rangle} \cdot \sqrt{\frac{1}{N_{u+d} + N_c} + \frac{1}{N'_{u+d} + N'_c}} \quad (3.10b)$$

The primed and unprimed quantities stand for before and after a field rotation and  $\alpha$  is a factor accounting for a non perfect acceptance cancellation.

Typically, for the inclusive asymmetry,  $\alpha$  is very small (order of 1%) and can be neglected; This is not the case for semi-inclusive asymmetries (where an identified hadron in the final state is recorded in addition to the scattered muon) where values up to 50% can be reached. For that reason, another method, less dependent on the acceptance discrepancies, is used and is introduced in the next section.

### 3.5.2 Second order weighting method

This method was introduced by SMC then adapted to COMPASS and largely described in [52, 53], hence only the outline is recalled. The number of events defined in Eq. (3.3) is

integrated over all dependent variables but the ones binned in the asymmetry (typically  $x$  and  $Q^2$ ) with a weighting factor  $w = fP_bD$ . The weight takes better into account events with a large polarisation transfer than the diluted ones. Equation (3.3) can be rewritten as Eq. (3.11):

$$p_{cell} = \int N_{cell} w dX = \int \phi \sigma_0 n_{cell} dX \langle a_{cell} \rangle (1 + \langle \beta_{cell} \rangle A_1^p) \quad (3.11)$$

where  $dX$  is the measure of all unbinned variables,  $\beta = wP_{cell}$  and

$$\langle a_{cell} \rangle = \frac{\int \phi \sigma_0 n_{cell} a_{cell} w dX}{\int \phi \sigma_0 n_{cell} w dX} \quad (3.12a)$$

$$\langle \beta_{cell} \rangle = \frac{\int \phi \sigma_0 n_{cell} a_{cell} \beta_{cell} w dX}{\int \phi \sigma_0 n_{cell} a_{cell} w dX} \quad (3.12b)$$

are the weighted average of acceptance and of polarisation product. Instead of the arithmetic average, the geometric average of  $N_{u+d}$ ,  $N_c$  and  $N'_{u+d}$ ,  $N'_c$  is computed:

$$\underbrace{\frac{p_{u+d} \cdot p'_c}{p'_{u+d} \cdot p_c}}_{\delta} = \underbrace{\frac{\langle a_{u+d} \rangle \langle a'_c \rangle}{\langle a'_{u+d} \rangle \langle a_c \rangle}}_{\kappa \text{ factor}} \cdot \frac{(1 + \langle \beta_{u+d} \rangle A_1^p)(1 + \langle \beta'_c \rangle A_1^p)}{(1 + \langle \beta'_{u+d} \rangle A_1^p)(1 + \langle \beta_c \rangle A_1^p)} \quad (3.13)$$

Assuming the double ratio of the average value of acceptances  $\kappa$  is equal to 1 like for the intuitive method, the physical asymmetry is one of the roots of the second order equation (3.13). The statistical uncertainty on  $A_1^p$  is obtained by taking the derivative of Eq. (3.13) with respect to  $\delta$  and propagating the uncertainty. The uncertainty on  $\delta$ , Eq. (3.14), is obtained by propagating the uncertainties on  $p_{cell}$  which follows a Poisson law.

$$\sigma_\delta^2 = \frac{1}{\sum_{i \in u+d} w_i^2} + \frac{1}{\sum_{i \in c} w_i^2} + \frac{1}{\sum_{i \in u+d} w_i'^2} + \frac{1}{\sum_{i \in c} w_i'^2} \quad (3.14)$$

### 3.5.3 Radiative corrections

The proton asymmetry  $A_1^p$  is given in the one-photon-exchange approximation  $\sigma_{\mu p}^{1\gamma}$ . The measured cross section  $\sigma_{\mu p}^{meas}$  contains contributions coming from the elastic, quasi-elastic and inelastic tails as well as from the vertex correction and the vacuum polarisation :

$$\sigma_{\mu p}^{meas} = \sigma_{\mu p}^{1\gamma} + \sigma_{\mu p}^{other} \quad (3.15)$$

In the asymmetry, all contributions stay in the denominator while only spin-dependent parts remain in the numerator.

$$A_1^{meas} = \frac{\Delta\sigma_{\mu p}^{1\gamma} + \Delta\sigma_{\mu p}^{other}}{\sigma_{\mu p}^{meas}} \quad (3.16)$$

The corrections for these extra contributions are applied in two steps, one for the unpolarised part and one for the polarised part. The first step corrects for the dilution of the denominator by radiative events and is included in the dilution factor calculation (see Eq. (3.6)).

A second correction ( $A_{RC}$  which is small) removes the contribution of  $\Delta\sigma_{\mu p}^{other}$ . It is evaluated in  $x$  and  $Q^2$  bins by an iterative method with the POLRAD program [54]. Indeed the latter

contribution depends also on the knowledge of the asymmetry. It is re-evaluated until Eq. (3.17) converges (where  $A^{(k)}$  is the corrected asymmetry after the  $k^{th}$  step).

$$A^{(k)} - A^{(k-1)} = \frac{\Delta\sigma_{\mu p}^{other}(A^{(k-1)})}{\sigma_{\mu p}^{1\gamma}} \xrightarrow{\text{converge}} A_{RC} \quad (3.17)$$

Finally,

$$A_{1\gamma}^{\mu p} = \frac{A_1^{meas}}{\rho} - A_{RC} \quad (3.18)$$

Figure 3.10 shows the size of the radiative corrections to subtract from  $A_1$  as well as the ratio to the statistical uncertainty for beam energies at 160 GeV and 200 GeV. As expected the corrections are small ( $<0.03$ ) but not negligible compared to the accuracy of the measurements where it contributes up to about  $1\sigma$  at moderate  $x$ .

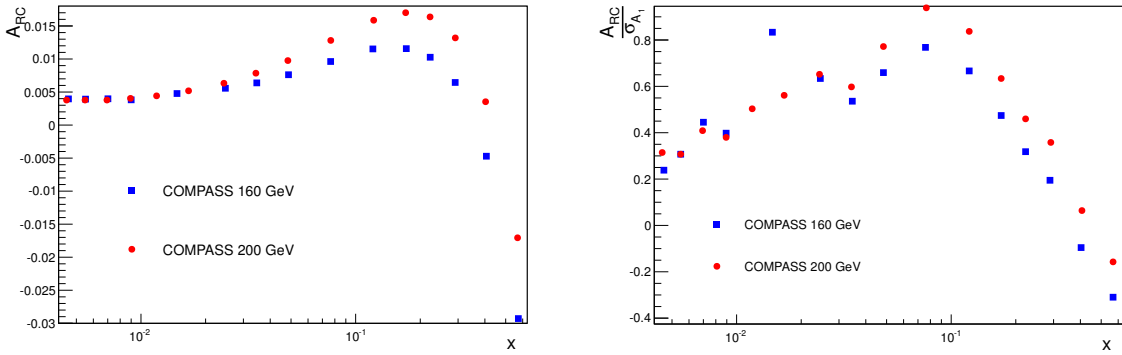


Figure 3.10: (a): Radiative corrections  $A_{RC}$  to subtract from  $A_1$  for 200 GeV and 160 GeV data as a function of  $x$ . (b): Ratio as a function of  $x$  of the radiative corrections  $A_{RC}$  to the statistical uncertainty on  $A_1$ .

### 3.5.4 $^{14}\text{N}$ polarisation correction

The measurements are done using an ammonia target ( $^{14}\text{NH}_3$ ), which implies a little contamination of the asymmetry of the proton  $A_1^p$  due to the presence of nitrogen Eq. (3.19), where  $N_X$ ,  $\sigma_X$  and  $P_X$  are the number density, the unpolarised cross-section and the polarisation of the X element respectively.

$$A_1^{meas} = A_1^p + \frac{N_{^{14}\text{N}}}{N_H} \frac{P_{^{14}\text{N}}}{P_H} \frac{\sigma_{^{14}\text{N}}}{\sigma_H} A^{^{14}\text{N}} \quad (3.19)$$

In the shell model, the nitrogen can be modeled as a carbon spinless core with a proton and a neutron [40] so that the nitrogen contribution can be rewritten as:  $A^{^{14}\text{N}} \sigma_{^{14}\text{N}} = \beta_{^{14}\text{N}} g_{^{14}\text{N}} (A^p \sigma_p + A^n \sigma_n)$ , where the terms  $\beta_{^{14}\text{N}}$  and  $g_{^{14}\text{N}}$  correct for the nuclear effects and the EMC effect respectively. The proton and the neutron contributions can also be expressed in terms of deuteron asymmetry according to the relation:  $A_1^d \sigma_d = \omega_D (A_1^p \sigma_p + A_1^n \sigma_n)$ , where  $\omega_D$  corrects for the D-state of the deuteron. Reshuffling the equations, one ends with a correction to subtract from the measured asymmetry in Eq. (3.20). The first factor accounts for the ratio of the number of nuclei of  $^{14}\text{N}$  to that of  $H$ , the second one for the fact that the nucleon spin is anti-aligned to the  $^{14}\text{N}$  one third of the time and the last factor stands for the relative polarisation of the  $^{14}\text{N}$  with respect to the protons [55, 28].

$$\Delta A_1^p = \left(\frac{1}{3}\right) \cdot \left(-\frac{1}{3}\right) \cdot \left(\frac{1}{6}\right) \cdot \frac{\sigma_d}{\sigma_p} A_1^d \quad (3.20)$$

A fit to the COMPASS deuteron data with a power-law function has been performed to obtain a parametrisation of  $A_1^d$  in order to evaluate  $\Delta A_1^p$  in Eq. (3.20). The magnitude of the correction, which increases the asymmetry, is plotted in Fig. 3.11. Although the correction for the

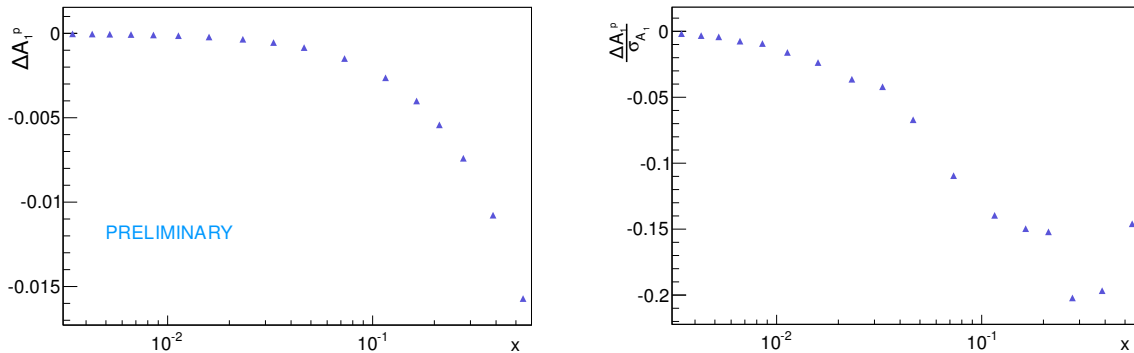


Figure 3.11: (a):  $^{14}\text{N}$  correction to be subtracted from  $A_1^p$  as a function of  $x$ . (b): Ratio of the  $^{14}\text{N}$  correction to the statistical errors of  $A_1^p$ .

polarisation of the  $^{14}\text{N}$  nitrogen is found to be small in absolute value, it still represents 20% of the statistical uncertainty at high  $x$  and is not negligible.

### 3.6 Systematic studies: Search for biases and false asymmetries

As the physical asymmetry is heavily diluted ( $fDP_bP_t$  amounts typically to 6%), a good knowledge of the various sources of systematics is needed. Several tests, using either Monte-Carlo data or real data, have been carried out in order to quantify possible false asymmetries. None of them reveal the presence of a false asymmetry larger than the statistical accuracy. A partial review of the performed tests is presented.

#### 3.6.1 Estimates based on a Monte-Carlo simulation

The Monte-Carlo simulation comprises a complete description of the apparatus and the modelisation of the physical process of interest, DIS.

The different steps of the Monte-Carlo chain are:

- The generation of Deep Inelastic Scattering events based on LEPTO generator [56].
- The description of the apparatus effected through COMGeant, a COMPASS derivative of GEANT toolkit [57].
- The reconstruction of the events realised by CORAL, the COMPASS software of reconstruction [32].

#### Smearing in $x$

The finite resolution of the spectrometer on the momentum reconstruction of the incident and scattered muons introduces an uncertainty on  $Q^2$  and on  $x$ . Since the  $Q^2$  dependence of the asymmetry is rather weak, the smearing in  $Q^2$  is expected to produce negligible effects and is omitted from the description of the method of propagation given below. As the  $x$  distribution shows two slopes (Fig. 3.7), one in the low  $x$ -region and one in the large  $x$ -region, the smearing

in  $x$  leads to a bin migration of the asymmetry towards low  $x$  in the low  $x$  region and towards high  $x$  in the high  $x$  region. Since the asymmetry is rather constant at low  $x$ , the smearing effect is not expected to be important. In contrast, at high  $x$  a dilution of the asymmetry is expected.

To quantify the effect, for each reconstructed event the asymmetry is always computed with the generated kinematics and fills a bin in  $x$  in two histograms. One with the generated kinematics and the second with the reconstructed kinematics. The average value over all events of the asymmetry is then computed in each bin of  $x$ . Figures 3.12 and 3.13 show the comparison between the asymmetry without smearing and the asymmetry obtained by the method described above representing a smearing of about 5% in  $x$  and  $Q^2$ . The two curves are not distinguishable and the smearing in  $x$  and  $Q^2$ , which at most in the last bin represent 1.5% of  $A_1$ , can be neglected.

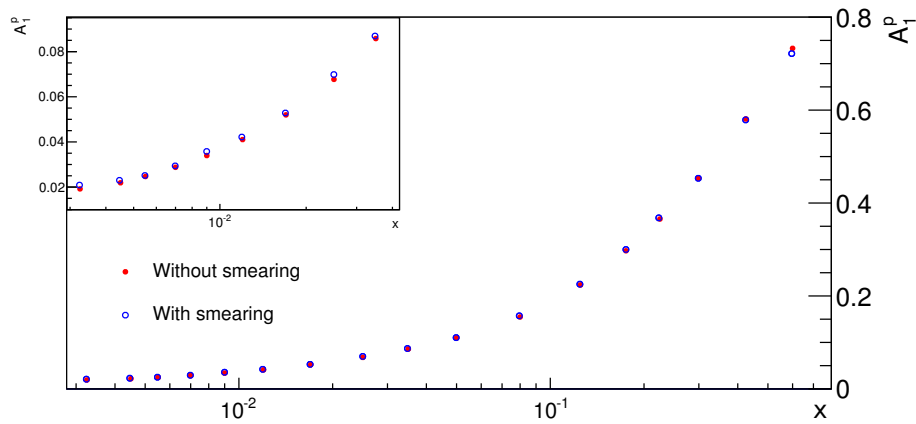


Figure 3.12: Effect of a smearing in  $x$ ,  $Q^2$ . The asymmetry without smearing is represented in red, the one with the effect of smearing in blue. The inset is a zoom of the low  $x$  region (MC study).

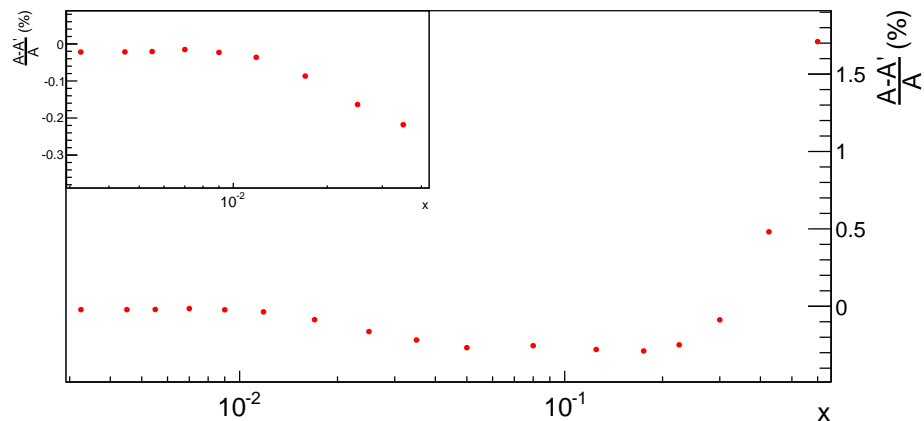


Figure 3.13: Difference of the asymmetry without ( $A$ ) and with ( $A'$ ) smearing effects compared to the asymmetry as a function of  $x$ . The results are given in percentage with an enlarged inset to show the low  $x$  region (MC study).

### Solenoid field

The fringe field of the solenoid in which the target is embedded extends over the closest detectors and affects their performance. Its effect can create a difference of acceptance between the two field orientations. In the past, the 2.5 T solenoid field used to polarise the target was reduced to a holding field of 1 T during the data taking to diminish this risk. However, to reduce the drawback of target polarisation build-up, in 2011 the data were taken with a 2.5 T field for the first time. The Monte-Carlo simulation is used to compare the kinematic distributions obtained using a 2.5 T field and a 1 T field. The impact on the asymmetries was also studied. In Fig. 3.14 is shown  $A_1^p$  computed from Monte-Carlo data combining events produced for the two directions of the solenoid field as it is the case for the real data. Since the event generator is unpolarised, a null asymmetry is expected. The distribution is compatible with zero with a  $\chi^2$  probability of 95%. The good compatibility with zero within the statistical fluctuation does not reveal the presence of solenoid field effects.

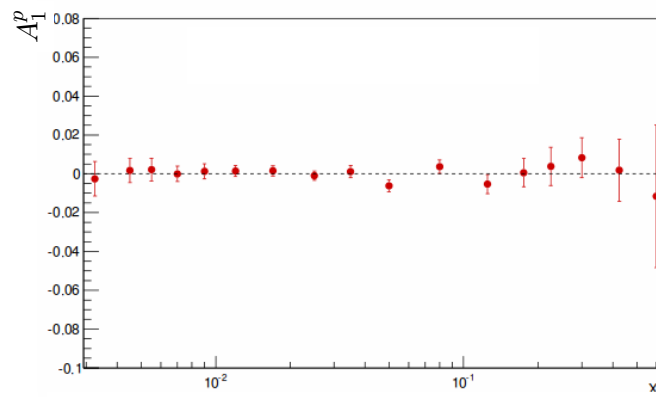


Figure 3.14: Asymmetry computed from unpolarised MC data as a function of  $x$  (MC study).

### Trigger bias

Part of the events used to compute the inclusive asymmetry are recorded using a semi-inclusive trigger. This fact introduces a bias in the inclusive asymmetry extraction depending on the efficiency of the calorimeters in detecting hadrons according to their charge. Higher efficiency of detecting charged hadrons causes a raise of scattering off u quarks (which are expected to be positively polarised) compared to d quarks (negatively polarised). This results in a larger asymmetry with an effect which is emphasised in the large  $x$  region (low values of  $W$ ) where the calorimetric condition of the trigger may most likely be fulfilled by the leading hadron. A Monte-Carlo simulation with POLDIS event generator was used to quantify the effect. SMC showed (Fig. 3.15) that the difference of the asymmetry computed from inclusive events  $A_1^i$ , and “semi-inclusive” events  $A_1^h$  was negligible compared to the statistical precision of the data [58]. The same conclusion based on their results can be preliminary drawn for this analysis. The same method based on Monte-Carlo study is being investigated to confirm the SMC observation in the COMPASS trigger conditions.

### 3.6.2 Estimates based on real data

#### Wrong spin configuration association

As it was presented in sections 3.1.3 and 3.5.1, the data are grouped into small samples separated in time by a solenoid field rotation (Fig. 3.16) to cancel out the false asymmetry from

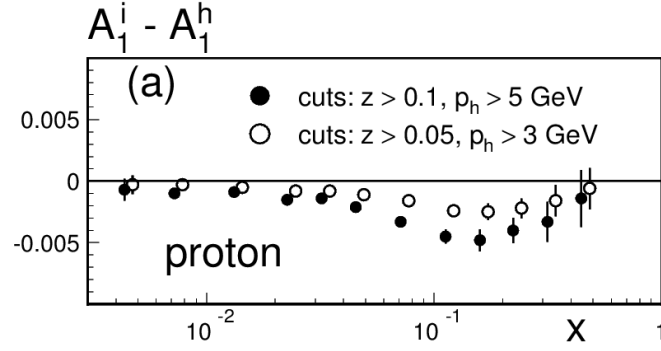


Figure 3.15: Difference of the asymmetry computed for the inclusive DIS events and for the semi-inclusive DIS events. The latter is a subsample of the former that at least contains a hadron surviving cuts on the hadron fractional energy ( $z$ ) and on the hadron momentum. Results are shown for two sets of cuts (MC study).

the apparatus. A way to estimate the contribution of this false asymmetry is to combine data separated by the two solenoid field rotations. The physical asymmetry is expected to be null and any deviation from zero is due to acceptance differences. About 100 of groups of data were created. For each group, the false asymmetry  $A_i^{fake}(x)$  and the  $\chi_1^2 = (A_i^{fake}/\sigma_i)^2$  for each bin in  $x$  are calculated. The distribution of  $\chi_1^2$  values for each  $x$ -bin is shown in Fig. 3.17. If no false asymmetry is present, the distributions follow the  $\chi_1^2$  probability density function. However, in case of a false asymmetry each  $\chi_1^2$  follows a non-central chi-squared distribution  $\chi_{1,\mu}^2$ . As each group has different statistics, each  $A_i^{fake}(x)$  follows a different  $\chi_{1,\mu}^2$ -distribution. Nevertheless, assuming that the false asymmetry is the same for all groups and that each  $\sigma_i$  is perfectly known, the sum of the  $\chi_{1,\mu}^2$ -distributions can be fitted with only one parameter  $\mu$  defining the amplitude of the false asymmetry. The result of the fit to each  $x$ -bin is shown as a blue line in Fig. 3.17. The value of  $\mu$  and its error are given in the top part of each pad. Most of the values are fully compatible with a null false asymmetry but for two  $x$ -bins the compatibility with zero is of about  $2.6 \sigma_\mu$ . As the  $x$ -bins are correlated, in case of a false asymmetry coming from the apparatus, several consecutive  $x$ -bin should be affected. No trend is observed in any  $x$ -bin and the effect on the two tendentious  $x$ -bins is isolated suggesting a statistical fluctuation. The fits were also performed with  $\mu$  set to zero in order to see the compatibility with a null false asymmetry hypothesis and for all  $x$ -bins the probability of  $\chi^2$  was found to be at least above 7%.

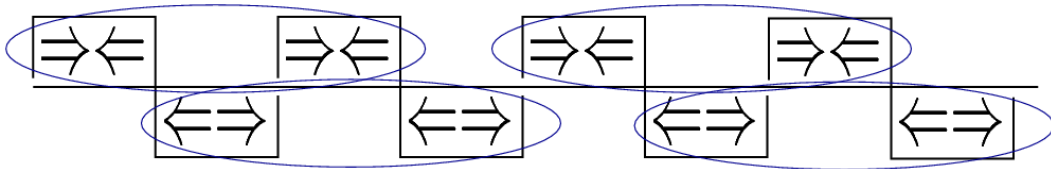


Figure 3.16: Illustration of the so called fake configuration (wrong association of spin states). Each rectangle represent the spin state of a two cell target at a given time. Time goes from left to right. Going from a row to another corresponds to a solenoid field rotation (flip of the spin states). The blue ellipses show how the data are combined to compute asymmetry in this fake configuration.

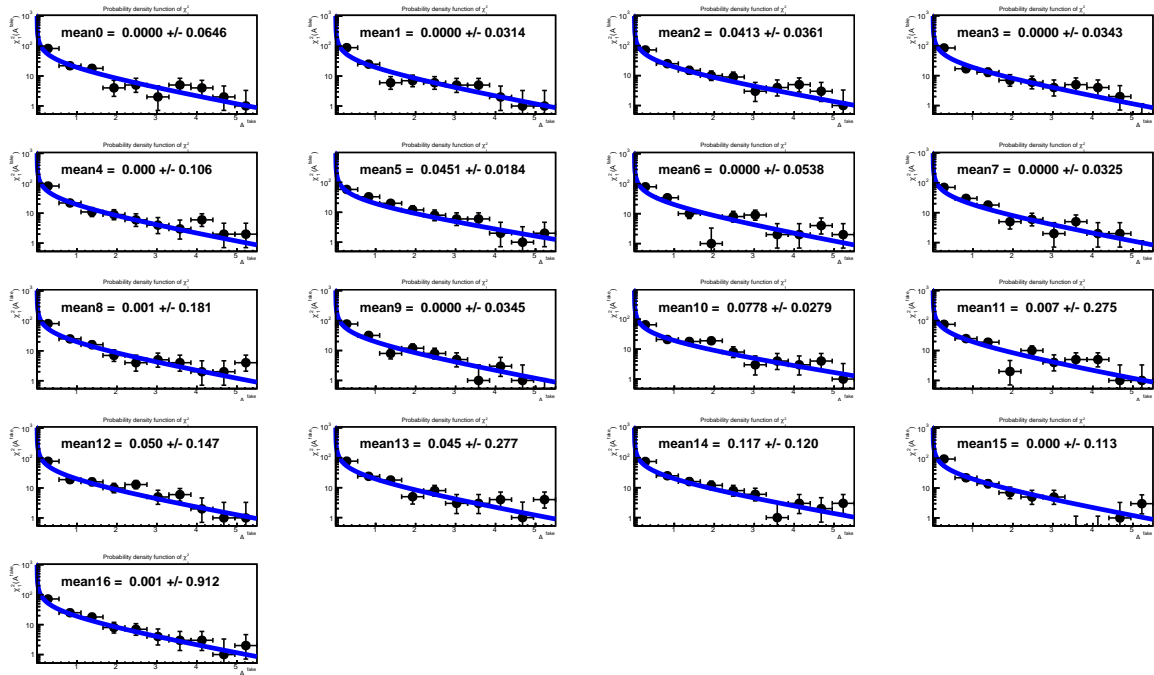


Figure 3.17:  $(A_1/\sigma)^2$  distributions for asymmetries computed with the wrong spin configuration associations.  $\chi^2_{1,\mu}$  distributions are fitted to the data (blue lines) to estimate the value of  $\mu$  (given in each pad).

### Target polarisation homogeneity

In order to check the homogeneity of the target polarisation, two false asymmetries are computed by using events from the cells with the same spin state. In other words, the asymmetry between events from the upstream and the downstream cells is compared to the zero expected value. The same is done using events from the two halves of the central cell. Any deviation from zero would reveal a problem with the target polarisation or acceptance issues after a solenoid field rotation. To reduce the effect of differences of acceptance, the setup of three cells is artificially rebuilt: the central cell is divided into 3 parts, the central part being twice as long as the extreme parts. The first and the last parts represent a fake upstream cell and a fake downstream cell while the part in the middle represents the fake central cell. A similar procedure is applied to the upstream and downstream cells. They are divided into two and the first part of the upstream cell stands for the fake upstream cell, the last part of the downstream cell for the fake downstream cell and the last part of the upstream cell is merged with the first part of the downstream cell to form the fake central cell. The results of these false asymmetries are shown in Fig. 3.18, they are consistent with zero with a  $\chi^2$  probability of 19% and 82% for the upstream-downstream and central-central tests respectively and no inhomogeneity of polarisation is found within the statistical fluctuations.

### Anisotropy of the spectrometer

The aim of this study is to verify the homogeneity of the efficiency of the spectrometer, the alignment of the detectors and thus possible changes in acceptance. Depending on the direction of the scattered muon, the data are separated in two samples. In a first test, the two samples consist of the data where the scattered muons go in the upper or in the lower part of the spectrometer. In a second test, the samples are made up of data where the scattered muons go to the left or to the right part of the spectrometer. From these samples and unlike in the

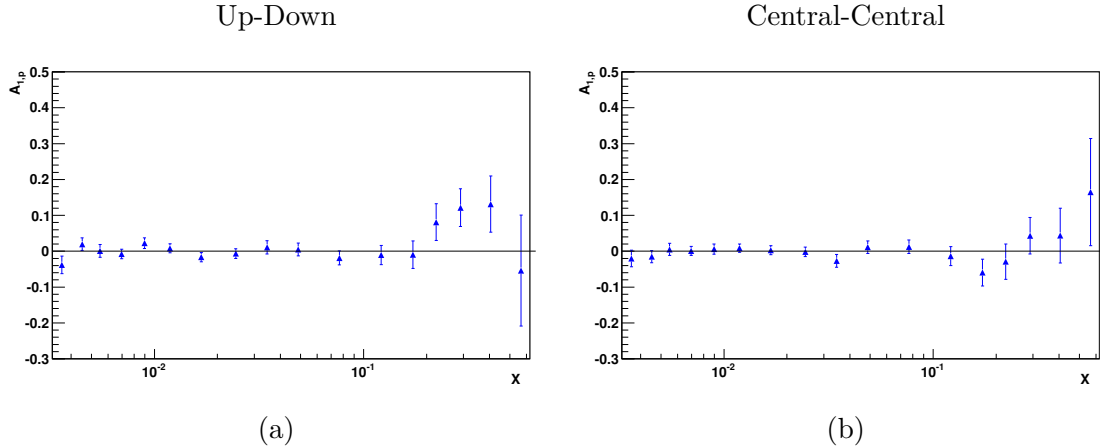


Figure 3.18: Upstream-downstream (a) and central-central (b) false asymmetries.

previous tests, physical asymmetries are computed. Therefore, the relevant quantities are the differences between the asymmetries computed for the top and bottom samples, and between the ones computed for the left and right samples. Figures 3.19a and 3.19b show the result for the two cases. The  $\chi^2$  probability for a zero false asymmetry is 46% (10%) for the top-bottom (left-right) asymmetry. The good compatibility with zero within the statistical fluctuation does not reveal the presence of a false asymmetry.

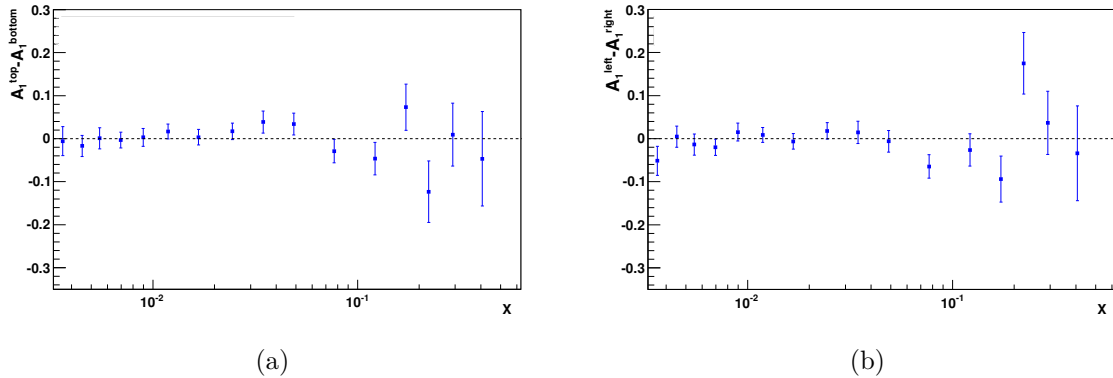


Figure 3.19: Difference of asymmetries top-bottom (a) and left-right (b) compared to zero.

### Correlation between acceptances and solenoid field

As mentioned in section 3.5.1, to cancel out the apparatus false asymmetry, a solenoid field rotation is performed once a day. This rotation introduces a correlation between the direction of the solenoid field and the acceptance. To suppress this correlation, at least once a year the target is completely depolarised and polarised again with different microwave frequencies (section 2.2) for the different cells, in order to obtain an opposite spin state for a same direction of the solenoid field. To estimate the size of the possible false asymmetry remaining after this procedure, the physical asymmetry for each microwave setting (denoted  $A^+$  and  $A^-$  respectively in the following) is computed. Half the difference of the two represents the false asymmetry due to the correlation between the acceptance and the direction of the solenoid field. This residual false asymmetry is the fraction of the false asymmetry which is not cancelled due to

unbalanced statistics in the two microwave settings Eq. (3.21).

$$A_{res}^{false} = \frac{(\delta A^+)^2 - (\delta A^-)^2}{(\delta A^+)^2 + (\delta A^-)^2} \cdot \frac{A^+ - A^-}{2} \quad (3.21)$$

Table 3.4 shows the group of the 2011 periods with the two microwave settings. The result of the  $A^+$  and  $A^-$  measurements for the inclusive asymmetry is shown in Fig. 3.20. The difference between the two microwave settings is already compatible with zero with a  $\chi^2$  probability of 42%. The false asymmetry due to the correlation between the solenoid field and the acceptance is then negligible.

+							-				
W25	W27	W30	W31	W32	W33	(W34)	W36	W38	W39	W41	W43

Table 3.4: Sharing of data between the two microwave settings.

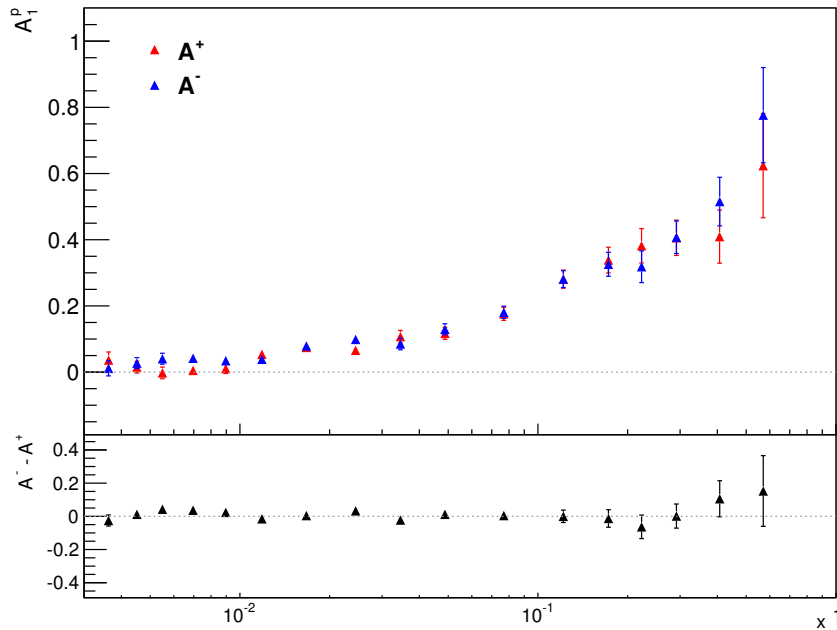


Figure 3.20: Comparison of  $A_1^p$  for both microwave settings (red and blue). The bottom part of the figure displays the difference between the two settings.

### Compatibility in time

Finally, the self-consistency of the data is studied. The physical asymmetry is computed for each group of data and noted  $A_i$  for the group number  $i$ . The distribution of these asymmetries recentred by the sample average and normalised by the statistical uncertainty must follow a normal distribution.

$$\Delta r = \frac{A_i(x) - \overline{A(x)}}{\sqrt{\sigma_i^2 - \sigma_A^2}} \rightsquigarrow \mathcal{N}(0,1) \quad (3.22)$$

In case of instabilities of the spectrometer (acceptance changes, efficiency drop, misalignment, etc), a broadening of the distribution would appear (due to underestimated uncertainties). The distributions associated to Eq. (3.22) is shown in Fig. 3.21 for each  $x$ -bin. Each distribution contains 78 entries and is fitted with a Gaussian distribution using the maximum likelihood estimator. All mean values and widths are compatible with zero and one, respectively, suggesting no systematic effects.

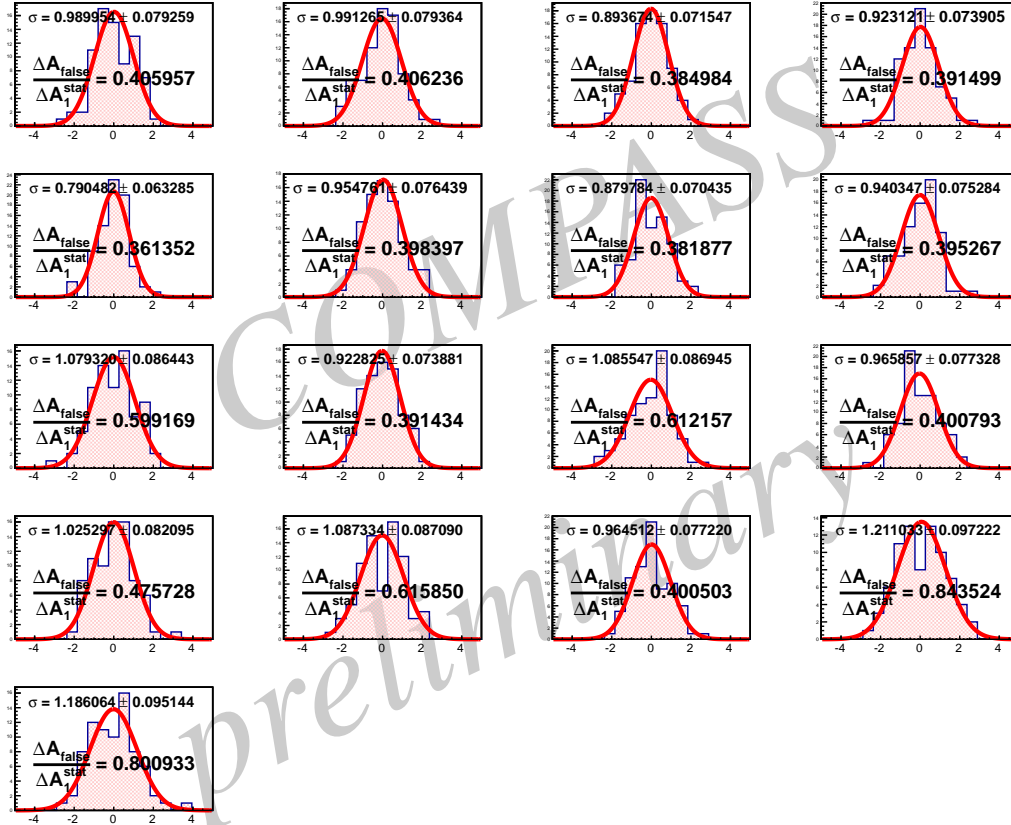


Figure 3.21: Distributions of the normalised residuals  $\Delta r$  (Eq. (3.22)). Each pad corresponds to an  $x$ -bin. Each entry in a histogram corresponds to a sample of data of a few days before and after a field rotation.

### Further checks

More checks, summarised below, were performed to evaluate the reliability of the data. An asymmetry has been computed with the events recorded during the night and those taken during the day. Temperature variations between day and night results in changes of thermal expansions and noise level in the detectors, which could have an effect on the asymmetry. The two asymmetries were found fully compatible with a  $\chi^2$  probability of 60%.

The asymmetry was also computed for each single trigger in order to check the stability of the detectors covering different domains of the phase-space. They were found fully compatible in the region of overlapping.

Finally, an asymmetry for each direction of the solenoid field has been evaluated. Although the acceptance difference between the target cells is cancelled out by the microwave reversal, the idea was to emphasise the correlation between the acceptance and the direction of the solenoid field. Here again the two asymmetries were found compatible with zero with a  $\chi^2$  probability of 46%.

### 3.6.3 External contributions

In addition to the apparatus uncertainties, the measurement of the asymmetry is subject to external contributions, which introduce additional uncertainties. Among these additional inputs, we report normalisation uncertainties such as the polarisation of the beam and of the target, the dilution factor of the target and the depolarisation factor. Moreover, uncertainties are assigned to the biases introduced by the polarised radiative correction as well as by neglecting the  $A_2$  asymmetry contribution.

#### Polarisation uncertainties

As mentioned in section 2.1, the beam polarisation is determined by a Monte-Carlo simulation describing the beam line. The relative uncertainties on the beam polarisation estimated by MC have been evaluated to 4% [59] when it was possible to compare the simulation to the measurement via a polarimeter. Since that time, the polarimeter has been removed and the beam line upgraded. A conservative value of 5% is taken for the uncertainty on the beam polarisation.

The uncertainties on the target polarisation [60] comprise the statistical uncertainties in the measurement of the polarisation as well as the systematics coming from the measurement of the temperature equilibrium and the measurements from the NMR coils. In total a relative uncertainty of 3.5% is estimated.

#### Uncertainties on the dilution and depolarisation factors

The uncertainty on the dilution factor,  $f$ , originates from the uncertainties on the target material [61] and on the total cross-sections. The contribution coming from the depolarisation factor,  $D$ , is mainly due to the uncertainty on  $R$ , the ratio of the longitudinal to transverse polarised photon absorption cross section.  $R$  is taken from a parametrisation based on the E143 fit to world data [51]. Three sources of uncertainties are taken into account: the statistical errors, the model dependence and the radiative corrections. In total, the relative uncertainty on the depolarisation factor is between 2 and 3 % depending on the kinematics.

#### Bias uncertainties

The contribution of the transverse asymmetry  $\eta A_2$  has been neglected from the extraction of  $A_1$  and an uncertainty taking into account this approximation is assigned to the systematics. According to the measurement of [4], a constant value of 0.05 was taken as an upper limit of  $A_2^p$  for all  $x < 0.4$  and 0.1 otherwise. This approximation results in a small uncertainty reaching at most 10% of the statistical uncertainty.

The uncertainties arising from the additive spin dependent radiative corrections  $A_{RC}$  come mainly from the input parametrisation of  $A_1^p$  implemented in the POLRAD program. The systematics assigned to  $A_{RC}$  comes from the variations of the corrections when the input parametrisation is varied inside its uncertainties. It represents at most 10% of the statistical uncertainties. Finally, the systematics coming from the estimation of the correction of the  $^{14}\text{N}$  contribution is estimated by the propagation of the uncertainties on the fit of  $A_1^d$  data. It corresponds to an uncertainty which is always below 3% of the statistical uncertainties and can easily be neglected when compared to the other sources of systematics.

### 3.6.4 Summary and calculation of the systematic error

The goal of the present analysis is to extract the one-photon-exchange asymmetry  $A_1^{1\gamma}$ :

$$A_1^{1\gamma} = \frac{1}{fDP_bP_t}A^{raw} - \left(\eta A_2 + A_{RC} + A_{false}\right). \quad (3.23)$$

This formula<sup>1</sup> uses  $f$ ,  $D$ ,  $P_b$ ,  $P_t$  and  $A_1^{RC}$  which are only known with limited precision. In addition  $A_2$  [62] is neglected and the uncertainties on the false asymmetry  $A_{false}$  must be estimated. All these factors contribute to the systematic error  $\sigma_{syst}$ . Let us divide  $\sigma_{syst}$  into two classes: multiplicative  $\sigma_{mult}$  and additive  $\sigma_{add}$ :

$$\sigma_{mult} = A_1 \sqrt{\left(\frac{\sigma_{P_b}}{P_b}\right)^2 + \left(\frac{\sigma_{P_t}}{P_t}\right)^2 + \left(\frac{\sigma_f}{f}\right)^2 + \left(\frac{\sigma_{D(R)}}{D(R)}\right)^2} \quad (3.24)$$

$$\sigma_{add} = \sqrt{(\sigma_{\eta A_2})^2 + (\sigma_{A_{RC}})^2 + (\sigma_{A_{false}})^2} \quad (3.25)$$

At the end these two terms are added in quadratures:

$$\sigma_{syst} = \sqrt{(\sigma_{mult})^2 + (\sigma_{add})^2} \quad (3.26)$$

To avoid a misunderstanding, we remind that the coefficient  $\rho$  ( $\rho = \nu\sigma_p^{1\gamma}/\sigma_p^{tot}$ ) was included into the dilution factor  $f$ , changing the meaning of  $A_1$  by transforming it into the asymmetry for the one-photon-exchange<sup>2</sup>  $A_1^{1\gamma}$ .

From the studies presented in section 3.6, no significant false asymmetries were found. The uncertainty on its presence is evaluated as follows.

The total uncertainties are defined as on the one hand:

$$(\sigma_{tot})^2 = (\sigma_{\Delta_r}^{syst})^2 + (\sigma_{\Delta_r}^{stat})^2 \quad (3.27)$$

and evaluated on the other hand as:

$$(\sigma_{tot})^2 = (\max\{\sigma_{\Delta_r}, 1\} + \delta\sigma_{\Delta_r})^2 \quad (3.28)$$

where  $\sigma_{\Delta_r}$  is the width of the normalised residual shown in Fig. 3.21 and  $\delta\sigma_{\Delta_r}$  its uncertainty. The equations 3.27 and 3.28 can then be reshuffled to obtain an upper limit for  $\sigma_{A_{false}}/\sigma_{stat}$ , which is given by  $\sigma_{\Delta_r}^{syst}$  for every  $x$ -bin [20]:

$$\sigma_{\Delta_r}^{syst} = \sqrt{(\max\{1, \sigma_{\Delta_r}\} + \delta\sigma_{\Delta_r})^2 - 1}. \quad (3.29)$$

The different contributions to  $\sigma_{syst}$  are summarised in Table 3.5. The fraction of the total systematic uncertainty from each contribution is shown as a function of  $x$  in Fig. 3.22. Although, all the tests were compatible with the absence of false asymmetry hypothesis, the dominant fraction is the one from the false asymmetry uncertainty for mostly the whole range in  $x$ . The sub-dominant contribution is from the beam polarisation uncertainty which is as significant as the dominant uncertainty in the middle  $x$ -range around 0.1. The values of each contribution for each bin in  $x$  are given in Table 3.6.

<sup>1</sup> $A^{raw}$  is the asymmetry of counts, *i.e.*  $\frac{N^{\uparrow\downarrow} - N^{\uparrow\uparrow}}{N^{\uparrow\downarrow} + N^{\uparrow\uparrow}}$ .

<sup>2</sup>For simplicity, the  $1\gamma$  index is omitted in the following.

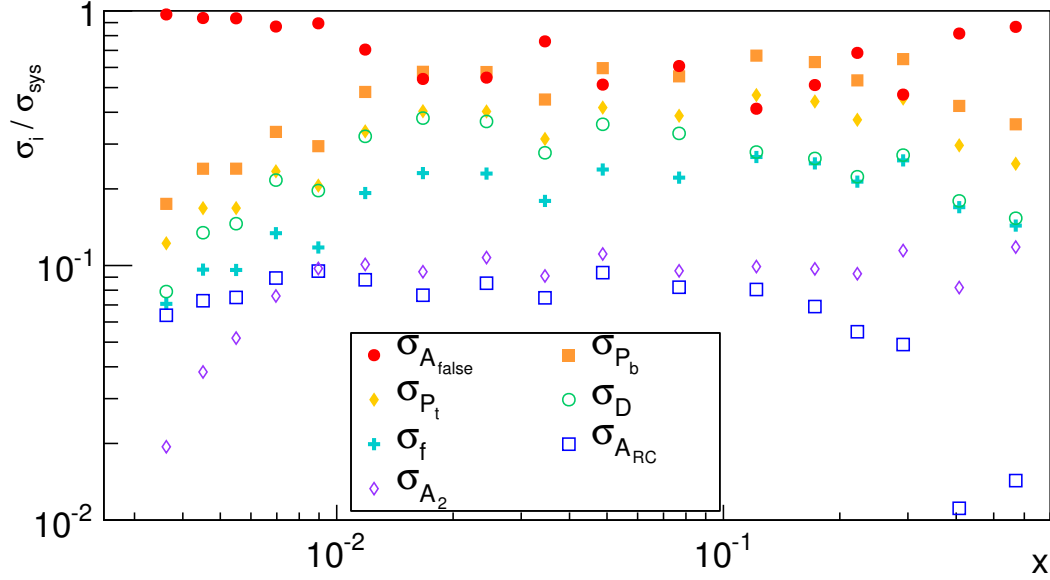


Figure 3.22: Fraction of the contribution of the different sources of systematics.

Table 3.5: Summary for the systematic error of  $A_1$ .

	Beam polarisation	$\sigma_{P_b}/P_b$	5%
Multiplicative variables error, $\sigma_{mult}$	Target polarisation	$\sigma_{P_t}/P_t$	3.5%
	Depolarisation factor	$\sigma_{D(R)}/D(R)$	2 – 3 %
	Dilution factor	$\sigma_f/f$	2 %
	Total		$\sigma_{mult} \simeq 0.07A_1^p$
Additive variables error, $\sigma_{add}$	Transverse asymmetry	$\sigma_{\eta \cdot A_2}$	$10^{-3} - 10^{-2}$
	Rad. corrections	$\sigma_{A_{RC}}$	$0.1 \cdot \text{Max}( A_{RC,incl.} ,  A_{RC,semi-incl.} ) = 10^{-5} - 10^{-3}$
	False asymmetry	$\sigma_{A_{false}}$	$< (0.36-0.84) \cdot \sigma_{stat}$

Table 3.6: Contribution to the systematic error of  $A_1$  for the 17  $x$ -bins.

$\langle x \rangle$	$\sigma_{mult}$				$\sigma_{add}$			$\sigma_{syst}$
	$\sigma_{P_b}$	$\sigma_{P_t}$	$\sigma_f$	$\sigma_D$	$\sigma_{ARC}$	$\sigma_{A_{false}}$	$\sigma_{\eta A_2}$	
0.0036	0.00126	0.00088	0.00051	0.00057	0.00046	0.00699	0.00014	0.00722
0.0045	0.00132	0.00092	0.00053	0.00074	0.00040	0.00516	0.00021	0.00550
0.0055	0.00125	0.00088	0.00050	0.00076	0.00039	0.00487	0.00027	0.00520
0.0070	0.00150	0.00105	0.00060	0.00097	0.00040	0.00389	0.00034	0.00447
0.0090	0.00130	0.00091	0.00052	0.00087	0.00042	0.00395	0.00043	0.00442
0.0119	0.00257	0.00180	0.00103	0.00172	0.00047	0.00377	0.00054	0.00535
0.0167	0.00415	0.00291	0.00166	0.00273	0.00055	0.00389	0.00068	0.00719
0.0244	0.00466	0.00326	0.00186	0.00298	0.00069	0.00443	0.00087	0.00810
0.0346	0.00523	0.00366	0.00209	0.00323	0.00087	0.00885	0.00106	0.01166
0.0488	0.00693	0.00485	0.00277	0.00417	0.00109	0.00597	0.00129	0.01162
0.0768	0.00970	0.00679	0.00388	0.00579	0.00144	0.01065	0.00167	0.01752
0.1217	0.01476	0.01033	0.00590	0.00617	0.00178	0.00913	0.00219	0.02211
0.1725	0.01753	0.01227	0.00701	0.00733	0.00192	0.01424	0.00270	0.02782
0.2228	0.01817	0.01272	0.00727	0.00760	0.00187	0.02330	0.00316	0.03405
0.2916	0.02102	0.01471	0.00841	0.00882	0.00159	0.01525	0.00372	0.03249
0.4073	0.02399	0.01679	0.00960	0.01016	0.00063	0.04618	0.00464	0.05664
0.5702	0.03564	0.02495	0.01426	0.01524	0.00142	0.08605	0.01174	0.09935

## 3.7 Results on the longitudinal spin structure of the proton

### 3.7.1 Double spin asymmetry $A_1^p$

The extracted double longitudinal spin asymmetry for a 200 GeV muon beam is presented in Fig. 3.23. The results are shown as a function of  $x$  at the measured  $Q^2$ . A large positive asymmetry is observed at large  $x$  and it dwindles along with  $x$ . To picture this behaviour, let

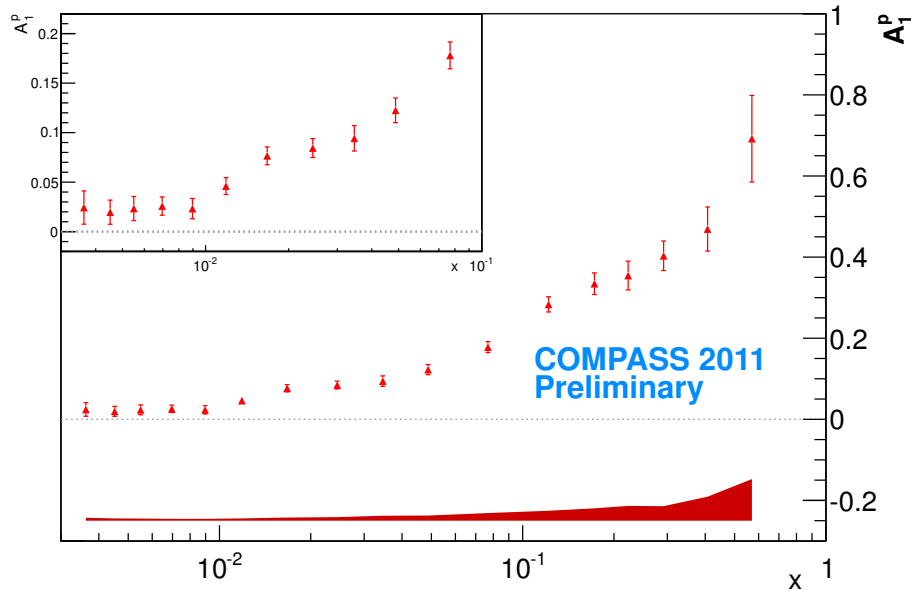


Figure 3.23: The  $A_1^p$  asymmetry as a function of  $x$  obtained from the COMPASS data taken at 200 GeV. The band at the bottom shows the systematic uncertainty. The inset shows a zoom of the low  $x$  region.

us recall the definition of  $A_1 = (\sigma_{1/2} - \sigma_{3/2})/(\sigma_{1/2} + \sigma_{3/2})$  and consider only quarks.

- At large  $x \sim 1$ : the struck quark carries all the momentum of the proton. As the virtual photon interacts only with quarks with an opposite polarisation,  $\sigma_{3/2}$  cancels out and  $A_1(x \rightarrow 1)$  is expected to go towards 1.
- For  $x \sim 1/3$ : the virtual photon interacts with the valence quarks. There are twice more quarks with a polarisation anti-aligned to the polarisation of the virtual photon and thus  $\sigma_{1/2}$  is twice larger than  $\sigma_{3/2}$  so that  $A_1(x \sim 1/3)$  is expected to be around 1/3.
- At small  $x \ll 1$ : the virtual photon probes sea quarks. All quark anti-quark pairs are produced with opposite polarisation, hence one can expect the relative difference between the two cross-sections,  $\sigma_{1/2}$  and  $\sigma_{3/2}$  to decrease.

However, this is only an intuitive representation and measurements are necessary to access and to quantify the parton polarisation especially in the low  $x$  region.

The measurement at 200 GeV is compared to the previous measurements covering the same kinematic domain: one extracted by COMPASS with a polarised muon beam of 160 GeV and one by SMC using a polarised muon beam of 190 GeV in Fig. 3.24. The statistics of the present results at 200 GeV is similar to the one from the previous 160 GeV data. They bring together a factor of about 3 in statistical precision compared to SMC for a comparable beam time. The 200 GeV data have about a factor of 2 larger systematics uncertainties compared to

SMC data. This is mainly due to the beam polarisation and the false asymmetry estimation uncertainties. The beam polarisation relies on a Monte-Carlo simulation, while it was also measured in SMC. The method used by SMC to evaluate the possible false asymmetries is mainly based on MC simulations to study acceptance variations [63]. With this method, SMC reported an astonishing precision  $\sigma_{A_{false}} \leq 0.05 \sigma_{stat}$ , while for COMPASS a conservative value is quoted  $\sigma_{A_{false}} \leq (0.36-0.84) \sigma_{stat}$ .

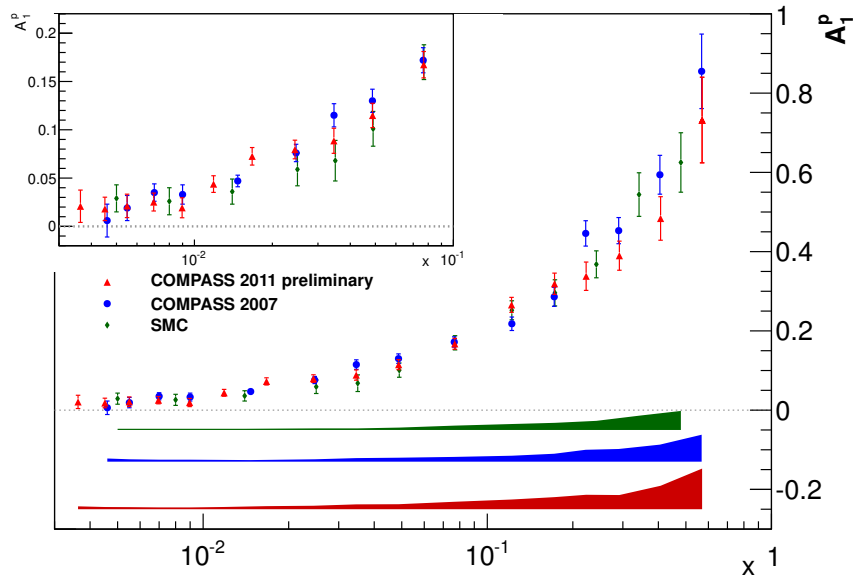


Figure 3.24: Same as 3.23 for COMPASS 200 GeV data (red), 160 GeV data (blue) and SMC 190 GeV data (green).

The results are compared to the world data in Fig. 3.25, where the crucial supply of COMPASS data is visible in the low  $x$  region, which is only covered by CERN experiments. A relatively good agreement is found between all experiments although they are measured at relatively different  $Q^2$ . The asymmetry is found to be very weakly dependent on the scale in the accessed  $Q^2$  range. This is illustrated in Fig. 3.26 where each COMPASS  $x$ -bin is split into three  $Q^2$  bins. The asymmetry is represented as a function of  $Q^2$ . The COMPASS data are fitted to a constant in each bin of  $x$  and no significant deviations were observed. This fact was already observed by SMC [58].

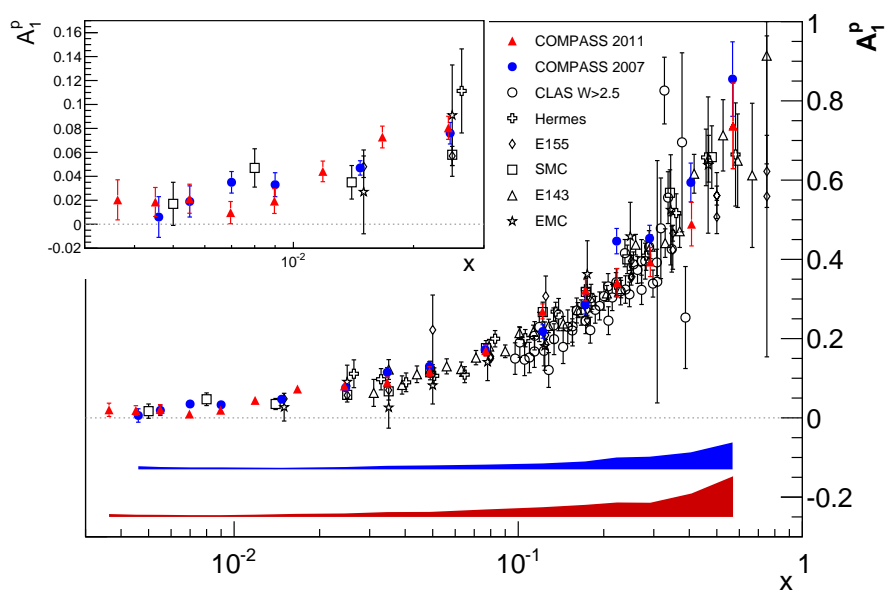


Figure 3.25: Same as 3.23 for world data.

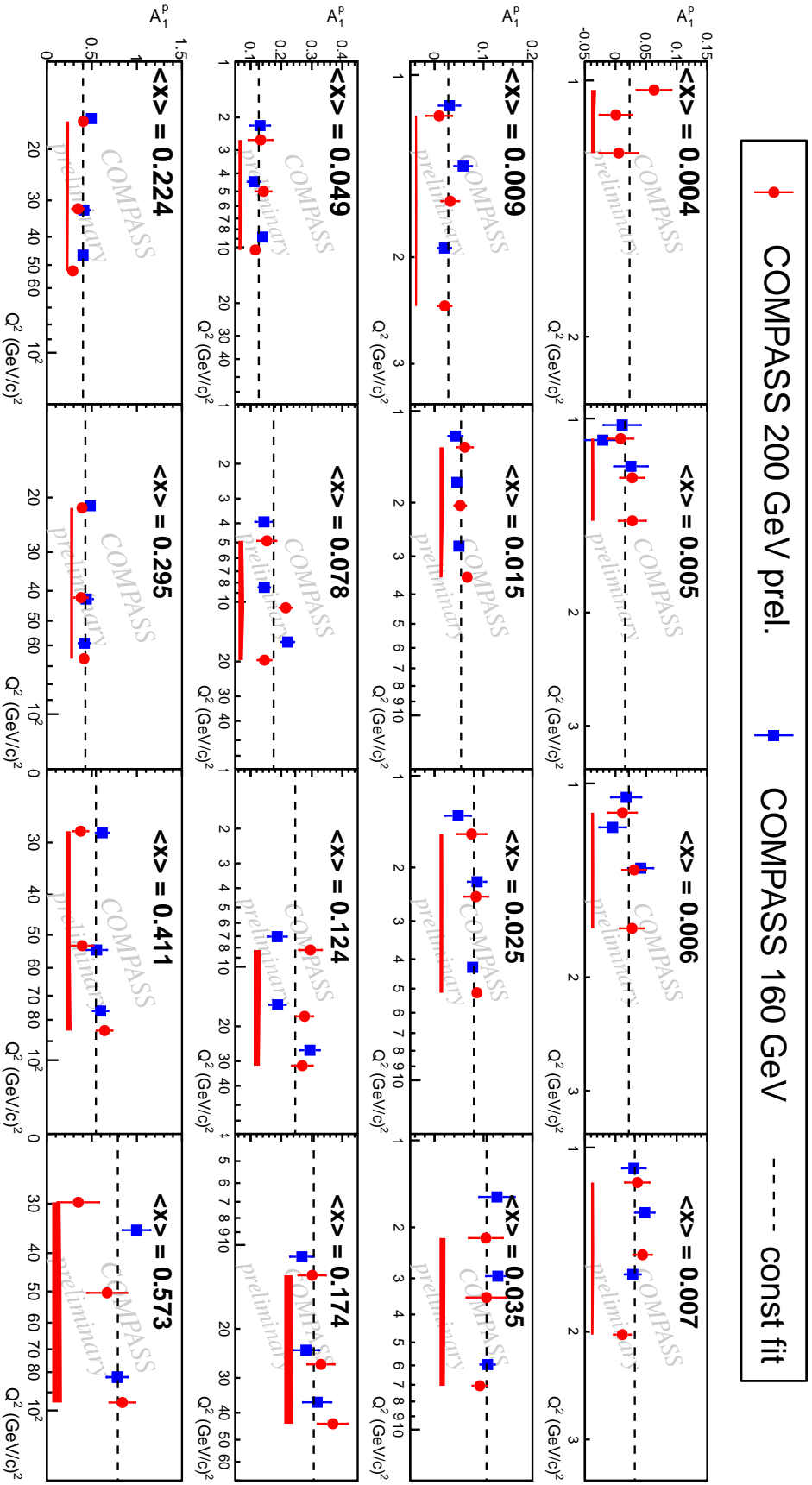


Figure 3.26: The asymmetry  $A_1^p$  as a function of  $Q^2$  at various  $x$  values from the 200 GeV (red) and 160 GeV (blue) COMPASS data. The dashed line indicates the results of the fits to a constant. The band at the bottom indicates the systematic uncertainty for 200 GeV data.

### 3.7.2 The proton spin dependent structure function $g_1^p$

When neglecting the  $A_2$  spin asymmetry, the proton spin dependent structure function  $g_1^p$  is related to  $A_1$  the spin asymmetry according to Eq. (3.30):

$$g_1^p(x, Q^2) = F_1^p(x, Q^2) \cdot A_1^p(x, Q^2) \quad (3.30)$$

where  $F_1^p$  is the spin independent structure function of the proton. It is commonly evaluated through the relation given in Eq. (3.31) which relates the second spin independent structure function of the proton  $F_2^p$  and the ratio of longitudinal to transverse virtual photon absorption cross-section  $R$ .

$$F_1^p(x, Q^2) = \frac{F_2^p(x, Q^2)}{2 \cdot x \cdot (1 + R(x, Q^2))} \quad (3.31)$$

$F_2^p$  is taken from [58] while  $R$  is the one used in the depolarisation factor and taken from [51]. Both structure functions are evaluated at the average value of  $x$  and  $Q^2$  of the data within each bin. The systematic uncertainties on  $A_1$  are propagated with care to  $g_1^p$  to take into account the correlation between  $R$  and  $D$  and with an additional contribution for the uncertainties on the  $F_2^p$  parametrisation. The resulting spin-dependent structure function of the proton is shown in Fig. 3.27. The statistical improvement of the 2011 data taking is clearly visible in the low  $x$  region ( $x < 2 \cdot 10^{-2}$ ) which is only significantly covered by COMPASS and SMC experiments. In Fig. 3.28,  $x \cdot g_1^p$  is plotted to better apprehend the value of the integral of  $g_1^p$  which is directly related to the quark helicity distributions at LO.

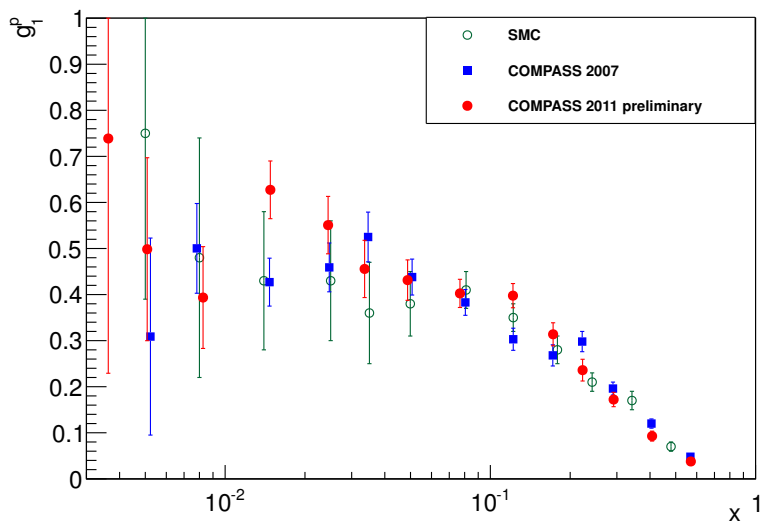


Figure 3.27: The spin-dependent structure function of the proton  $g_1^p$  as a function of  $x$  at the measured  $Q^2 > 1(\text{GeV}/c)^2$  for the 200 GeV COMPASS data (red) and compared to the 160 GeV COMPASS data (blue) and to the 190 GeV SMC data (green).

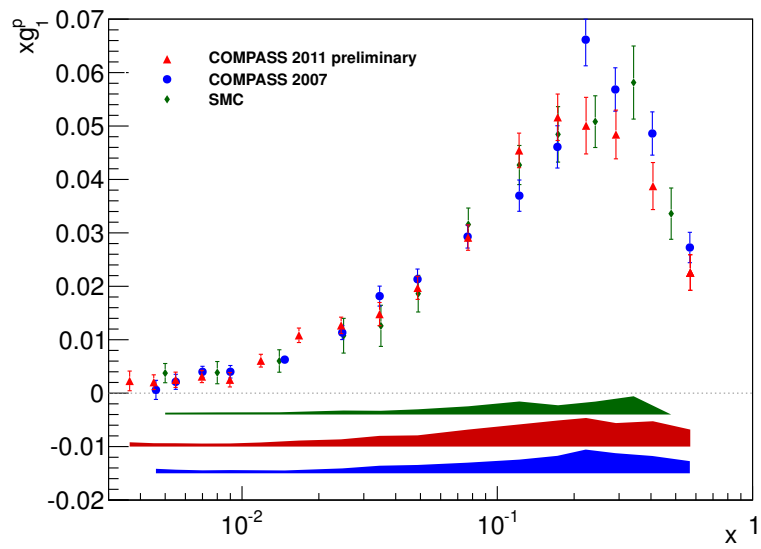


Figure 3.28: Same as 3.27 for  $x \cdot g_1^p$  with the systematics uncertainties of the experiments represented by the coloured bands.

## Chapter 4

# NLO QCD analysis: Extraction of polarised PDFs and Bjorken sum rule

In this chapter, the new  $g_1^p$  data presented in section 3.7 are fitted together with world data on  $g_1^p$ ,  $g_1^d$  and  $g_1^n$  in order to extract the polarised parton distribution functions (PDFs). The aim is to assess the precision with which inclusive data are able to constrain  $\Delta\Sigma$  and  $\Delta G$ . The results of the fits are also used to evolve the COMPASS data alone to a common  $Q^2$  for the purpose of updating the evaluation of the deuteron and proton first moment  $\Gamma_1^p$  and  $\Gamma_1^d$ , as well as the verification of the Bjorken sum rule.

The QCD fit is performed at NLO. It involves explicitly  $\Delta g$  in the expression of  $g_1$ . However, as only inclusive DIS data and the NLO COMPASS open charm muoproduction extraction are included in the fit, it is not possible to separate quarks from antiquarks<sup>1</sup>. The first moment of the quarks per flavour,  $\Delta(u + \bar{u})$ ,  $\Delta(d + \bar{d})$  and  $\Delta(s + \bar{s})$  is obtained using also external constraints coming from axial-vector weak couplings measured in baryon  $\beta$ -decay with the assumption of  $SU(3)_f$  flavour symmetry.

The chapter is organised as follows. Firstly, the fitting method is described with a detailed analysis of the uncertainties. The results for the polarised PDFs are compared to other world extractions which rely on other data and assumptions. The first moment of the proton and the deuteron spin structure functions based on the COMPASS data alone is also evaluated. Finally, the experimental verification of the fundamental Bjorken sum rule is presented.

### 4.1 NLO QCD fits

The extraction of the polarised PDFs is based on a computer program fitting  $g_1^p$ ,  $g_1^d$ ,  $g_1^n$  and the NLO open charm muon production data. It was developed by SMC (program #2 from [64]). Modifications were added to take into account the normalisation uncertainties of the data set and the external inputs (unpolarised PDFs,  $\alpha_s$  evolution code and axial-vector couplings) were updated or modified according to the current knowledge. The fit is performed in the  $\overline{MS}$  factorisation and renormalisation scheme. Unlike most of the fitting programs on the market which solve the Dokshitzer-Gribov-Lipatov-Altarelli-Parisi (DGLAP) equations [65, 66, 67, 68] in the Mellin space, this algorithm computes the  $Q^2$  evolution on a  $(x, Q^2)$  grid<sup>2</sup> which covers the kinematic domain of the experimental data.

---

<sup>1</sup>For instance, semi-inclusive asymmetries  $A_{1,p/d}^{\pi^\pm}$  and  $A_{1,p/d}^{K^\pm}$  as they are sensitive to quark flavour can be used to separate quarks from antiquarks.

<sup>2</sup>The grid spans values of  $Q^2$  from 1 to 100 (GeV/c)<sup>2</sup> and values of  $x$  between 0.001 and 1.

### 4.1.1 Method

#### Data used in the fit

All the data sets considered in the present analysis are given in Table 4.1. They include results expressed as either  $A_1$ ,  $g_1/F_1$  or  $g_1$ . In the case of  $A_1$  data, the inputs are divided by the kinematic factor  $\sqrt{1+\gamma^2} = \sqrt{1+4M^2x^2/Q^2}$  to obtain  $g_1/F_1$ . Then, all  $g_1/F_1$  values (either original or obtained from  $A_1$ ) are converted into  $g_1$  by using the same  $F_1$  parametrisation ( $F_1$  being calculated from  $F_2$  [58] and R [69]). By doing so, instead of using directly the values of  $g_1$ , possible inconsistencies between experiments due to the use of different parametrisations of  $F_1$  are minimised. In appendix A, the difference induced by using either  $g_1$  or converting  $g_1/F_1$  to  $g_1$  is illustrated for CLAS data.

The data binned in both  $x$  and  $Q^2$  are preferred over those integrated over  $Q^2$  when available, to cover the widest kinematic domain and to be as sensitive as possible to the  $Q^2$  scaling violation and thus to the gluon polarisation. Overall, 682 points are available covering the wide kinematic domain shown in Fig. 4.1, two orders of magnitude in  $Q^2$  and two in  $x$ . However, only 679 points are retained in this analysis with three CLAS proton data points being discarded because of their large contribution to the  $\chi^2$  (about 40). The data included in the fit are listed in Table 4.1.

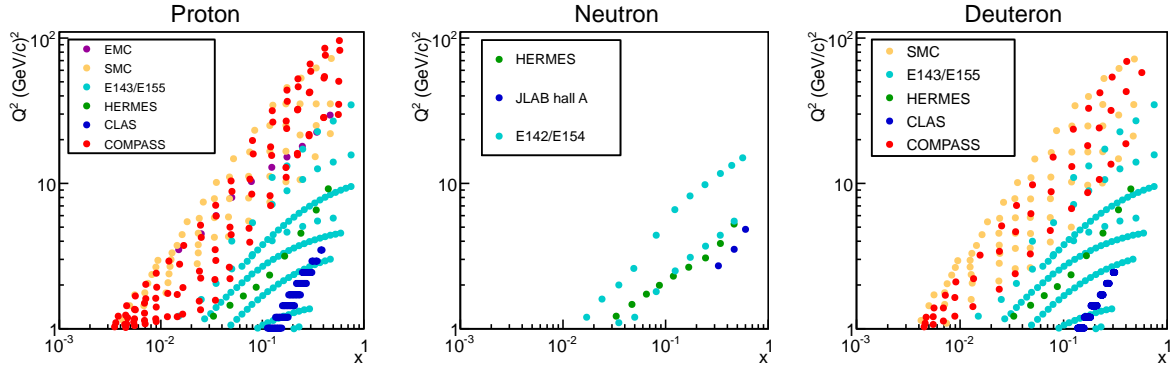


Figure 4.1: The  $x$  and  $Q^2$  kinematic domain covered by  $g_1$  data used in the analysis. Left: proton; Centre: neutron; Right: deuteron.

#### Fitting function

At NLO, the expression for  $g_1$  reads:

$$g_1^{p(n)} = \frac{1}{9} \left( C_S \otimes \Delta q_S + C_{NS} \otimes \left[ \pm \frac{3}{4} \Delta q_3 + \frac{1}{4} \Delta q_8 \right] + C_g \otimes \Delta g \right) \quad (4.1)$$

where the flavour singlet and non singlet combinations of polarised PDFs in  $SU(3)_f$  are used (singlet  $\Delta q_S = \Delta u + \Delta d + \Delta s$ , triplet  $\Delta q_3 = \Delta u - \Delta d$  and octet  $\Delta q_8 = \Delta u + \Delta d - 2\Delta s$ , respectively) and  $\Delta g$  is the gluon spin distribution. All quantities depend on  $x$  and  $Q^2$ . The Wilson coefficients  $C_S$ ,  $C_{NS}$  and  $C_g$  are computed at NLO [70, 71].

Once the distributions are known at a given scale  $Q_0^2$ , the spin-dependent structure functions can be computed at any  $Q^2$  scale by using the DGLAP equations:

$$\frac{d}{d \ln Q^2} \Delta q_{NS} = \frac{\alpha_s(Q^2)}{2\pi} \Delta P_{qq} \otimes \Delta q_{NS} \quad (4.2)$$

$$\frac{d}{d \ln Q^2} \begin{pmatrix} \Delta q_S \\ \Delta g \end{pmatrix} = \frac{\alpha_s(Q^2)}{2\pi} \begin{pmatrix} \Delta P_{qq} & 2n_f \Delta P_{qg} \\ \Delta P_{gq} & \Delta P_{gg} \end{pmatrix} \otimes \begin{pmatrix} \Delta q_S \\ \Delta g \end{pmatrix} \quad (4.3)$$

where  $\alpha_s(Q^2)$  is the strong coupling,  $n_f$  is the number of active quark flavours and  $\Delta P_{ij}$  are the splitting functions computed up to NLO [72, 73]. The following functional forms are chosen at a reference  $Q_0^2$  scale (see section 4.1.2 for more detail):

$$\Delta q_S(x, Q_0^2) = \eta_S \frac{x^{\alpha_S} (1-x)^{\beta_S} (1 + \gamma_S x + \rho_S \sqrt{x})}{\int_0^1 x^{\alpha_S} (1-x)^{\beta_S} (1 + \gamma_S x + \rho_S \sqrt{x}) dx} \quad (4.4)$$

$$\Delta g(x, Q_0^2) = \eta_g \frac{x^{\alpha_g} (1-x)^{\beta_g} (1 + \gamma_g x + \rho_g \sqrt{x})}{\int_0^1 x^{\alpha_g} (1-x)^{\beta_g} (1 + \gamma_g x + \rho_g \sqrt{x}) dx} \quad (4.5)$$

$$\Delta q_3(x, Q_0^2) = \eta_3 \frac{x^{\alpha_3} (1-x)^{\beta_3}}{\int_0^1 x^{\alpha_3} (1-x)^{\beta_3} dx} \quad (4.6)$$

$$\Delta q_8(x, Q_0^2) = \eta_8 \frac{x^{\alpha_8} (1-x)^{\beta_8}}{\int_0^1 x^{\alpha_8} (1-x)^{\beta_8} dx} \quad (4.7)$$

In total, at most 14 parameters are used. Proton and neutron (from deuteron or  $^3\text{He}$ ) target measurements allow to disentangle the isospin singlet, triplet and gluon (from scaling violation) distributions but the octet distribution is under-constrained. Therefore, assuming  $\text{SU}(3)_f$  symmetry, the first moment of the octet distribution,  $\eta_8$ , is fixed to  $3F - D$ , the value of the axial-vector coupling of hyperon obtained from  $\beta$ -decay<sup>1</sup>[74]. The shape of the distribution is expected to be determined from the different scale evolution of the non-singlet distributions.

The  $Q^2$  evolution of the four distributions is performed to reach the scale of each data point and the distributions are combined to compute  $g_1^{fit}$ . The solution for  $\Delta q_S$ ,  $\Delta q_3$ ,  $\Delta q_8$  and  $\Delta g$  distributions is obtained by minimising the  $\chi^2$  function given in Eq. (4.8). More details on the fitting program can be found in [64, 75].

### $\chi^2$ function

The  $\chi^2$  function consists in three terms.

$$\chi^2 = \sum_{n=1}^{N_{exp}} \left[ \underbrace{\sum_{i=1}^{N_n^{data}} \left( \frac{g_1^{fit}(x_i, Q_i^2) - \mathcal{N}_n g_{1,i}^{data}}{\mathcal{N}_n \sigma_i} \right)^2}_{Statistics} + \underbrace{\left( \frac{1 - \mathcal{N}_n}{\delta \mathcal{N}_n} \right)^2}_{Normalisations} \right] + \chi_{positivity}^2 \quad (4.8)$$

The main contribution comes from the difference between the model and the data within the statistical precision. The second contribution is directly related to the normalisation factors of the data sets,  $\mathcal{N}_n$ , which are specific to each experiment and account for global systematic errors within a given measurement. They appear as free parameters in the first term of the  $\chi^2$  function to rescale the measurements and the uncertainties, and are constrained in the second term where large fluctuations with respect to  $\delta \mathcal{N}_n$  are penalised. The uncertainties on the normalisation factors  $\delta \mathcal{N}_n$  are taken from the publications when they are available, or computed from the uncertainties on the beam and target polarisations. The normalisation factors are determined simultaneously with the parameters of the functional forms. The remaining systematic uncertainties locally correlated, mainly evaluated from the dilution factor, the depolarisation factor and the false asymmetry are left out of the  $\chi^2$  function. For a correct treatment of these uncertainties [11, 76] the correlations between the points should be known which is not the case in general. Finally, to constrain the unmeasured large  $x$  region, a positivity condition is applied to the strange and gluon polarisation distributions  $|\Delta(s + \bar{s})(x, Q^2)| < s(x) + \bar{s}(x, Q^2)$  and  $|\Delta g(x, Q^2)| < g(x, Q^2)$ . This condition comes from a probabilistic interpretation of the

<sup>1</sup>The condition is also applied to the triplet distribution,  $\eta_3 = F + D$ .

parton densities at LO. Beyond LO, the positivity condition is strictly valid only for the cross-section relation, however it has been shown [77] that NLO correction to LO positivity bound are small and negligible for  $x \gtrsim 0.01$  compared to polarised PDF uncertainties. Thus, a last term  $\chi_{positivity}^2$ , is added to the  $\chi^2$  function to impose  $|\Delta(s + \bar{s})(x, Q^2)| < s(x) + \bar{s}(x, Q^2)$  and  $|\Delta g(x, Q^2)| < g(x, Q^2)$  for all  $x$  above 0.1. This condition is applied at the lowest considered scale  $Q^2 = 1$  (GeV/c)<sup>2</sup> in this analysis, since positivity once satisfied to a scale is conserved with the evolution to higher scales [78]. The unpolarised NLO PDFs used for the positivity constraints are taken from the MSTW collaboration [11].

Table 4.1: Data sets used in the QCD fit. The  $\chi^2$  contribution and the values obtained for the normalisation factor are given for the three solutions ffN, ffP and ff0 (see text), yielding negative, positive and compatible with zero  $\Delta G$ , respectively. On average the fits have  $\sim 650$  degrees of freedom.

Experiment	Target	Input	Number of points	$\chi^2$			Normalisation		
				ffP	ff0	ffN	ffP	ff0	ffN
EMC [18]	p	$A_1$	10	5.2	4.9	4.8	1.02 $\pm$ 0.07	1.02 $\pm$ 0.07	1.01 $\pm$ 0.07
SMC [58]	p	$A_1$	59	55.0	54.5	55.0	1.02 $\pm$ 0.03	1.01 $\pm$ 0.03	1.00 $\pm$ 0.03
SMC [58]	d	$A_1$	65	58.6	58.7	61.2	1.01 $\pm$ 0.04	1.00 $\pm$ 0.04	1.00 $\pm$ 0.04
COMPASS 04 [27]	d	$g_1$	43	32.6	34.2	37.8	0.99 $\pm$ 0.05	0.97 $\pm$ 0.05	0.95 $\pm$ 0.05
COMPASS 07 [28]	p	$A_1$	44	47.9	46.9	47.1	1.00 $\pm$ 0.02	0.99 $\pm$ 0.02	0.98 $\pm$ 0.02
COMPASS 11 [79]	p	$A_1$	51	41.7	41.8	43.9	1.03 $\pm$ 0.02	1.02 $\pm$ 0.03	1.01 $\pm$ 0.03
E142 [80]	n	$A_1$	8	3.1	2.6	2.5	0.99 $\pm$ 0.07	0.98 $\pm$ 0.07	0.98 $\pm$ 0.07
E143 [81]	d	$g_1/F_1$	82	67.4	67.1	66.6	0.98 $\pm$ 0.04	0.99 $\pm$ 0.04	0.99 $\pm$ 0.04
E143 [81]	p	$g_1/F_1$	82	90.3	90.5	90.0	1.02 $\pm$ 0.02	1.03 $\pm$ 0.02	1.04 $\pm$ 0.02
E154 [82]	n	$A_1$	11	4.4	4.7	5.3	1.03 $\pm$ 0.04	1.03 $\pm$ 0.04	1.04 $\pm$ 0.05
E155 [83]	d	$g_1/F_1$	24	18.6	17.2	17.6	1.01 $\pm$ 0.04	1.00 $\pm$ 0.04	0.99 $\pm$ 0.04
E155 [84]	p	$g_1/F_1$	24	47.4	45.0	43.9	1.12 $\pm$ 0.02	1.11 $\pm$ 0.02	1.11 $\pm$ 0.02
HERMES [85]	d	$A_1$	9	17.7	13.6	10.2	0.98 $\pm$ 0.03	0.99 $\pm$ 0.03	1.00 $\pm$ 0.03
HERMES [85]	p	$A_1$	9	5.3	6.1	6.1	1.03 $\pm$ 0.03	1.03 $\pm$ 0.03	1.04 $\pm$ 0.03
HERMES [86]	n	$A_1$	9	2.2	2.2	2.3	1.00 $\pm$ 0.07	1.00 $\pm$ 0.07	1.00 $\pm$ 0.07
Hall A [87]	n	$g_1/F_1$	3	4.6	4.7	6.4	1.00 $\pm$ 0.05	1.00 $\pm$ 0.05	1.00 $\pm$ 0.05
CLAS [88]	d	$g_1$	86	78.2	78.0	76.6	0.99 $\pm$ 0.09	1.00 $\pm$ 0.09	1.02 $\pm$ 0.08
CLAS [88]	p	$g_1$	59	78.4	81.5	88.5	1.06 $\pm$ 0.02	1.07 $\pm$ 0.02	1.08 $\pm$ 0.01
COMPASS [26]	p and d	$\Delta G/G$	1	9.2	5.7	0.3			

### 4.1.2 Uncertainties affecting the QCD fit

Several sources of uncertainties affecting the QCD fits are studied in this section. Some of them are directly related to the precision of the considered experimental data but others originate from prescriptions used in the choice of functional forms and reference scale, and from theoretical “limitation” due to the unavailability higher order QCD corrections (renormalisation and factorisation scale dependence) or to the neglect of higher twist contributions. In consequence, except for the theoretical uncertainties, a study of the possible systematics that could arise in the QCD fit are investigated.

#### Error propagation from experimental data points

Three approaches are available to propagate the statistical precision of the experimental measurements to the fit results. They are the Lagrange multiplier, the Hessian matrix and the Monte-Carlo sampling [11]. The latter method is used in the present analysis for its simplicity in spanning the uncertainties bands to the various  $Q^2$  nodes of the grid and because its limitations in exporting the uncertainties to any  $Q^2$  do not affect the primary goal of assessing the precision with which polarised inclusive DIS data are able to constrain  $\Delta\Sigma$  and  $\Delta G$ . The method starts by generating replicas of the original data set by repeatedly and randomly varying the original data points according to a Gaussian distribution centred on their mean and with a width equal to their uncertainty. The data replicas are then fitted to produce PDF replicas. Finally, the envelope of the distributions (defined as their sample mean  $\pm$  their RMS) of these PDF replicas evolved at any given  $Q^2$ , provides an estimate of the error bands associated to the uncertainty on the data. Note that these error bands are not necessarily centred on the original PDFs. The uncertainty on any quantity derived from the PDFs, such as  $\Delta\Sigma$  and  $\Delta G$ , can be similarly obtained. An illustration of the method based on 2,000 replicas is given in Fig. 4.2 for  $\Delta G$ .

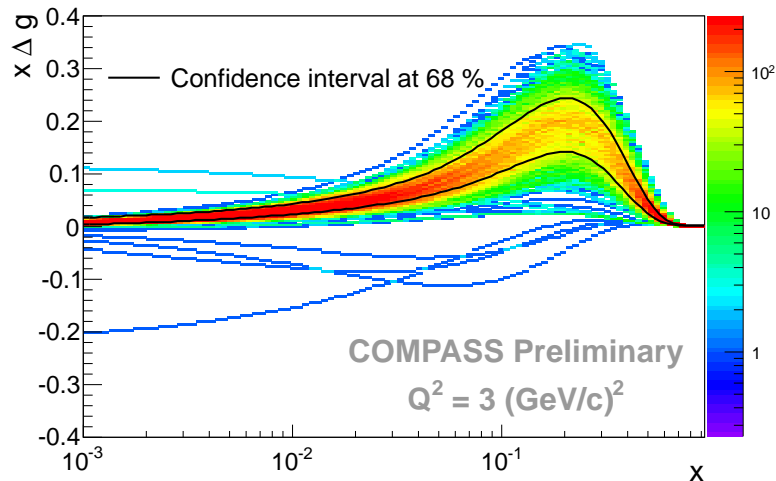


Figure 4.2: Illustration of the randomisation procedure for the polarised gluon distribution. The density of results of the fits to the replicas are shown in colour scale and the black lines indicate a  $1 \sigma$  deviation.

#### Choice of the functional forms

For each distribution, a functional form is assumed at the reference scale  $Q_0^2 = 1 \text{ (GeV/c)}^2$ . The functional forms are composed of at least two factors (Eqs. (4.4) to (4.7)): a factor in  $x^\alpha$

to give the shape at low  $x$  and a factor in  $(1-x)^\beta$  for the behaviour at large  $x$ . For the singlet and gluon cases, a factor in  $(1+\gamma x+\rho\sqrt{x})$  is added to allow the distributions to have a node. Finally, all the distributions are normalised in such a way that the  $\eta$  parameters represent the value of their first moment. The parameters  $\eta_S$  and  $\eta_g$  are determined from the fit while the parameters  $\eta_3$  and  $\eta_8$  are fixed to the values obtained from  $\beta$ -decay measurements (see section 4.1.1). The parameter  $\beta_g$ , which is not very sensitive to the present data, is fixed to 7.5. The relevance of the parameters  $\gamma_s$ ,  $\rho_s$ ,  $\gamma_g$  and  $\rho_g$  has been investigated by fixing all of them to zero and releasing them separately to test all possible combinations.

The three following combinations give a similarly good  $\chi^2$  and span all possibilities of gluon polarisation. They are studied in detail:

$$\text{ffN} : \quad \gamma_S = \rho_S = \gamma_g = \rho_g = 0 \quad \chi^2/ndf = 692/652$$

None of the distributions are allowed to cross zero and the fit converges to a relatively large and negative gluon polarisation:  $\eta_g = -0.67 \pm 0.13$  and  $\eta_S = 0.35 \pm 0.01$ .

$$\text{ffP} : \quad \gamma_s \neq 0 \text{ and } \rho_S = \gamma_g = \rho_g = 0 \quad \chi^2/ndf = 682/651$$

The singlet distribution can cross zero which reduces the value of  $\Delta\Sigma$  and the fit converges to a positive gluon polarisation:  $\eta_g = 0.27 \pm 0.09$  and  $\eta_S = 0.28 \pm 0.02$ .

$$\text{ff0} : \quad \gamma_s \neq 0, \gamma_g \neq 0 \text{ and } \rho_S = \rho_g = 0 \quad \chi^2/ndf = 676/650$$

Both the singlet and the gluon distributions can have a node and the gluon polarisation is found to be compatible with zero:  $\eta_g = -0.13 \pm 0.16$  and  $\eta_S = 0.30 \pm 0.02$

The first moments of the polarised singlet and gluon distributions ( $\Delta\Sigma$  and  $\Delta G$ ) at  $Q^2 = 3$  (GeV/c)<sup>2</sup> are given in Table 4.2 for the three cases. The other combinations, when they converge, give a similarly good  $\chi^2$  and are shown together with the three cases described above in Fig. 4.3. One can see that the solutions for  $\Delta\Sigma$  are rather well constrained by the data and lie between the results given by the cases ffN and ffP. The solutions for  $\Delta G$  lie also between ffN and ffP but the sensitivity of the data to  $\Delta g$  is very poor and the range of possible values is much wider. Only the three cases ffN, ffP and ff0 described above are kept in the rest of the analysis.

Table 4.2: First moment of the distributions for the three functional forms enumerated in the text. The results are given at  $Q^2 = 3$  (GeV/c)<sup>2</sup>.

First moment	ffN	ffP	ff0
$\Delta\Sigma$	0.318	0.272	0.287
$\Delta G$	-0.832	0.451	-0.092

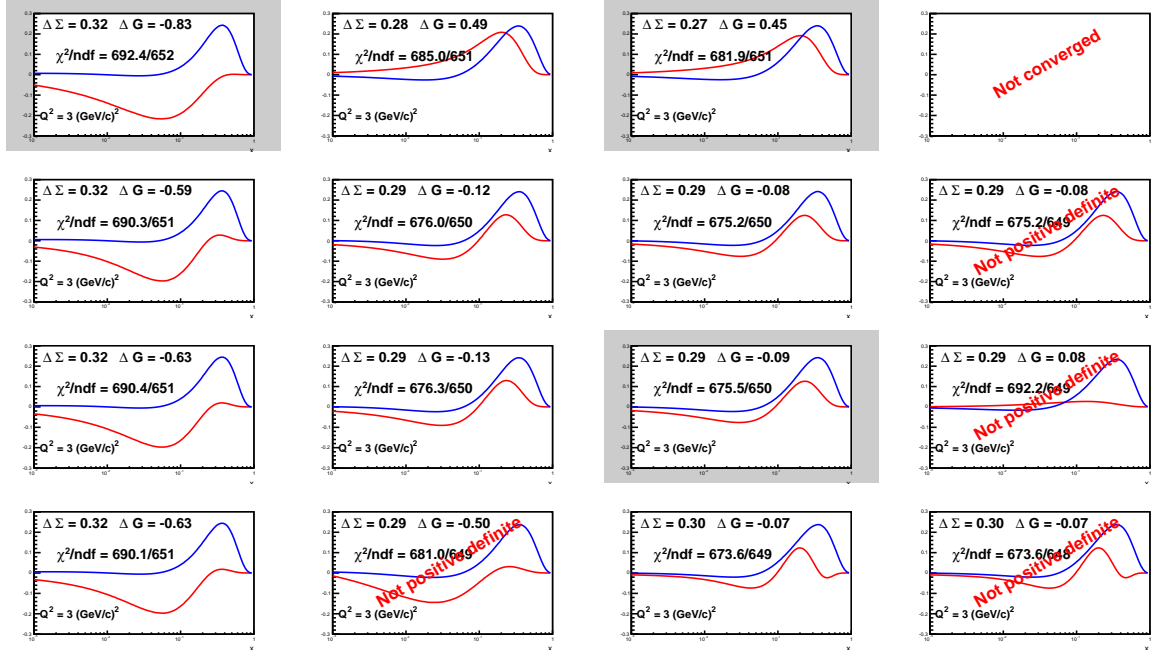


Figure 4.3: Results for  $\Delta q_S(x)$  (blue) and  $\Delta g(x)$  (red) for the sixteen different functional form assumptions as a function of  $x$  with their first moment  $\Delta\Sigma$  and  $\Delta G$ , and the associated value of  $\chi^2$ . In the first column,  $\gamma_S = \rho_S = 0$ . In the second column  $\rho_S$  is free, in the third one  $\gamma_S$  is free and in the last one both  $\gamma_S$  and  $\rho_S$  are free, and similarly for the rows with  $\gamma_g$  and  $\rho_g$ . In five cases, no satisfying minimum were found. The pads coloured in grey correspond to the three functional forms enumerated in the text.

### Choice of the value of $\beta_g$

The  $\beta_g$  parameter, when left free, is not well determined by the data and is kept constant in the fit. Low values of  $\beta_g$  are not favoured because of the positivity condition, while large values would kill the gluon polarisation at high  $x$ . Therefore, the parameter is set to 7.5. A scan of  $\beta_g$  values between 6 and 16 was performed to cover the uncertainty range of the parameter when it is released. The results for the three functional forms are shown in Fig. 4.4. As expected, the first moment of the distributions only evolves weakly with the values of  $\beta_g$ . The highest sensitivity is for the ffN case on both  $\Delta\Sigma$  and  $\Delta G$ ; the lowest one for the fFP case. The effect is quantified in Table 4.3.

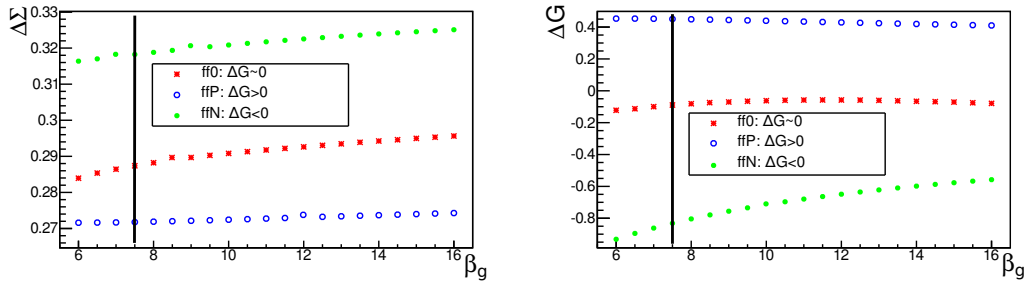


Figure 4.4:  $\Delta\Sigma$  (left) and  $\Delta G$  (right) for various choices of  $\beta_g$ . Results are given at  $Q^2 = 3 \text{ (GeV/c)}^2$ . The vertical line corresponds to  $\beta_g = 7.5$ , value used in the analysis.

Table 4.3: Errors on  $\Delta\Sigma$  and  $\Delta G$  due to imposing a fixed value of  $\beta_g$  (see text).

	ffN	ffP	ff0
$\delta\Delta\Sigma$	0.015	<0.0005	0.015
$\delta\Delta G$	0.03	<0.0005	<0.0005

### Choice of the reference scale

The functional forms were arbitrarily defined at the reference scale  $Q_0^2 = 1$  (GeV/c)<sup>2</sup>. In Figs. 4.5 to 4.7, the results obtained for  $Q_0^2$  values varying between 1 in violet and 63 (GeV/c)<sup>2</sup> in red are shown. Varying the reference  $Q_0^2$ , is equivalent to changing the functional forms at the reference scale. The  $\chi^2$  values in all cases are found to be almost unchanged.

ffN :  $\gamma_S = \rho_S = \gamma_g = \rho_g = 0$  (Figure 4.5)

For  $Q_0^2$  varying from 1 to 18 (GeV/c)<sup>2</sup>,  $\Delta G$  reduces from -0.78 to -0.33. Although the  $\Delta q_S(x)$  distribution shows some sensitivity, the first moment,  $\Delta\Sigma$ , sees a compensation between a gain at large  $x$  and a loss at small  $x$  so that it varies around 0.31.

Above  $Q_0^2 = 20$  (GeV/c)<sup>2</sup>,  $\Delta G$  becomes positive at the reference scale and the evolution to lower scales creates a node in  $\Delta g(x)$  distributions. At  $Q^2 = 3$  (GeV/c)<sup>2</sup>,  $\Delta G$  is stable around -0.03 and  $\Delta\Sigma \sim 0.33$ .

ffP :  $\gamma_S \neq 0$  and  $\rho_S = \gamma_g = \rho_g = 0$  (Figure 4.6)

For  $Q_0^2$  varying from 1 to  $Q_0^2 = 63$  (GeV/c)<sup>2</sup>,  $\Delta G$  varies from 0.45 to 0.03. As in the previous case, the effect on  $\Delta\Sigma$  is small and the first moment of the singlet distribution stays around 0.28.

ff0 :  $\gamma_S \neq 0$ ,  $\gamma_g \neq 0$  and  $\rho_S = \rho_g = 0$  (Figure 4.7)

For  $Q_0^2$  varying between 1 and 63 (GeV/c)<sup>2</sup>,  $\Delta G$  varies between -0.10 to 0.06. The node of this distribution stays around  $x \sim 0.1$ . The value of  $\Delta\Sigma$  varies between 0.265 and 0.285.

Exploring the configuration space of the functional forms along this reference scale dimension allows to fill the gaps between the three discrete solutions ffN, ffP and ff0. The variation of the reference scale shows that  $\Delta G$  at  $Q^2 = 3$  (GeV/c)<sup>2</sup> can take almost any value within [-0.9;0.5] with a slightly favoured region in [-0.1; 0.1]. The favoured region for  $\Delta\Sigma$  is around 0.27 at  $Q^2 = 3$  (GeV/c)<sup>2</sup> but values within [0.265;0.33] can be obtained when varying the reference scale.

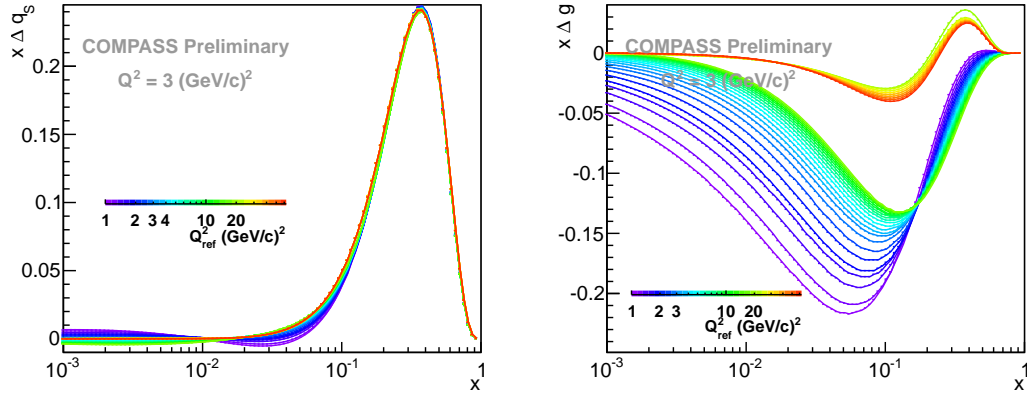


Figure 4.5:  $\Delta q_S(x)$  and  $\Delta g(x)$  at  $3 \text{ (GeV/c)}^2$  for several  $Q_{ref}^2$  when  $\Delta q_S(x) = \eta_S x^{\alpha_S} (1-x)^{\beta_S} / N_S$  and  $\Delta g(x) = \eta_g x^{\alpha_g} (1-x)^{\beta_g} / N_g$  (ffN).  $Q_{ref}^2$  varies from  $1 \text{ (GeV/c)}^2$  in violet to  $63 \text{ (GeV/c)}^2$  in red.

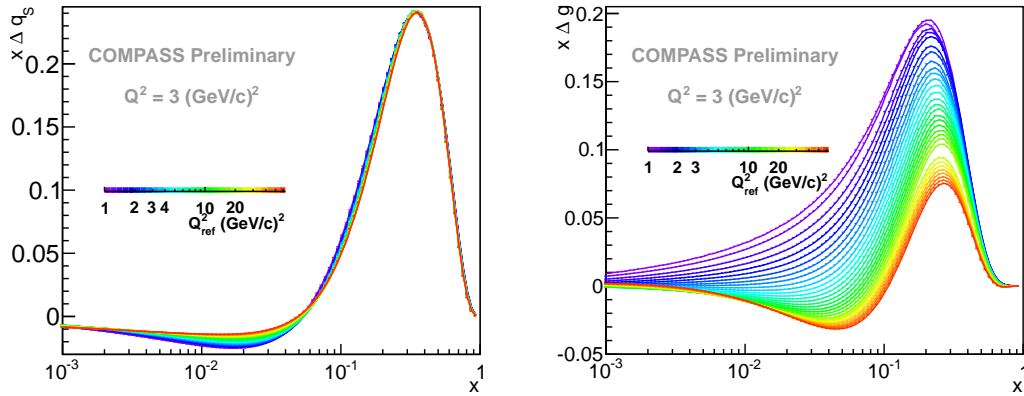


Figure 4.6: Same as Fig. 4.5 for  $\Delta q_S(x) = \eta_S x^{\alpha_S} (1-x)^{\beta_S} (1 + \gamma_S x) / N_S$  and  $\Delta g(x) = \eta_g x^{\alpha_g} (1-x)^{\beta_g} / N_g$  (ffP).

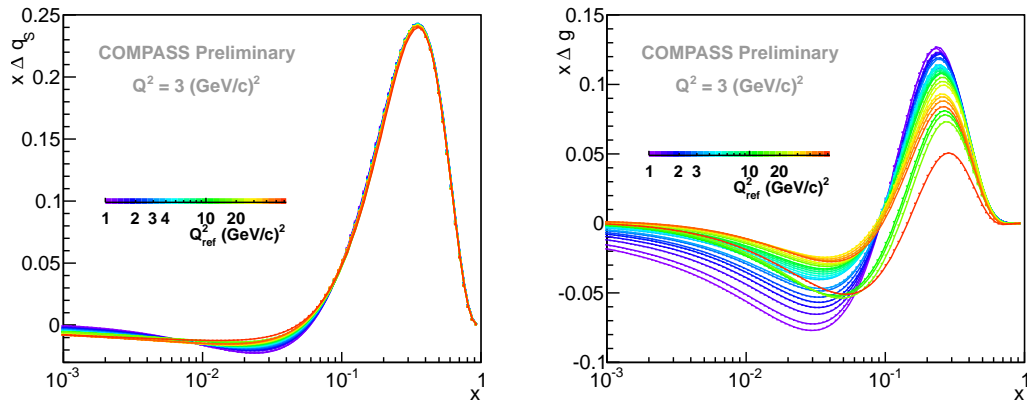


Figure 4.7: Same as Fig. 4.5 for  $\Delta q_S(x) = \eta_S x^{\alpha_S} (1-x)^{\beta_S} (1 + \gamma_S x) / N_S$  and  $\Delta g(x) = \eta_g x^{\alpha_g} (1-x)^{\beta_g} (1 + \gamma_g x) / N_g$  (ff0).

### Error propagation from unpolarised PDF set *via positivity constraint*

As the fits rely on the unpolarised PDFs through the condition of positivity, the sensitivity of the results of the fits on the PDFs was studied. The MSTW collaboration gives  $2n + 1$  sets of

PDFs, where  $n = 20$  is the number of parameters used in their fit. One corresponds to their optimal solution and the other  $2n = 40$  correspond to the solutions with a given increase of  $\chi^2$  when moving along an eigenvector in the parameter space. The 40 sets of PDFs describing a confidence interval of  $1 \sigma$  (probability of 68%) have been used and the resulting uncertainties on the polarised distributions have been computed according to the formulae (7) and (8) given in [89].

The results for the central value (only for completeness) and the uncertainties are given in Table 4.4 for the three solutions of  $\Delta G$ . The error bands associated to this study are shown in black in Fig. 4.8. As expected, an effect can only be seen on  $\Delta g$  and  $\Delta(s + \bar{s})$  for which the positivity constraints are applied. The size of the effect is found to be small compared to the statistical error band for the fits with the ffP and ff0 assumptions and completely negligible for the ffN hypothesis. To explain these facts, one has to remember that the  $\beta_g$  parameter is fixed and the positivity constraint plays only a tiny role in the determination of  $\gamma_s$  (for  $\Delta G \sim 0$ ) and of  $\alpha_g$  (for all cases) since these parameters have a very limited impact in the high  $x$  region. For  $\Delta(s + \bar{s})$ , since the  $\beta$  parameters of  $\Delta q_s$  and  $\Delta q_{\bar{s}}$  are free, an effect representing a fraction of the statistical error band is visible.

Table 4.4: Errors on the first moment of the polarised parton distributions associated to the uncertainties on the unpolarised PDFs  $s(x)$  and  $g(x)$ . The values are given at  $Q^2 = 3 \text{ (GeV}/c)^2$ . Values of first moments are given again only for completeness.

	ffN	ffP	ff0
$\Delta G$	$-0.832^{+0.0004}_{-0.0013}$	$0.451^{+0.0142}_{-0.0193}$	$-0.092^{+0.0279}_{-0.0245}$
$\Delta \Sigma$	$0.318^{+0.0025}_{-0.0023}$	$0.272^{+0.0007}_{-0.0006}$	$0.287^{+0.0004}_{-0.0005}$
$\Delta(u + \bar{u})$	$0.838^{+0.0008}_{-0.0008}$	$0.823^{+0.0002}_{-0.0002}$	$0.828^{+0.0001}_{-0.0002}$
$\Delta(d + \bar{d})$	$-0.431^{+0.0008}_{-0.0008}$	$-0.446^{+0.0003}_{-0.0002}$	$-0.441^{+0.0001}_{-0.0002}$
$\Delta(s + \bar{s})$	$-0.090^{+0.0008}_{-0.0008}$	$-0.105^{+0.0002}_{-0.0002}$	$-0.100^{+0.0001}_{-0.0002}$

### Effect of the uncertainty on $\alpha_s$

The value of the strong coupling at the mass of the  $Z$  boson  $\alpha_s(Z)$  is taken from the MSTW collaboration for consistency with the PDFs which were fitted simultaneously. The impact of the uncertainty on  $\alpha_s$  has been evaluated. As the PDFs used to impose the positivity constraints are correlated with the value of  $\alpha_s$ , the right sets of PDFs were chosen consistently with the value used for  $\alpha_s$ . The error bands on the polarised distributions corresponding to the variation of “ $\alpha_s$ +PDF” within the confidence interval at 68% confidence level are shown in red in Fig. 4.8 and given in Table 4.5. They have been computed according to equations (9) and (10) of [89]. The size of the error is of about half of the statistical uncertainty for all distributions.

Table 4.5: Errors on the first moment of the polarised parton distributions associated to the uncertainties on “ $\alpha_s$ +PDFs”. The values are given at  $Q^2 = 3 \text{ (GeV/c)}^2$ . Values of first moments are given again only for completeness.

	ffN	ffP	ff0
$\Delta G$	$-0.832^{+0.0155}_{-0.0157}$	$0.451^{+0.0449}_{-0.0332}$	$-0.092^{+0.0997}_{-0.0857}$
$\Delta \Sigma$	$0.318^{+0.0054}_{-0.0054}$	$0.272^{+0.0050}_{-0.0062}$	$0.287^{+0.0076}_{-0.0088}$
$\Delta(u + \bar{u})$	$0.838^{+0.0017}_{-0.0017}$	$0.823^{+0.0016}_{-0.0019}$	$0.828^{+0.0024}_{-0.0028}$
$\Delta(d + \bar{d})$	$-0.431^{+0.0019}_{-0.0019}$	$-0.446^{+0.0018}_{-0.0021}$	$-0.441^{+0.0026}_{-0.0030}$
$\Delta(s + \bar{s})$	$-0.090^{+0.0018}_{-0.0018}$	$-0.105^{+0.0017}_{-0.0021}$	$-0.100^{+0.0026}_{-0.0030}$

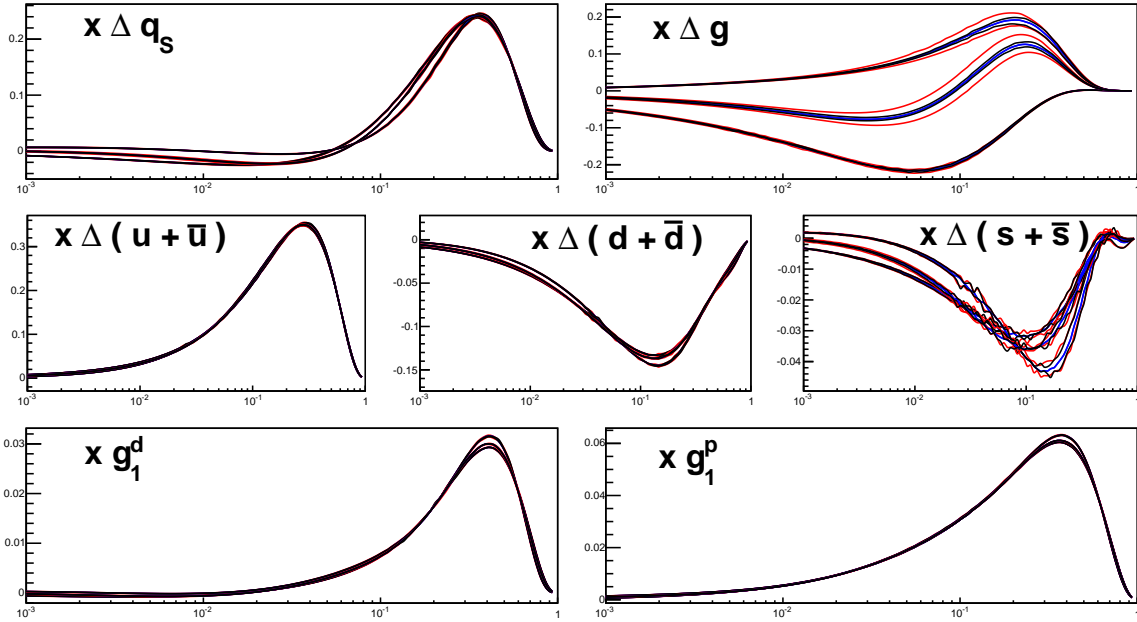


Figure 4.8: Distributions of the polarised PDFs as a function of  $x$  in blue with the error bands propagated from the uncertainties on the unpolarised PDFs in black and from “ $\alpha_s$ +PDFs” in red. Results are at  $3 \text{ (GeV/c)}^2$ .

### Normalisation uncertainties

The normalisation values obtained from the fits listed in Table 4.1 are compatible with 1.0 except for E155 (1.11) and CLAS (1.07) proton data. For E155, it was expected since the authors suggested already a normalisation of  $1.08 \pm 0.03 \pm 0.07$ . For CLAS proton data, the 6% normalisation was found to be unexpectedly large given the uncertainty quoted (2%).

### $SU(3)_f$ symmetry breaking effect on the non-singlet distribution normalisations

The fits were performed assuming  $SU(3)_f$  symmetry to fix the first moments  $\eta_3$  and  $\eta_8$  to  $F + D$  and  $3F - D$  respectively (see section 4.1.2). In this section the constants  $F$  and  $D$  are used only to initialise the  $\eta_3$  and  $\eta_8$  parameters which are released under constraints. Additional

terms defined in Eq. (4.9) are added to the  $\chi^2$  function (Eq. (4.8))

$$\chi_{add.}^2 = \left( \frac{\epsilon_{SU(2)_f}}{\delta\epsilon_{SU(2)_f}} \right)^2 + \left( \frac{\epsilon_{SU(3)_f}}{\delta\epsilon_{SU(3)_f}} \right)^2 \quad (4.9)$$

where:

$$\epsilon_{SU(2)_f} = \frac{\eta_3 - (F + D)}{F + D} \quad (4.10)$$

and

$$\epsilon_{SU(3)_f} = \frac{\eta_8 - (3F - D)}{3F - D} \quad (4.11)$$

represent the relative deviations from  $SU(2)_f$  and  $SU(3)_f$  respectively. The relative uncertainties on  $F + D$  and  $3F - D$  are  $\delta\epsilon_{SU(2)_f}$  and  $\delta\epsilon_{SU(3)_f}$ . The results of the fits give  $\epsilon_{SU(2)_f} = 0.08\%$  and  $\epsilon_{SU(3)_f} = 0.08\%$ . The values are similarly small and do not imply deviations from the  $SU(2)_f$  and  $SU(3)_f$  symmetry. Relaxing  $SU(2)_f$  and  $SU(3)_f$  does not change the value of the other parameters ( $\alpha_3, \alpha_8, \alpha_S, \dots$ ) by more than 0.1% in the most extreme case and the correlation between the  $\epsilon$  parameters and the others is smaller than 10%. For those reasons, the possible effects of symmetry breaking are neglected.

However, it should be noted that the possible actual symmetry breaking may not be reflected by the value of  $\delta\epsilon_{SU(2)_f}$  and  $\delta\epsilon_{SU(3)_f}$  [90, 76].

### 4.1.3 Results and conclusions from the QCD fits of world data

#### On the polarised parton distributions:

All the results of the fits presented in section 4.1.2 are summarised in three parametrisations (Fig. 4.9) that represent the three possible hypotheses of gluon polarisation (ffN:  $\Delta G < 0$ , ffP:  $\Delta G > 0$  and ff0:  $\Delta G \sim 0$ ). The dark coloured bands represent the statistical uncertainty, *i.e.* the results of the error propagation of the statistical uncertainty of the input data. They are evaluated via the randomisation procedure. The lightest bands correspond to the combined statistical and all systematics uncertainties discussed previously. The major contribution of the errors on the fit results comes from the choice of the functional forms that cannot be discriminated by the present data. This is mainly due to the weak sensitivity of the data to  $\Delta g(x)$  because of the limited kinematic coverage in  $x$  and  $Q^2$  in current measurements.

The comparison of the resulting  $g_1$  parametrisations to the world data are shown in Fig. 4.10. The ff0 functional forms defined at  $Q_0^2 = 1$  (GeV/c)<sup>2</sup> were chosen for the central value of  $g_1$  as they give one of the best  $\chi^2$  if ever it can really be discriminated. The ffN and ffP functional forms were used to create the uncertainty bands. As expected from the low values of  $\chi_r^2 \sim 1.05$ , a good description of the world data is given by the fits.

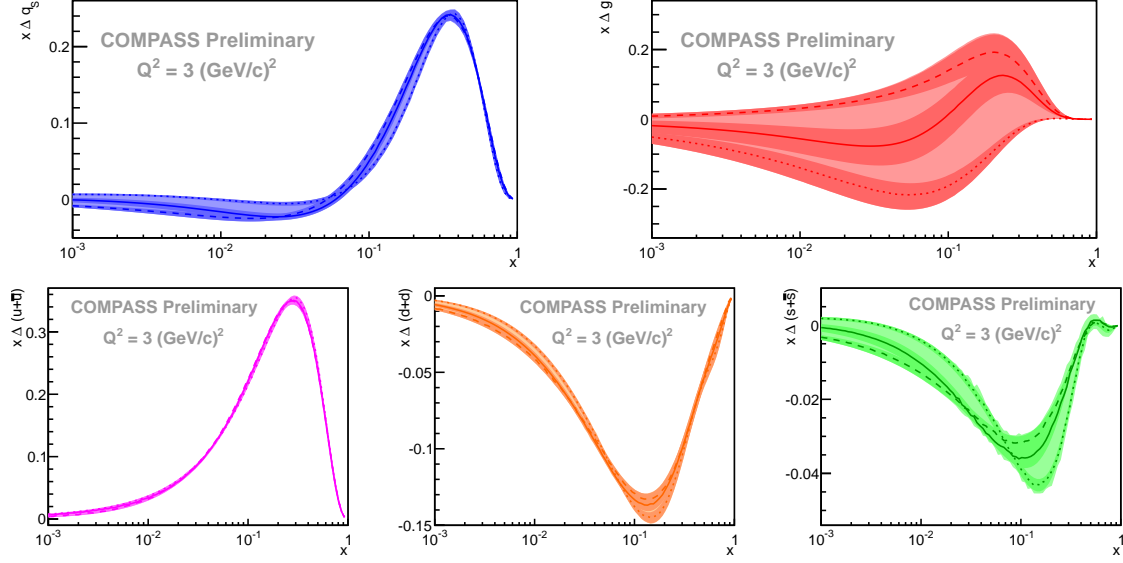


Figure 4.9: Results from the NLO QCD fits of  $g_1$  world data at  $Q^2=3$  (GeV/c) $^2$ . Top left: Quark singlet distribution  $x\Delta q_S(x)$ . Top right : Gluon spin distribution  $x\Delta g(x)$ . Bottom left to right:  $x(\Delta q + \Delta \bar{q})(x)$  for u, d and s flavour. The three solutions (dashed, solid and dotted lines) correspond to the three hypotheses of functional forms (ffP, ff0, ffN) (see text and appendix B for the value of the parameters).

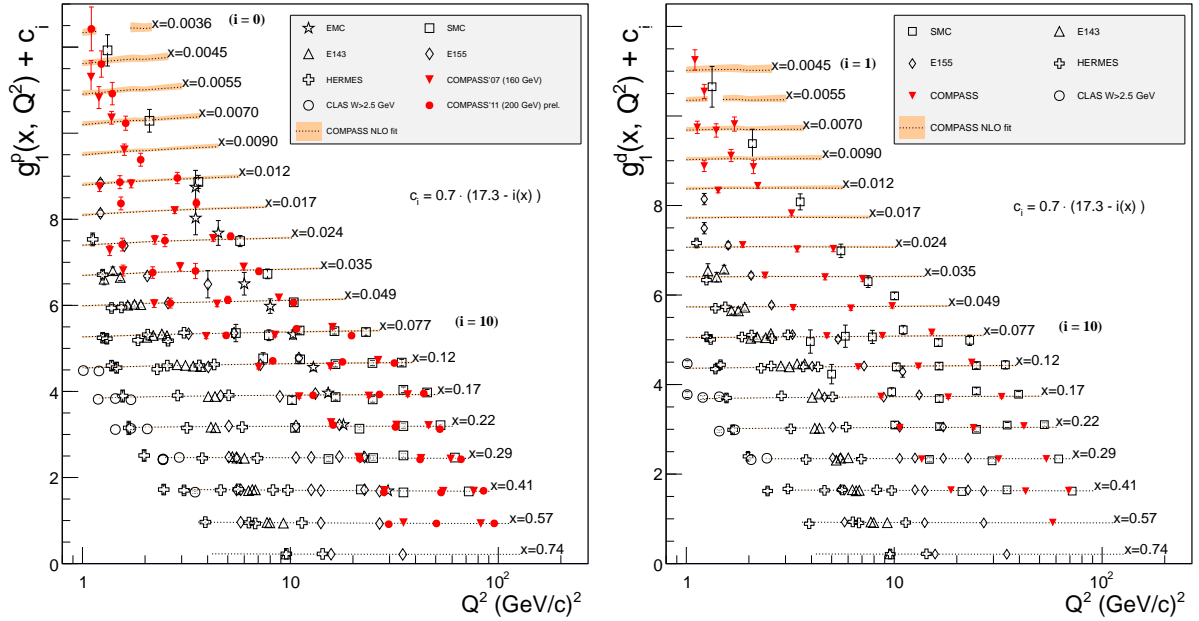


Figure 4.10: Results for the COMPASS NLO QCD fit to  $g_1$  world data, proton (left) and deuteron (right). The curves are given *vs.*  $Q^2$  at several values of  $x$  and are compared to the data. The orange band represents the envelope of the three parametrisations given in appendix B (Table B.1) including statistical and systematic errors. The dotted lines corresponds to the ff0 functional form defined at  $Q_{ref}^2 = 1$  (GeV/c) $^2$ .

### On the first moment of the polarised parton distributions:

The confidence domains for the parameters  $\eta_S$  and  $\eta_g$  that correspond to the first moments  $\Delta\Sigma$  and  $\Delta G$  at the input scale are shown in Fig. 4.11 at  $Q^2 = 1$  (GeV/c) $^2$  for the functional forms ffN, ffP and ff0. The domains are derived from a study using the fitting error analysis

method MINOS, which performs a minimisation of the  $\chi^2$  for fixed values of  $\eta_S$  and  $\eta_g$ . A clear correlation is visible between  $\Delta G$  and  $\Delta\Sigma$ . Considering the three  $\Delta G$  solutions together,  $\Delta\Sigma$  is only constrained to  $[0.264, 0.356]$ . If the negative  $\Delta G$  solution could be removed (slightly larger  $\chi^2$ ),  $\Delta\Sigma$  would be constrained to  $[0.264, 0.318]$ . This is also illustrated in Fig. 4.12, which

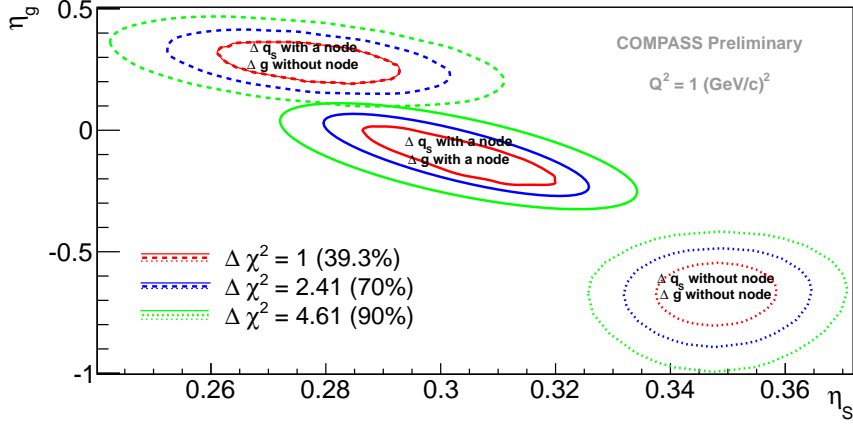


Figure 4.11: Domains of 39%, 70% and 90% confidence level for  $\eta_S$  (*i.e.*  $\Delta\Sigma$ ) and  $\eta_g$  (*i.e.*  $\Delta G$ ) for the three assumed sets of functional forms. The domains are shown at  $Q^2 = Q_0^2 = 1$  (GeV/c) $^2$ .

shows the results of  $\Delta\Sigma$  and  $\Delta G$  with the  $\chi^2$  probability for all of the almost equally likely functional forms studied in section 4.1.2. They are given at the average scale of the COMPASS data  $\langle Q^2 \rangle = 3$  (GeV/c) $^2$ . For the functional forms defined at a reference scale different from  $\langle Q^2 \rangle$ , a numerical integration of the results of the fits is performed down to the lowest  $x$  point of the grid:  $x = 0.001$ . The rest of the integral is estimated by an extrapolation of the form  $x^\alpha$ . The resulting values of  $\Delta\Sigma$  lies within  $[0.256, 0.335]$  and  $\Delta G$  value are within  $[-1, 0.5]$ . For completeness, the range of values for  $\Delta\Sigma$  is given at  $Q^2 = 1, 3$  and  $10$  (GeV/c) $^2$  in Table 4.6.

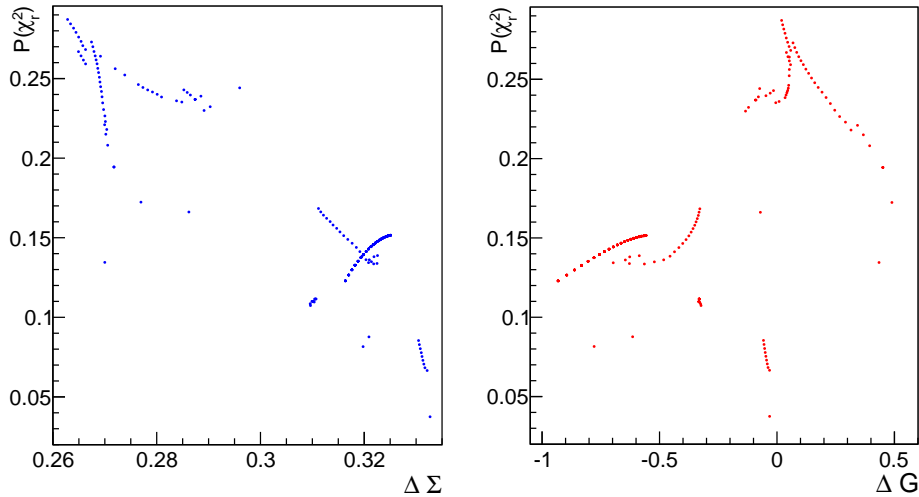


Figure 4.12:  $\chi^2$  probability for the various fits. Values are plotted *vs.*  $\Delta\Sigma$  (left) and  $\Delta G$  (right). The first moments are given at  $Q^2 = 3$  (GeV/c) $^2$ . Fits with  $\Delta G \sim 0$  and  $\Delta G > 0$  and smaller values of  $\Delta\Sigma$  have a slightly higher  $\chi^2$  probability than the ones for  $\Delta G < 0$  and greater values of  $\Delta\Sigma$ , although those first moments cannot be disregarded.

Table 4.6: Range of solution for  $\Delta\Sigma$  from the QCD fits of  $g_1$  at  $Q^2 = 1, 3$  and  $10$   $(\text{GeV}/c)^2$ . No  $Q^2$  evolution is seen.

$Q^2$ $((\text{GeV}/c)^2)$	$\Delta\Sigma$
1	[0.264, 0.356]
3	[0.256, 0.335]
10	[0.258, 0.299]

### On the first moment of the spin structure functions $g_1^p$ and $g_1^d$ :

In order to compute the first moments  $\Gamma_1^p$  and  $\Gamma_1^d$ , the COMPASS  $g_1^p$  and  $g_1^d$  data are evolved (using the NLO fit) to the average scale of the measurements  $\langle Q^2 \rangle = 3$   $(\text{GeV}/c)^2$  according to the formula:

$$g_1(x_{meas.}, \langle Q^2 \rangle) = g_1^{meas.}(x_{meas.}, Q_{meas.}^2) - g_1^{fit}(x_{meas.}, Q_{meas.}^2) + g_1^{fit}(x_{meas.}, \langle Q^2 \rangle) \quad (4.12)$$

The results are shown in Fig. 4.13 and compared to the results of the NLO QCD fit at the same scale. As expected the scaling violation of  $g_1$  increases for low values of  $x$  and “large” values of  $Q^2$  and the behaviour of  $g_1$  depends more strongly on the shape of  $\Delta g$  as it can be seen for  $x < 0.01$ . A discrimination could be possible in this region only with an improvement of statistical precision by a factor of four in the proton or deuteron data.

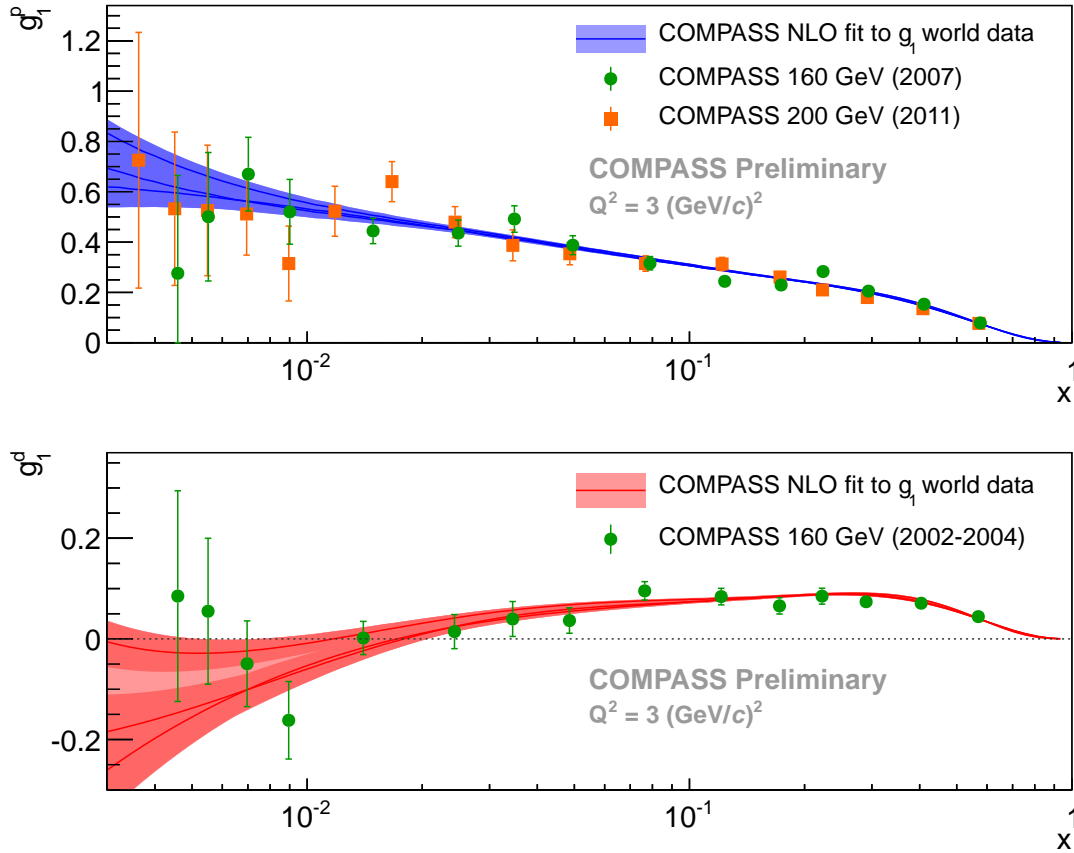


Figure 4.13: Results for the COMPASS NLO QCD fit to  $g_1$  world data at  $3$   $(\text{GeV}/c)^2$  compared to COMPASS proton (top) and deuteron (bottom) data. As expected, for  $x < 0.01$ , the  $g_1$  behaviours start to show a sensitivity to the gluon polarisation.

The evaluation of the first moments  $\Gamma_1^p$  and  $\Gamma_1^d$  of the spin structure functions is based on two contributions: one from the integral in the measured range and one from the extrapolations to  $x = 0$  and to  $x = 1$ . Within the measured range, the truncated first moment is evaluated according to:

$$\int_{x_{min}}^{x_{max}} g_1(x, \langle Q^2 \rangle) dx \approx \sum_{i=1}^{n-1} (x_{i+1} - x_i) \cdot g_1^{data}(x_{c,i}, \langle Q^2 \rangle) \quad (4.13)$$

where  $x_i$  are the edges of the bins and  $x_{c,i}$  the centre of the  $i^{th}$  bin. In the case of the proton, the data points taken at the two beam energies 160 and 200 GeV are merged once evolved to the same scale. For the unmeasured region, a numerical integration of the fits is performed within the grid<sup>1</sup> (4.14) and a linear extrapolation based on the fits complete the grid down to  $x = 0$ .

$$\int_{\text{grid}} g_1^{fit}(x, \langle Q^2 \rangle) dx = \sum_{x \in \text{grid}} 0.5 \cdot (x_{i+1} - x_i) \cdot (g_1^{fit}(x_i, \langle Q^2 \rangle) + g_1^{fit}(x_{i+1}, \langle Q^2 \rangle)) \quad (4.14)$$

The values of the different contributions to the first moment of the proton and the deuteron spin structure functions are given in Table 4.7 for the ff0 ( $\Delta G \sim 0$ ) hypothesis. The same

Table 4.7: Contribution to the first moment of the proton and deuteron spin structure functions  $\Gamma_1^p$  and  $\Gamma_1^d$  at  $Q^2 = 3$  (GeV/c)<sup>2</sup> (ff0 hypothesis).

x range	$\Gamma_1^p$	x range	$\Gamma_1^d$
0.0000-0.0025	0.0025	0.000-0.004	-0.0007
0.0025-0.7000	$0.1316 \pm 0.0028$	0.004-0.700	$0.0457 \pm 0.0027$
0.7000-1.0000	0.0031	0.700-1.000	0.0013

evaluation is also performed for the two other  $\Delta G$  hypotheses. The results of the truncated first moment as a function of the lower bound of the integral is shown in Fig. 4.14 for the three  $\Delta G$  hypotheses.

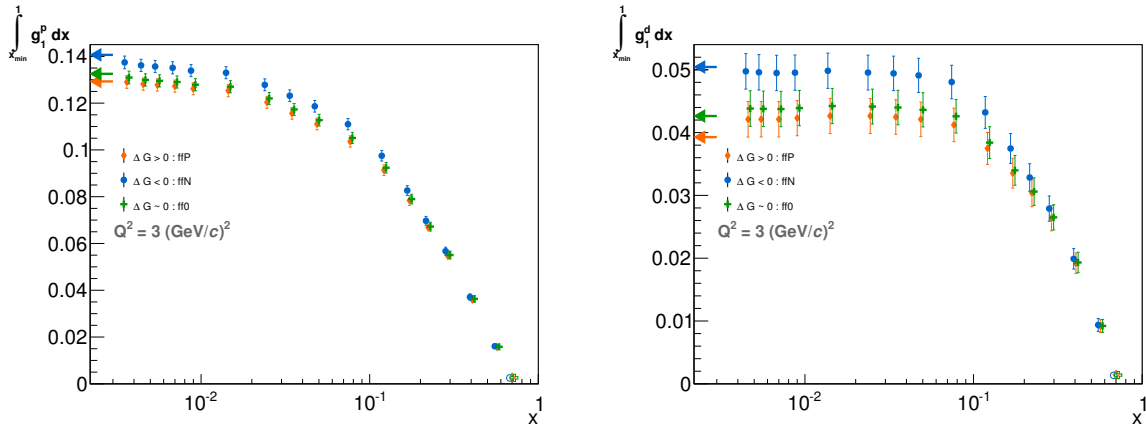


Figure 4.14: Truncated first moment of  $g_1^p$  (left) and  $g_1^d$  (right) at  $Q^2 = 3$  (GeV/c)<sup>2</sup> as a function of the lower bound of the integral. The arrows show the estimated first moments using the extrapolation from the fits.

The spread of results for the different  $\Delta G$  solutions are used as systematics associated to the evolution. The statistical and the systematic uncertainties of the data points are propagated

<sup>1</sup>The grid covers the  $x$  range between 0.001 and 0.0025, and between 0.1 and 1

to the evaluation of the first moment. Combining the proton and the deuteron data after a correction for the D-state probability, one can also evaluate the first moment  $\Gamma_1^n$  of the neutron spin structure function by the relation:

$$\Gamma_1^n = 2 \cdot \frac{\Gamma_1^d}{1 - \frac{3}{2} \cdot \omega_D} - \Gamma_1^p \quad (4.15)$$

The first moment of the spin structure functions with the statistical and systematical uncertainties are given in Table 4.8 for three values of  $Q^2$ .

Table 4.8: First moment of the proton (top), deuteron corrected for the D-state (middle) and neutron (bottom) at 1,3 and 10  $(\text{GeV}/c)^2$  from COMPASS data. The first uncertainty is statistical, the second comes from the systematic uncertainties on the data and the last one from the evolution from the measured scale to the  $Q^2$  of evaluation.

$Q^2$ $(\text{GeV}/c)^2$	$\Gamma_1^p$
1	$0.1313 \pm 0.0027 _{stat.} \pm 0.0081 _{syst.} \pm 0.0036 _{evol.}$
3	$0.1372 \pm 0.0027 _{stat.} \pm 0.0084 _{syst.} \pm 0.0031 _{evol.}$
10	$0.1396 \pm 0.0027 _{stat.} \pm 0.0086 _{syst.} \pm 0.0022 _{evol.}$

$Q^2$ $(\text{GeV}/c)^2$	$\Gamma_1^d$
1	$0.0454 \pm 0.0028 _{stat.} \pm 0.0081 _{syst.} \pm 0.0036 _{evol.}$
3	$0.0463 \pm 0.0028 _{stat.} \pm 0.0035 _{syst.} \pm 0.0031 _{evol.}$
10	$0.0464 \pm 0.0028 _{stat.} \pm 0.0035 _{syst.} \pm 0.0022 _{evol.}$

$Q^2$ $(\text{GeV}/c)^2$	$\Gamma_1^n$
1	$-0.0405 \pm 0.0063 _{stat.} \pm 0.0108 _{syst.} \pm 0.0036 _{evol.}$
3	$-0.0445 \pm 0.0063 _{stat.} \pm 0.0112 _{syst.} \pm 0.0031 _{evol.}$
10	$-0.0469 \pm 0.0063 _{stat.} \pm 0.0114 _{syst.} \pm 0.0022 _{evol.}$

#### 4.1.4 Comparison of $\Delta g$ from the NLO QCD fits to direct measurements

The three NLO fit results on  $\Delta g$  are compared to direct measurements of  $\Delta g$  in Fig. 4.15. These measurements come from the analysis of the photon-gluon-fusion channel, which is tagged by high- $p_T$  hadron (photo)productions [91, 92, 93, 94] or open charm muoproduction [26], interpretable at LO and NLO, respectively. They are all in fair agreement with the fit results (which do not include these data points but the COMPASS open charm measurement).

Let us take a closer look to the latest COMPASS LO  $\Delta g$  extraction [92], which is the most precise LO extraction in the world that gives  $\langle \Delta g/g \rangle = 0.113 \pm 0.038 \pm 0.035$  positive at the  $3\sigma_{stat}$  for  $\langle x \rangle = 0.10$ . Compared to the ffP, ff0 and ffN NLO solutions separately, one obtains a  $\chi^2$  of 1.0, 5.4 and 42.7 respectively. Looking to these values and keeping in mind that the results are at different QCD order of correction and that only the statistical uncertainty of the direct measurement enters the chi-square calculation, one can conclude that the latest COMPASS LO extraction favours the ffP and ff0 NLO solutions.

As the only direct NLO extraction of  $\Delta G$  (COMPASS open charm muoproduction result) is included in the fit, we only emphasise that it favours the ffN solution, see Table 4.1.

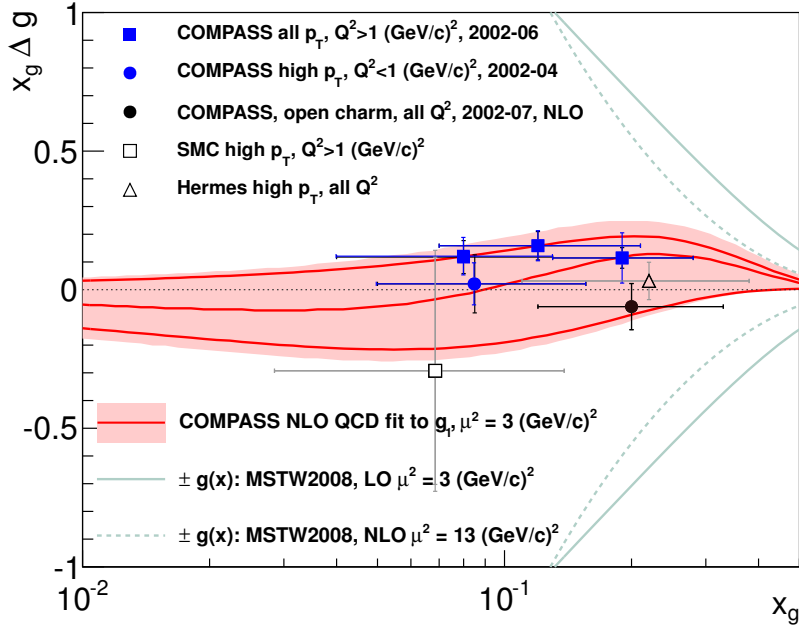


Figure 4.15: The three solutions for  $\Delta g$  from the NLO fit to  $g_1$  world data compared to direct measurements of  $\Delta g$  via photon-gluon-fusion process. LO extraction from high  $p_T$  [91, 92, 93, 94] (blue circle, blue squares, open triangle, open square) and NLO extraction from open charm muoproduction [26] (black circle).

#### 4.1.5 Comparison of the present NLO QCD fits to other global QCD analysis

The results of the distributions of  $\Delta(u + \bar{u})$ ,  $\Delta(d + \bar{d})$ ,  $\Delta(s + \bar{s})$  and  $\Delta g$  are also compared in Fig. 4.16 to other NLO QCD fit extractions from the LSS, DSSV and NNPDFpol collaborations [95, 96, 97] with their error bars when they are available.

For  $\Delta(u + \bar{u})$  and  $\Delta(d + \bar{d})$ , a relatively good agreement is found within the measured range, although the NNPDFpol1.1 distribution for  $\Delta(d + \bar{d})$  deviates slightly from the general trend between  $0.04 \leq x \leq 0.1$ . A deviation from the general trend is also observed for the results of the present analysis in the unmeasured high- $x$  region. Unlike the other results, no positivity conditions were applied to the  $\Delta(u + \bar{u})$  and  $\Delta(d + \bar{d})$  distributions. This neglect is being studied and will be discussed as a perspective in the end of the section.

Large differences are also visible over the whole  $x$  range for  $\Delta(s + \bar{s})$  distribution. The present analysis agrees with the result of NNPDFpol and gives a negative distribution for the strange quark polarisations of the nucleon. This distribution is actually not well constrained by the present data. In the case of only inclusive DIS data, the distribution of  $\Delta(s + \bar{s})$  is determined mainly by the  $SU(3)_f$  flavour symmetry, which fixes the first moment to a negative value, and marginally by the evolution. In contrast, in the fits of the LSS and DSSV collaborations, semi-inclusive DIS data are included. Those data are sensitive to the quark flavours but are also subjected to the knowledge of fragmentation functions. The discrepancy for  $\Delta s$  is known and is part of the current issues in spin hadronic physics to be solved.

Results for  $\Delta g$  from the various fits are quite spread. The two solutions, ffP and ff0, which have the best  $\chi^2$  are the closest to the other analyses. In particular they are compatible with the latest results of the DSSV and NNPDFpol collaborations, which include the RHIC spin data in their fit and lead to a significant positive truncated  $\Delta G$  value for  $x$  within  $[0.05, 0.2]$  (see Table 4.9 for a rough comparison).

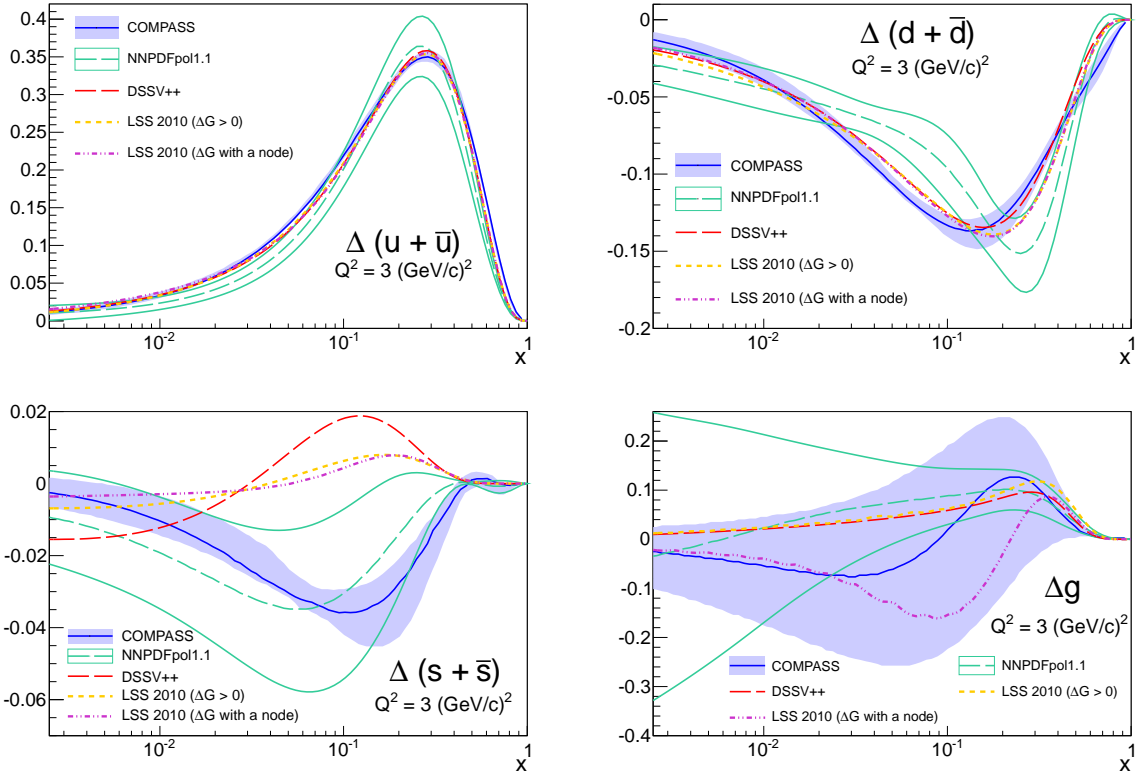


Figure 4.16: Distributions of  $\Delta(u + \bar{u})$  (top left),  $\Delta(d + \bar{d})$  (top right),  $\Delta(s + \bar{s})$  (bottom left) and  $\Delta g$  (bottom right) at  $3 \text{ (GeV/c)}^2$ . This analysis (continuous blue line) is compared to LSS [95] (dotted yellow and dashed-dotted pink lines), DSSV [96] (dashed red line) and NNPDFpol [97] (dashed teal line) collaborations.

Table 4.9: Comparison of truncated  $\Delta G$  to the range  $[0.05, 0.2]$  at  $Q^2 = 3 \text{ (GeV/c)}^2$ .

DSSV Estimated from results in [96]	COMPASS		
	ffP	ff0	ffN
0.09	0.19	0.03	-0.23

The first moments from the various fits including different kind of data are compared to each other in Table 4.10. Although, the other results are given at different  $Q^2$  (as they are published) the evolution of  $\Delta\Sigma$  within this range of the scale is pretty weak and the results could be compared. They are all compatible with the present analysis (COMPASS) with a trend to small value of  $\Delta\Sigma$  with respect to the range given by the present analysis. Notice that the DSSV value given here corresponds to a truncated moment but is also close to 0.26 when computed over the full interval.

For  $\Delta G$ , only the collaborations including the RHIC spin data can derive from the fits a significant positive value for the truncated moment. However, over the full interval the range of uncertainties becomes as large as the one from COMPASS.

<sup>1</sup>Truncated first moment  $\Delta\Sigma$  to the range  $[0.001, 1]$  [76].

<sup>2</sup>Truncated first moment  $\Delta G$  to the range  $[0.05, 0.2]$  [96].

<sup>3</sup>Truncated first moment  $\Delta G$  to the range  $[0.05, 0.2]$ .

Table 4.10: First moment of  $\Delta\Sigma$  and  $\Delta G$  from different fits using different inputs. The results are given at the relevant scale of extraction as published.

Collaboration	Data			$\Delta\Sigma$	$\Delta G$
	DIS	SIDIS	RHIC		
COMPASS: 3 (GeV/c) <sup>2</sup>	✓	✗	✗	$0.26 \leq \Delta\Sigma \leq 0.33$	$-1 \leq \Delta G \leq 0.5$
LSS: 4 (GeV/c) <sup>2</sup> [95]	✓	✓	✗	$0.207 \pm 0.034$	$0.316 \pm 0.190$
DSSV <sup>1,2</sup> : 10 (GeV/c) <sup>2</sup> [76, 96]	✓	✓	✓	$0.254 \pm 0.042$	$-0.339 \pm 0.458$
DSSV <sup>1,2</sup> : 10 (GeV/c) <sup>2</sup> [76, 96]	✓	✓	✓	$0.366^{+0.042}_{-0.062}$	$0.010^{+0.06}_{-0.07}$
NNPDFpol1.1 <sup>3</sup> : 10 (GeV/c) <sup>2</sup> [98]	✓	✗	✓	$0.18 \pm 0.21$	$0.17 \pm 0.06$

#### 4.1.6 Further steps for QCD analysis

The results shown so far correspond to a first iteration of the analysis. Since then, few defects has been identified. Solutions to fix those irregularities are proposed in this section but only cursory and preliminary results are presented. The main ideas are the following:

- A better treatment of the positivity constraint
- A stricter cut on  $W^2$  to ensure the selection of data not affected by higher twist effects.
- A restriction to pure  $g_1$  data (discard open charm muoproduction result)

The treatment of the positivity constraint, which was restricted to the  $\Delta(s + \bar{s})$  and  $\Delta g$  distributions, is being generalised to  $\Delta(u + \bar{u})$  and  $\Delta(d + \bar{d})$ . Adding two terms to the  $\chi^2$  of the forms of the one already defined in section 4.1.1 does not lead to a convergent fit. Instead, the penalty term of Eq. (4.8) due to the violation of positivity, was changed to the form of [99]:

$$\chi_{positivity}^2 = \sum_{0.1 < x \in \text{grid}} \frac{1}{33} \left( e^{K_u[\Delta(u+\bar{u})-(u+\bar{u})]} + e^{K_d[\Delta(d+\bar{d})-(d+\bar{d})]} + e^{K_s[\Delta(s+\bar{s})-(s+\bar{s})]} + e^{K_g[\Delta g - g]} \right) \quad (4.16)$$

where the  $K_q$  factors are arbitrary fixed and represent the strength of the positivity condition. In contrast to the previous definition of the penalty, the condition is always checked whether the positivity condition is violated or not and introduces a bias. To limit this bias, the penalty term is normalised by 33, the value corresponding to the number of  $x$  points above 0.1 in the grid. In this way, even when the polarised distributions converge towards the unpolarised one<sup>4</sup>, the bias is only of one. Moreover, it is checked at the end of the fit that the penalty contribution is negligible compared to the global  $\chi^2$ . The advantage of this definition is a smoother penalty when converging close to the unpolarised distribution. New solutions of the fits were obtained with a reduced positivity violation.

The normalisation of the CLAS data contributes now even more significantly to the global  $\chi^2$ . As those data are the more precise in the high- $x$  region and measured at a relatively low value of  $Q^2$ , the apparent incompatibility with the positivity condition is thought to come from higher twist effects. When removing those data, the  $\chi^2$  of the new solutions are comparable to the one of the results presented here and the positivity conditions are satisfied within the polarised and unpolarised PDF uncertainties. Parts of other data may be affected by higher twist effects, instead of removing the CLAS data, a stricter cut on  $W$  like NNPDF [97] is

<sup>4</sup>For instance, it is expected that  $\Delta u \xrightarrow{x \rightarrow 1} u$ .

investigated. The preliminary results (not detailed here) favour two solutions of the fits ( $\Delta G \sim 0$  and  $\Delta G > 0$ ) to the detriment of the  $\Delta G < 0$  one. As a consequence, the range for  $\Delta\Sigma$  would be reduced to  $[0.25;0.29]$ . More studies are planned (impact of the choice of reference scale and exploring several values of  $K_q$ ).

The results on the proton and deuteron first moments should stay valid as the positivity constrains have a small impact on the spin structure function. Figures 4.17, shows the values of the proton and the deuteron first moments evaluated from the COMPASS data for several models and especially for the results of the fit presented and the new preliminary results. No significant effect is noticeable.

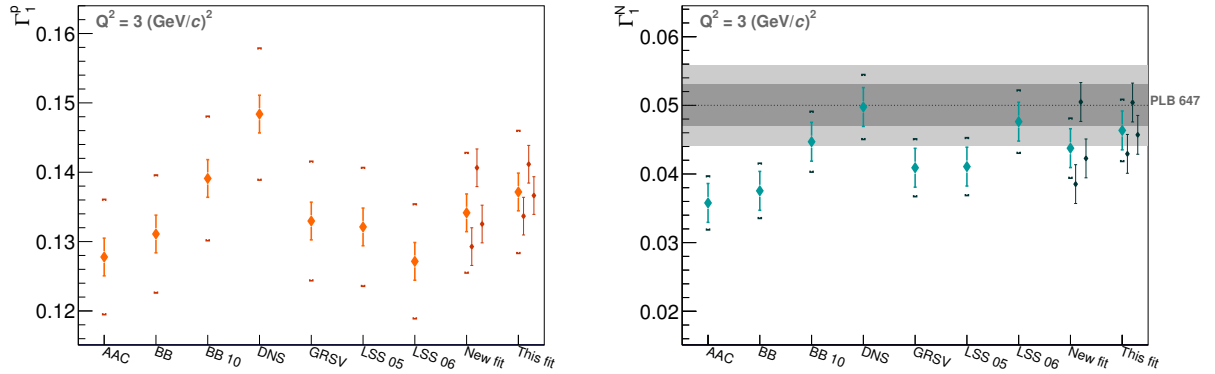


Figure 4.17: Comparison of the first moment  $\Gamma_1^p$  and  $\Gamma_1^d$  extracted from the data after evolution according to different models. “This fit” refers to section 4.1.3 and the “New fit” to section 4.1.6.

## 4.2 Bjorken sum rule

The Bjorken sum rule relates the first moment of  $g_1^{NS}$  to the ratio of the axial-vector to vector weak coupling constant  $g_A/g_V$  (see section 1.3.2). The non-singlet spin structure function  $g_1^{NS}$  can be calculated by combining the  $g_1$  proton and deuteron data together:

$$g_1^{NS}(x, Q^2) = g_1^p(x, Q^2) - g_1^n(x, Q^2) = 2 \left[ g_1^p - \frac{g_1^d}{1 - 1.5\omega_D} \right]. \quad (4.17)$$

where  $\omega_D = 0.05 \pm 0.01$  represents the D-state probability of the deuteron. An evaluation of the Bjorken sum rule is performed with the new data at 200 GeV, which slightly extend the measured range from  $x = 0.004$  to  $x = 0.0025$ . As  $g_1^{NS}$  is only related to  $\Delta q_3$  the non-singlet quark distribution of SU(2) flavour symmetry, only few parameters are needed. Moreover, as a non-singlet distribution, its evolution is decorrelated from  $\Delta g$  and a wide kinematic coverage in the  $(x, Q^2)$  plane is not mandatory as long as precise data covering a wide range of  $x$  are available. Unlike in the previous section, the fit of  $g_1^{NS}$  is performed to the COMPASS data alone. Thus the previously published COMPASS data [27, 28] are combined with the 200 GeV data according to Eq. (4.17). However, as the 200 GeV data have a slightly larger  $\langle Q^2 \rangle$  than the previous measurements at 160 GeV, the deuteron and proton data cannot be combined directly, they first need to be evolved to the same scale.

### 4.2.1 $Q^2$ evolution and data combination

The data are evolved according to Eq. (4.18), which relies on the results of the fits to the spin structure functions  $g_1$ .

$$g_1^{\text{data}}(x, Q_0^2) = g_1^{\text{data}}(x, \langle Q^2 \rangle) + [g_1^{\text{fit}}(x, Q_0^2) - g_1^{\text{fit}}(x, \langle Q^2 \rangle)] \quad (4.18)$$

To minimise the uncertainty on the evolution, due to the formula itself and to the uncertainties on  $g_1^{\text{fit}}$ , the evolution is limited to a small  $Q^2$  range: the 200 GeV proton data are evolved to the kinematics of the 160 GeV proton data. The deuteron data are at a slightly smaller scale due to differences in the trigger mix, so they are evolved to the  $Q^2$  of the proton data. Then, the proton and the deuteron data are combined according to Eq. (4.17). For the new data point at  $\langle x \rangle = 0.0036$  no corresponding value of  $g_1^d$  was measured so a data point is inferred based on the value of the  $g_1^d$  fit. The procedure for  $g_1^{\text{NS}}$  computation through evolutions and for the fit is illustrated in Fig. 4.18 together with the  $x$ - $Q^2$  initial values of the data.

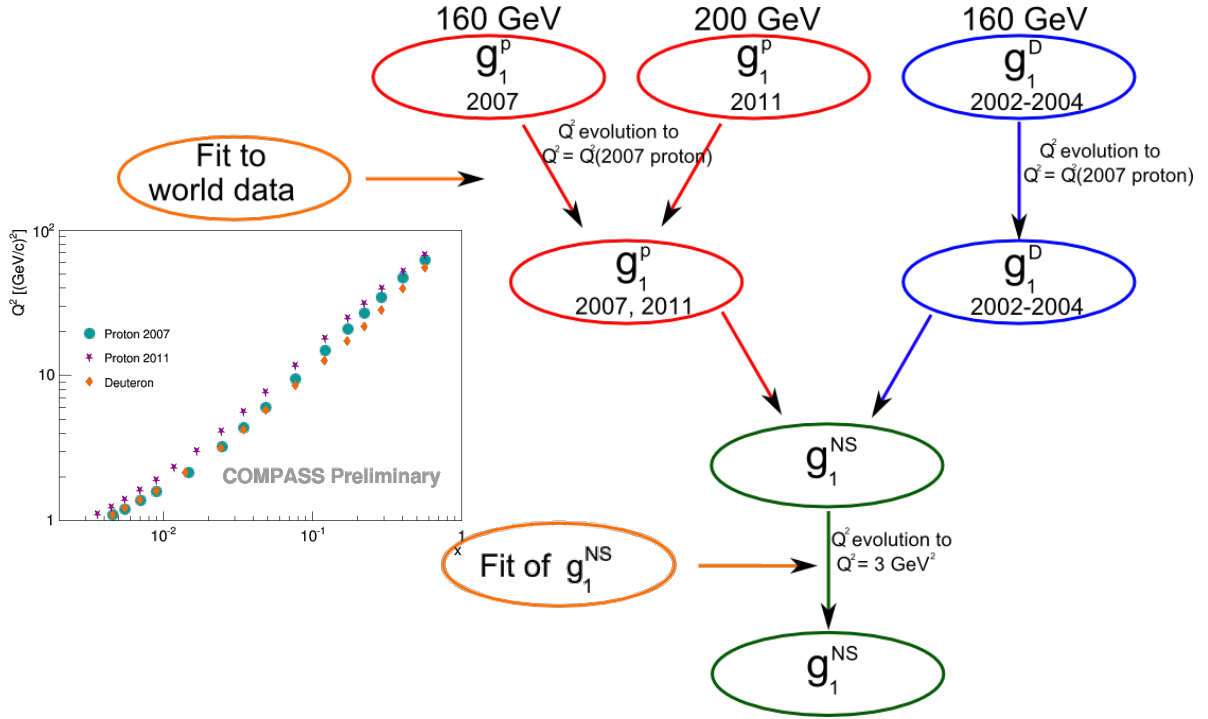


Figure 4.18: Illustration of the different steps to calculate  $g_1^{\text{NS}}$  from the 160 and 200 GeV proton and 160 GeV deuteron data together with the average  $x$ - $Q^2$  values for the various data taking.

### 4.2.2 Fit of $g_1^{\text{NS}}$

The COMPASS data are fitted with the same program as the one used for the NLO fit to the world data but restricted to the non-singlet case and  $\Delta q_3$  determination. The following functional form for  $\Delta q_3$  at a reference scale  $Q_0^2 = 1 \text{ (GeV/c)}^2$  is assumed:

$$\Delta q_3(x, Q_0^2) = \eta_3 \frac{x^{\alpha_3} (1-x)^{\beta_3}}{\int_0^1 x^{\alpha_3} (1-x)^{\beta_3} dx}, \quad (4.19)$$

as in section 4.1.2 but this time the  $\eta_3$  parameter is left free. The distribution is evolved to the  $Q^2$  of the data according to Eq. (4.2). It is next convoluted to the Wilson coefficient to obtain

$g_1^{NS}$ :

$$g_1^{NS}(x, Q^2) = \frac{1}{6} \int_x^1 C^{NS}\left(\frac{x}{x'}, \alpha_s(Q^2)\right) \Delta q_3(x', Q^2) \quad (4.20)$$

A simple  $\chi^2$ , taking into account only the statistical uncertainties of the data points, is minimised to determine the value of the parameters:

$$\chi^2 = \sum_{i=1}^{16} \left( \frac{g_1^{NS,fit}(x_i, Q_i^2) - g_1^{NS,data}}{\sigma_i^{stat}} \right)^2. \quad (4.21)$$

Only three parameters are fitted out of sixteen data points.

The Bjorken sum rule can be checked in two ways: directly from the value of the  $\eta_3$  parameter or indirectly from  $\Gamma_1^{NS}$  the first moment of  $g_1^{NS}$ , which are expected to give  $g_A/g_V$  and  $\frac{1}{6}g_A/g_V$  at LO, respectively. The two methods are presented below.

### 4.2.3 Extraction of $g_A/g_V$ from the fit

The results from the fit are given in table 4.11.

Table 4.11: Results of the fits of  $\Delta q_3$  at  $Q_0^2 = 1$  (GeV/c)<sup>2</sup>.

NS Parameter (prelim.)	
Param.	Value
$\eta_3$	$1.24 \pm 0.06$
$\alpha_3$	$-0.11 \pm 0.08$
$\beta_3$	$2.2^{+0.5}_{-0.4}$
$\chi^2/ndf$	8.1/13

Although the systematic uncertainties were neglected, a very good value of  $\chi^2$  is obtained and more complicated functional forms are thus disregarded. The value of the  $\eta_3$  parameter is in very good agreement with the value of  $1.2701 \pm 0.0025$  reported in the PDG.

This value is independent of the scale and therefore the  $\eta_3$  parameter must be independent of the choice of reference scale  $Q_0^2$ . The fit is therefore performed again with the same functional form defined at  $Q_0^2$  equal 1.5, 3.0, 5.0 and 9.0 (GeV/c)<sup>2</sup>. The results are given in 4.12. As

Table 4.12: Parameters of NLO QCD fit to  $g_1^{NS}$  data for several reference scales  $Q_0^2$ .

$Q_0^2$ (GeV/c) <sup>2</sup>	$\eta_3$	$\alpha_3$	$\beta_3$
1.5	$1.233 \pm 0.056$	$-0.158 \pm 0.070$	$2.35 \pm 0.42$
3.0	$1.233 \pm 0.056$	$-0.212 \pm 0.062$	$2.52 \pm 0.42$
5.0	$1.234 \pm 0.056$	$-0.242 \pm 0.057$	$2.63 \pm 0.42$
9.0	$1.235 \pm 0.056$	$-0.269 \pm 0.053$	$2.75 \pm 0.42$

expected, the value of the  $\eta_3$  parameter remains the same when changing the value of  $Q_0^2$ . The parameters  $\alpha_3$  and  $\beta_3$  vary with  $Q_0^2$  as also expected from the evolution.

The Bjorken sum rule is verified with 4.5% with this method which is based on the statistical uncertainties of the data only.

The second method below takes into account the data systematic uncertainties, which can more easily be propagated in this case.

#### 4.2.4 Extraction of $g_A/g_V$ from the data

The value of  $g_A/g_V$  is also related to the first moment  $\Gamma_1^{NS}$  of  $g_1^{NS}$ . In  $\overline{\text{MS}}$ , this relation is:

$$\Gamma_1^{NS}(Q^2) = \int_0^1 g_1^{NS}(x, Q^2) dx = \frac{1}{6} C^{NS}(Q^2) \left| \frac{g_A}{g_V} \right| \quad (4.22)$$

when higher twist terms are neglected. The non-singlet coefficient function  $C^{NS}(Q^2)$  is expressed as a power series in  $\alpha_s$  calculated up to the third order, for four active quark flavours [100]:

$$C^{NS}(Q^2) = \underbrace{1}_{LO} - \underbrace{\left(\frac{\alpha_s}{\pi}\right)}_{NLO} - \underbrace{3.25 \cdot \left(\frac{\alpha_s}{\pi}\right)^2}_{NNLO} - \underbrace{13.85026 \cdot \left(\frac{\alpha_s}{\pi}\right)^3}_{NNNLO}. \quad (4.23)$$

To evaluate  $\Gamma_1^{NS}$ , as the data points on  $g_1^{NS}$  are at different  $Q^2$ , they are first evolved to the average measured scale of the experiment. The evolution is made in the same way as in Eq. (4.18) to bring the measurements to a common  $\langle Q^2 \rangle = 3$  (GeV/c)<sup>2</sup> for the whole  $x$  range. This time,  $g_1^{data}$  corresponds to the “measured”  $g_1^{NS}$  and  $g_1^{fit}$  to the fitted parametrisation of  $g_1^{NS}$ . The systematic uncertainty from this evolution is expected to be smaller than the one based on the fit to the world data, as the evolution of the non-singlet spin structure function does not depend on  $\Delta g$ . The evaluation of  $\Gamma_1^{NS}$  relies on two different contributions, one from the measured range of the data and one from the unmeasured ranges for  $x \rightarrow 0$  and  $x \rightarrow 1$ . For the  $x$  range of the data, the integral is calculated according to Eq. (4.13). The contribution from the unmeasured range is calculated from a numerical integration of the non-singlet fit results within the grid (as in Eq. (4.14) with  $g_1^{NS}$  instead of  $g_1^p$  or  $g_1^d$ ) and from a linear extrapolation of the fit result for the integral down to  $x = 0$ . Figure 4.19 left shows the non-singlet data points after evolution to  $\langle Q^2 \rangle$  and compared to the fit. As already mentioned, the data and the fit agree well to each other.

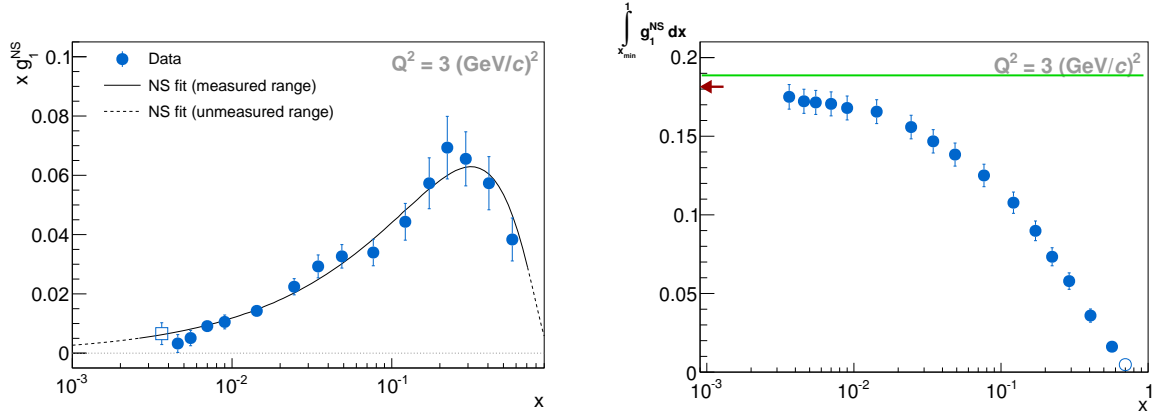


Figure 4.19: Left: Values of  $g_1^{NS}(x)$  at  $Q^2 = 3$  (GeV/c)<sup>2</sup> from the  $g_1^d$  and  $g_1^p$  data (closed circles) and from the combined  $g_1^p$  data and  $g_1^d$  NLO QCD fit result (open square). Right:  $\int_{x_{min}}^1 g_1^{NS} dx$  as a function of  $x_{min}$  from the extrapolation of the fit (open circle) and completed with the data points (closed circles). The arrow shows the value for the full range  $0 < x < 1$  and the green line the expected results at NLO and leading twist.

The value of the integral evaluated from the data with the extrapolation from the fit is shown in Fig. 4.19 right. The combined 200 GeV proton data and  $g_1^d$  NLO fit add a new “measured” point at  $x = 0.0036$  that confirms the beginning of the asymptotic behaviour of  $\int_x^1 g_1^{NS}(x) dx$ . The resulting  $\Gamma_1^{NS}$  is indicated by the arrow on the y-axis. The different contributions to the integral are given in Table 4.13 and 94% of the extrapolated  $\Gamma_1^{NS}$  comes from the measured

range. The contribution from the range of  $0.7 < x \leq 1$  corresponds to 2.3% of  $\Gamma_1^{NS}$  whereas the contribution for  $0 \leq x < 0.0025$  accounts for 3.7%.

Table 4.13: First moment  $\Gamma_1^{NS}$  at  $Q^2 = 3 \text{ (GeV/c)}^2$ . The different contributions of the evaluation of the integral of  $g_1^{NS}$  (see text) and the resulting first moment  $\Gamma_1^{NS}$  at  $Q^2 = 3 \text{ (GeV/c)}^2$ .

Contribution to $\Gamma_1^{NS}$ (Prelim.)	
$x$ range	$\Gamma_1^{NS}$
0 – 0.0025	0.0064
0.0025 – 0.7	$0.170 \pm 0.008$
0.7 – 1.0	0.0047
0 – 1	$0.181 \pm 0.008$

The systematic uncertainties on  $\Gamma_1^{NS}$  come mainly from the uncertainties associated to the measurements of  $g_1^p$  and  $g_1^d$ . They comprise the beam and target polarisation uncertainties as well as the uncertainties on the dilution factors and the depolarisation factor. The other contributions are either negligible or should compensate in the computation of  $g_1^{NS}$  as both proton and deuteron data come from the same experiment. The errors from the extrapolation and the evolution to a common  $Q^2$  are found to be negligible as in [28], and will be discussed later. The different contributions to the systematics uncertainties are given in Table 4.14.

Table 4.14: Relative systematic uncertainties for the different data samples.

Systematic uncertainties (prelim.)			
	Deuteron 160 GeV	Proton 160 GeV	Proton 200 GeV
Beam polarisation	5%		
Target polarisation	5%	2%	3.5%
Depolarisation factor	2%	2%	2%
Dilution factor	2%	1%	2%
Combined(target, dep., dil.)	6%	3.6%	

For the full  $x$  range a value of

$$\Gamma_1^{NS}(Q^2 = 3 \text{ (GeV/c)}^2) = 0.181 \pm 0.008(\text{stat.}) \pm 0.014(\text{syst.}) \text{ (Prelim.)} \quad (4.24)$$

is obtained. Using the NLO coefficient function  $C_1^{NS}(Q^2)$  at  $Q^2 = 3(\text{GeV/c})^2$ , one obtains Eq. (4.25).

The result is dominated by the systematic error, where the largest contributions are from the uncertainty on the beam polarisation, which is common to all data sets and from the absolute contribution from the proton data normalisation (see Table 4.15). To ensure that the

Table 4.15: Absolute contributions to the systematic uncertainties of  $g_A/g_V$ .

Syst. uncertainties on $g_A/g_V$ (prelim.)	
Beam polarisation	0.061
Deuteron data	0.033
Proton data	0.064

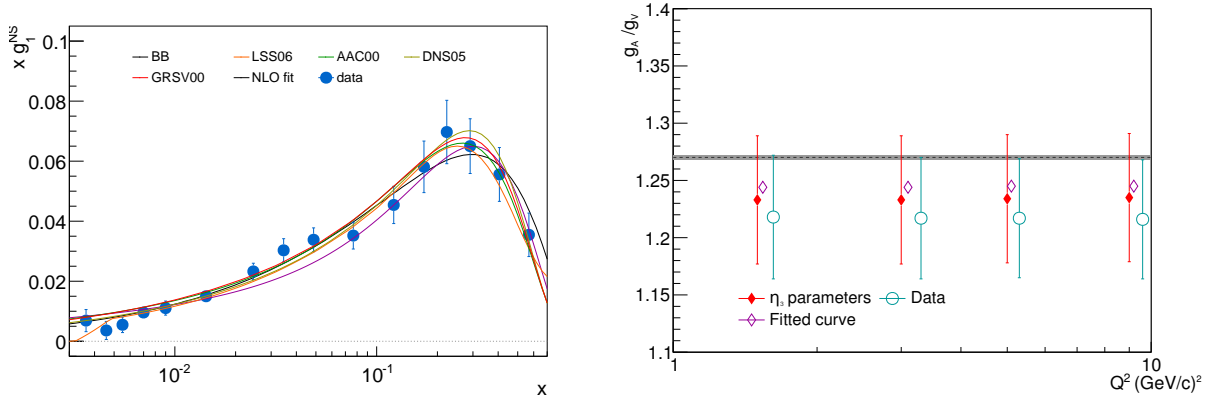


Figure 4.20: Left: Comparison of  $x \cdot g_1^{NS}$  from different models to the data at  $\langle Q^2 \rangle = 3 \text{ (GeV/c)}^2$ . Right: Comparison of  $g_A/g_V$  extraction at different  $Q_0^2$  values.

uncertainty on the contribution coming from the extrapolation of the integral can be neglected, several parametrisations [101, 102, 103, 104, 105] were taken, different  $Q_0^2$  values were explored between 1 and 10  $(\text{GeV/c})^2$  and the results were compared to the one obtained from Table 4.7. Figure 4.20 left shows the comparison at  $\langle Q^2 \rangle$  of different models to the data. The differences of the contribution from the extrapolated region are found to be within 0.8% of  $g_A/g_V$ . The variation of  $g_A/g_V$  when changing  $Q_0^2$  were found to be of the order of 0.3% (Fig. 4.20 right).

In comparison to the value of  $g_A/g_V$  obtained from the neutron  $\beta$  decay Eq. (4.26) [12], the *Bjorken sum rule* is verified with 8.5% accuracy.

$$g_A/g_V = 1.220 \pm 0.053(\text{stat.}) \pm 0.095(\text{syst.}) \quad (\text{Prelim.}) \quad (4.25)$$

$$g_A/g_V = 1.2701 \pm 0.002|_{\beta \text{ decay}} \quad (4.26)$$

The results is obtained at NLO whereas the one from the beta decay measurements takes into account all orders. To estimate the size and the direction in which further orders will influence the results, the value of  $g_A/g_V$  using the NNLO coefficient function  $C_1^{NS}(Q^2)$  is evaluated. In this case,

$$g_A/g_V = 1.256 \pm 0.054 \pm 0.098 . \quad (\text{Prelim.}) \quad (4.27)$$

is found and the *Bjorken sum rule* is verified with 8.8% accuracy.

#### 4.2.5 Comparison of the Bjorken sum rule to other analysis

Compared to the previous COMPASS result [28], the contribution from the extrapolation to  $x = 0$  is now 31.6% smaller than before. The result for  $\Gamma_1^{NS}$  agrees well with the previous one ( $0.190 \pm 0.009 \pm 0.015$ ). The precision of the result is improved by about a factor of 12% in terms of statistical uncertainties and 7.1% for the systematics uncertainties due to the lower value of  $\Gamma_1^{NS}$ . A gain of 25% of precision could be achieved by reducing the Monte-Carlo beam polarisation uncertainties to 4%, as it was achieved in the past.

This present result is also compatible within  $1.5 \sigma_{\text{stat.}}$  with the latest extraction of CLAS [106] including higher twist corrections, which reported a value of  $0.1697 \pm 0.0005|_{\text{stat.}} \pm 0.0171|_{\text{sys.}}$  at  $Q^2 = 3.22 \text{ (GeV/c)}^2$ . That result is slightly below the extraction presented here with a better statistical error bar and slightly larger systematics uncertainties. The dominant part of their systematic uncertainties comes from the models used for extrapolating  $\Gamma_1^{NS}$  from  $x \sim 0.36$  down to  $x = 0$  ( $\sim 80\%$  of the first moment). Indeed, unlike this study, the  $x$ -bin data are not evolved to a common  $Q^2$  value therefore for a given scale only a limited  $x$  domain is covered by experimental data.

### 4.3 Key information of the chapter

A NLO global QCD fit of the  $g_1^p$ ,  $g_1^d$  and  $g_1^n$  world data has been performed. This includes the latest 200 GeV  $g_1^p$  data and the NLO open charm  $\Delta G$  extraction. Overall, 679 data points are fitted using about 11 parameters for the functional forms of the polarised quark singlet, non-singlet and gluon distributions and 18 parameters for the normalisation of the experiments.

Three categories of functional forms describing equally well the data are kept. They can identify with a positive, compatible with zero and negative gluon polarisation. The dominant uncertainty on the fit results comes from the choice of the functional forms. Taking into account the propagated statistical uncertainties of the data and the uncertainties on the functional forms, the quark polarisation  $\Delta\Sigma$  ranges from 0.26 to 0.33 and the gluon polarisation  $\Delta G$  from  $-1$  to 0.5 at  $3 \text{ (GeV}/c)^2$  in the  $\overline{\text{MS}}$  scheme.

Other global NLO QCD fits give compatible results for  $\Delta\Sigma$  yet with a general trend towards the lower bound. For  $\Delta G$ , the two (positive and compatible with zero) solutions for the truncated first moment are compatible with the DSSV and NNPDFpol fits, which include the precise  $\Delta G$  sensitive RHIC spin data. The sensitivity of the inclusive data to  $\Delta G$  is very limited.

A test of the Bjorken sum rule is performed on the COMPASS  $g_1^p$  and  $g_1^d$  data alone. Including the  $g_1^p$  data from the previous chapter reduces the contribution from the unmeasured region in the evaluation of the first moment by about 70% and improves the statistical accuracy by 12%. The Bjorken sum rule is verified with 9% accuracy. This result is in agreement with both the previous COMPASS and the latest CLAS publication.

# Conclusion

The spin internal structure of the proton has been studied via neutral current polarised deep inelastic scattering  $\bar{\mu}\vec{p} \rightarrow \mu'X$ , which is one of the cleanest process available to probe hadrons. The data were taken on a polarised  $\text{NH}_3$  target with the COMPASS experiment and using the most energetic polarised muon beam (200 GeV) available in the world. About  $80 \cdot 10^6$  DIS events were collected to extract the double longitudinal spin asymmetry of the proton  $A_1^p$  and the derived proton spin dependent structure function  $g_1^p$ . The kinematic domain covered by those data extend the world kinematic coverage down to  $x = 0.0036$  and up to  $Q^2 \simeq 100$   $(\text{GeV}/c)^2$ . The new data set completes the previous COMPASS measurement obtained at 160 GeV with comparable statistics. From the combined results, about a factor of three in statistical precision is obtained compared to the previous SMC experiment for a similar beam time. The dominant systematic uncertainty comes from the uncertainties on the experimental false asymmetry contribution and represents a factor of 30% to 80% of the statistical precision. It is mainly evaluated from statistical tests on the data. The advantage of the method is its reliability in reflecting the experimental condition. The drawback is a conservative estimation of the uncertainties due to the limited statistics.

Polarised PDFs were extracted from a NLO ( $\overline{\text{MS}}$ ) QCD fit of world inclusive DIS  $g_1^p$ ,  $g_1^d$  and  $g_1^n$  data including the present  $g_1^p$  results at 200 GeV and the NLO direct extraction of the gluon polarisation  $\Delta G$  from the COMPASS open charm channel. Depending on the choice of functional forms postulated in the fit, three categories of solutions corresponding to a positive, compatible with zero and negative  $\Delta G$  value are found. As a consequence, the choice of functional forms constitutes the dominant uncertainty. The solution for the first moment of the quark spin contribution to the nucleon spin,  $\Delta\Sigma$ , ranges from 0.256 to 0.335 at  $Q^2 = 3$   $(\text{GeV}/c)^2$ . This is in agreement with other NLO QCD fits like the ones from the LSS, DSSV and NNPDFpol collaborations, which include additional data sets. The first moment  $\Delta G$ , which is not well constrained by inclusive data, is found to be within -1 and 0.5 at  $Q^2 = 3$   $(\text{GeV}/c)^2$ . The positive and with a node solutions, that correspond also to the best  $\chi^2$  fit results of this analysis, are in agreement with the DSSV and NNPDFpol truncated  $\Delta G$  first moment, which is better constrained due to the inclusion of the precise gluon sensitive RHIC spin data.

The first moments of the spin structure functions are evaluated from the COMPASS data alone in the measured range, once they are evolved to a common scale. The results of the fit to the world inclusive data are used to perform both the data evolution and the evaluation of the integral in the unmeasured regions. At  $Q^2 = 3$   $(\text{GeV}/c)^2$ , the first moment is:  $\Gamma_1^p = 0.1372 \pm 0.0027|_{\text{stat.}} \pm 0.0084|_{\text{syst.}} \pm 0.0031|_{\text{evol.}}$  for the proton,  $\Gamma_1^d = 0.0463 \pm 0.0028|_{\text{stat.}} \pm 0.0035|_{\text{syst.}} \pm 0.0031|_{\text{evol.}}$  for the deuteron and  $\Gamma_1^n = -0.0445 \pm 0.0063|_{\text{stat.}} \pm 0.0112|_{\text{syst.}} \pm 0.0031|_{\text{evol.}}$  for the neutron. They all violate, as already reported, the Ellis-Jaffe sum rule.

Finally, a completely independent NLO fit based on the proton and deuteron COMPASS data alone is performed to verify the Bjorken sum rule. The result of this fit is used to both evolve the measurements to a common scale and to extrapolate the value of the integral outside of the  $x$ -range covered by the data. The first moment of the non-singlet spin structure function is found to be  $\Gamma_1^{NS} = 0.181 \pm 0.008|_{\text{stat.}} \pm 0.014|_{\text{syst.}}$ , where 94% of the value is evaluated from

the data. Compared to the previous COMPASS evaluation of the Bjorken sum rule, the contribution from the unmeasured region is 30% smaller. The statistical uncertainties are reduced by about a factor of 12% and the systematic errors by 7%. The verification of the Bjorken sum rule is now verified with 8.5% accuracy.

The QCD analysis suffers from a limited kinematic coverage of the current inclusive data and their limited precision. The 200 GeV data do not change much the general trend of the PDFs but a reduction of the uncertainties on the PDFs was observed. This fact will be quantified, once the further steps of the QCD analysis discussed in section 4.1.6 are finished.

Finally, it must be stressed that a future polarised electron-ion collider would allow for a major breakthrough, by opening up the kinematic domain to much larger  $Q^2$  values and lower  $x$  values, which constitutes the most limiting aspect in determining  $\Delta G$  from  $g_1$  data.

# Bibliography

- [1] F. Halzen et al., QUARKS & LEPTONS: an introductory course in modern particle physics, John Wiley & Sons, Inc., 1984.  
*Cited on page 4.*
- [2] Manohar, Aneesh V., An introduction to spin dependent deep inelastic scattering, [arXiv:hep-ph/9204208] .  
*Cited on pages 5 and 12.*
- [3] L. N. Hand, Experimental investigation of pion electroproduction, Phys. Rev. 129 (1963) 1834.  
*Cited on page 6.*
- [4] P. Anthony et al., Precision measurement of the proton and deuteron spin structure functions  $g_2$  and asymmetries  $A_2$ , Phys. Lett. B 553 (1–2) (2003) 18 .  
*Cited on pages 7 and 53.*
- [5] D. Adams et al., Spin asymmetry in muon-proton deep inelastic scattering on a transversely-polarized target , Phys. Lett. B 336 (1) (1994) 125 .  
*Cited on page 7.*
- [6] K. Abe et al., Measurements of the proton and deuteron spin structure functions  $g_1$  and  $g_2$ , Phys. Rev. D 58 (1998) 112003.  
*Cited on page 7.*
- [7] M. Breidenbach et al., Observed behavior of highly inelastic electron-proton scattering, Phys. Rev. Lett. 23 (1969) 935.  
*Cited on page 8.*
- [8] A. Bodek et al., Experimental studies of the neutron and proton electromagnetic structure functions, Phys. Rev. D 20 (1979) 1471.  
*Cited on page 8.*
- [9] M. Stratmann, Lecture on perturbative QCD or from basic principles to current applications, in: PHENIX Spin Fest @ RIKEN Wako, 2005.  
*Cited on page 9.*
- [10] G. Sterman et al., Handbook of perturbative QCD, Rev. Mod. Phys. 67 (1995) 157.  
*Cited on page 9.*
- [11] A. Martin et al., Parton distributions for the LHC, The European Physical Journal C 63 (2) (2009) 189.  
*Cited on pages 11, 12, 65, 66, and 68.*
- [12] W.-M. Yao et al., Review of particle physics, J. Phys. G 33 (2006) 1+.  
*Cited on pages 12, 15, 35, and 89.*

- [13] E. Leader, Spin in particle physics, Camb. Monogr. Part. Phys. Nucl. Phys. Cosmol. 15 (2001) 1.  
*Cited on page 13.*
- [14] S. D. Bass, The Spin structure of the proton, World scientific, 2007.  
*Cited on page 13.*
- [15] S. L. Adler, Axial-Vector vertex in spinor electrodynamics, Phys. Rev. 177 (1969) 2426.  
*Cited on page 13.*
- [16] J. Bell et al., A PCAC puzzle:  $\pi^0 \rightarrow \gamma\gamma$  in the  $\sigma$ -model, Il Nuovo Cimento A 60 (1) (1969) 47.  
*Cited on page 13.*
- [17] J. Ellis et al., Sum rule for deep-inelastic electroproduction from polarized protons, Phys. Rev. D 9 (1974) 1444.  
*Cited on page 14.*
- [18] J. Ashman et al., An investigation of the spin structure of the proton in deep inelastic scattering of polarised muons on polarised protons, Nucl. Phys. B 328 (1) (1989) 1.  
*Cited on pages 14 and 67.*
- [19] B. Lampe et al., Spin physics and polarized structure functions, Physics Reports 332 (1–3) (2000) 1.  
*Cited on page 14.*
- [20] M. Stolarski, Spin structure of the nucleon at low  $x$  and low  $Q^2$  in the COMPASS experiment at CERN, Ph.D. thesis, University of Warsaw (2006).  
*Cited on pages 14 and 54.*
- [21] J. D. Bjorken, Applications of the chiral  $U(6) \otimes U(6)$  algebra of current densities, Phys. Rev. 148 (1966) 1467.  
*Cited on page 14.*
- [22] J. D. Bjorken, Inelastic scattering of polarized leptons from polarized nucleons, Phys. Rev. D 1 (1970) 1376.  
*Cited on page 14.*
- [23] G. Baum et al., COMPASS: A Proposal for a Common Muon and Proton Apparatus for Structure and Spectroscopy, Tech. rep., CERN (1996).  
*Cited on page 17.*
- [24] G. Baum et al., COMPASS : Common Muon and Proton Apparatus for Structure and Spectroscopy, Tech. rep., CERN (1996).  
*Cited on page 17.*
- [25] E. Ageev et al., Gluon polarization in the nucleon from quasi-real photoproduction of high- $p_T$  hadron pairs, Phys. Lett. B 633 (1) (2006) 25.  
*Cited on page 17.*
- [26] C. Adolph et al., Leading and next-to-leading order gluon polarization in the nucleon and longitudinal double spin asymmetries from open charm muoproduction, Phys. Rev. D 87 (2013) 052018.  
*Cited on pages 17, 67, 80, and 81.*

- [27] V. Alexakhin et al., The deuteron spin-dependent structure function and its first moment, Phys. Lett. B 647 (1) (2007) 8.  
*Cited on pages 17, 67, and 84.*
- [28] M. Alekseev et al., The spin-dependent structure function of the proton and a test of the Bjorken sum rule, Phys. Lett. B 690 (5) (2010) 466 .  
*Cited on pages 17, 44, 67, 84, 88, and 89.*
- [29] COMPASS Collaboration, Addendum 2 to the COMPASS Proposal, Tech. rep., CERN (2009).  
*Cited on page 17.*
- [30] F. Gautheron et al., COMPASS-II Proposal, Tech. Rep. CERN-SPSC-2010-014. SPSC-P-340, CERN, Geneva (May 2010).  
*Cited on page 17.*
- [31] N. Makke, Measurement of the polarisation of strange quarks in the nucleon and determination of quark fragmentation functions into hadrons, Ph.D. thesis, Université Paris-Sud XI (2011).  
*Cited on page 18.*
- [32] P. Abbon et al., The COMPASS experiment at CERN, NIM A 577 (3) (2007) 455 .  
*Cited on pages 18, 19, 24, 27, and 45.*
- [33] N. Doble et al., The upgraded muon beam at the SPS, NIM A 343 (2–3) (1994) 351 .  
*Cited on pages 19 and 20.*
- [34] C. Iselin, HALO, a computer program to calculate muon halo, Tech. Rep. CERN 74-17, CERN (1974).  
*Cited on page 20.*
- [35] D. Adams et al., Measurement of the SMC muon beam polarisation using the asymmetry in the elastic scattering off polarised electrons, NIM A 443 (1) (2000) 1 .  
*Cited on page 20.*
- [36] B. Adeva et al., Measurement of the polarisation of a high energy muon beam, NIM A 343 (2–3) (1994) 363 .  
*Cited on page 20.*
- [37] G. Mallot, The Spin Structure of the Nucleon from the SMC Experiments, Habilitation theses, Fachbereich Physik der Johannes Gutenberg-Universität Mainz (1996).  
*Cited on page 21.*
- [38] A. Abragam et al., Principles of dynamic nuclear polarisation, Reports on Progress in Physics 41 (3) (1978) 395.  
*Cited on page 21.*
- [39] D. G. Crabb et al., Solid polarized targets for nuclear and particle physics experiments, Annual Review of Nuclear and Particle Science 47 (1) (1997) 67.  
*Cited on page 22.*
- [40] B. Adeva et al., Measurement of proton and nitrogen polarization in ammonia and a test of equal spin temperature, NIM A 419 (1) (1998) 60 .  
*Cited on pages 22 and 44.*

- [41] N. Takabayashi, Polarized target for the measurement of the gluon contribution to the nucleon spin in the COMPASS experiment, Ph.D. thesis, Nagoya University (2003).  
*Cited on page 22.*
- [42] K. Kurek et al., An algorithm for track reconstruction in the large angle spectrometer of the COMPASS experiment, NIM A 485 (3) (2002) 720 .  
*Cited on page 22.*
- [43] C. Bernet et al., The gaseous microstrip detector Micromegas for the high-luminosity COMPASS experiment at CERN, NIM A 536 (1–2) (2005) 61 .  
*Cited on page 25.*
- [44] B. Ketzer et al., Triple GEM tracking detectors for COMPASS, Nuclear Science, IEEE Transactions on 49 (5) (2002) 2403.  
*Cited on page 25.*
- [45] V. Bychkov et al., The large size straw drift chambers of the COMPASS experiment, NIM A 556 (1) (2006) 66 .  
*Cited on page 26.*
- [46] P. Abbon et al., The COMPASS setup for physics with hadron beams, to be submitted to: NIM A (2014).  
*Cited on page 27.*
- [47] C. Bernet et al., The COMPASS trigger system for muon scattering, NIM A 550 (1–2) (2005) 217 .  
*Cited on page 27.*
- [48] A. Akhundov et al., Contribution of electromagnetic production of lepton pairs to inclusive cross-section of deep inelastic  $\mu p$  scattering, Sov. J. Nucl. Phys. 32 (1980) 234.  
*Cited on page 41.*
- [49] B. Adeva et al., Erratum: Spin asymmetries  $A_1$  of the proton and the deuteron in the low  $x$  and low  $Q^2$  region from polarized high energy muon scattering [Phys. Rev. D 60, 072004 (1999)], Phys. Rev. D 62 (2000) 079902.  
*Cited on page 42.*
- [50] K. Gustafsson, Computation of the dilution factor for the year 2002 COMPASS data, Tech. rep., COMPASS (2003).  
*Cited on page 42.*
- [51] K. Abe et al., Measurements of  $R = \sigma_L/\sigma_T$  for  $0.03 < x < 0.1$  and fit to world data, Phys. Lett. B 452 (1999) 513.  
*Cited on pages 42, 53, and 61.*
- [52] J.-M. Le Goff, Asymmetry extraction, Tech. rep., COMPASS (2004).  
*Cited on page 42.*
- [53] J. Pretz, A new method for Asymmetry Extraction, Tech. rep., COMPASS (2004).  
*Cited on page 42.*
- [54] I. Akushevich et al., POLRAD 2.0 Fortran code for the radiative corrections calculation to deep inelastic scattering of polarized particles, Computer Physics Communications 104 (1997) 201.  
*Cited on page 43.*

- [55] O. A. Rondon, Corrections to nucleon spin structure asymmetries measured on nuclear polarized targets, *Physical Review C* 60 (1999) 227.  
*Cited on page 44.*
- [56] G. Ingelman et al., LEPTO 6.5 — A Monte-Carlo generator for deep inelastic lepton-nucleon scattering, *Computer Physics Communications* 101 (1–2) (1997) 108 .  
*Cited on page 45.*
- [57] GEANT: Detector description and simulation tool (1994).  
*Cited on page 45.*
- [58] B. Adeva et al., Spin asymmetries  $A_1$  and structure functions  $g_1$  of the proton and the deuteron from polarized high energy muon scattering, *Phys. Rev. D* 58 (1998) 112001.  
*Cited on pages 47, 58, 61, 64, and 67.*
- [59] L. Gatignon, Private communication.  
*Cited on page 53.*
- [60] J. Koivuniemi et al., Longitudinal polarization 2011, Tech. rep., COMPASS (2013).  
*Cited on page 53.*
- [61] J. Koivuniemi et al., Target material data of run 2011, Tech. rep., COMPASS (2012).  
*Cited on page 53.*
- [62] SLAC E155 Collaboration, Precision measurement of the proton and deuteron spin structure functions  $g_2$  and asymmetries  $A_2$ , *Phys.Lett.B* 553 (2003) 18.  
*Cited on page 54.*
- [63] M. Grosse Perdekamp, Measurement of the proton structure function  $g_1^p$ , Ph.D. thesis, University of California, Los Angeles (1995).  
*Cited on page 58.*
- [64] B. Adeva et al., Next-to-leading order QCD analysis of the spin structure function  $g_1$ , *Phys. Rev. D* 58 (1998) 112002.  
*Cited on pages 63 and 65.*
- [65] V. Gribov et al., Deep inelastic  $ep$  scattering in perturbation theory, *Sov. J. Nucl. Phys.* 15 (1972) 438.  
*Cited on page 63.*
- [66] V. Gribov et al.,  $e^+e^-$  pair annihilation and deep inelastic  $ep$  scattering in perturbation theory, *Sov. J. Nucl. Phys.* 15 (1972) 675.  
*Cited on page 63.*
- [67] G. Altarelli et al., Asymptotic freedom in parton language , *Nucl. Phys. B* 126 (2) (1977) 298 .  
*Cited on page 63.*
- [68] Y. L. Dokshitzer, Calculation of the structure functions for deep inelastic scattering and  $e^+e^-$  annihilation by perturbation theory in quantum chromodynamics., *Sov. Phys. JETP* 46 (1977) 641.  
*Cited on page 63.*
- [69] V. Alexakhin et al., Spin asymmetry and the spin-dependent structure function of the deuteron at low values of  $x$  and  $Q^2$ , *Phys. Lett. B* 647 (5–6) (2007) 330 .  
*Cited on page 64.*

- [70] J. Kodaira et al., Quantum-chromodynamic effects in polarized electroproduction, Phys. Rev. D 20 (1979) 627.  
*Cited on page 64.*
- [71] J. Kodaira, QCD higher-order effects in polarized electroproduction: Flavour singlet coefficient functions, Nucl. Phys. B 165 (1) (1980) 129 .  
*Cited on page 64.*
- [72] R. Mertig et al., The calculation of the two-loop spin splitting functions  $P_{ij}^{(1)}(x)$ , Zeitschrift für Physik C Particles and Fields 70 (4) (1996) 637.  
*Cited on page 65.*
- [73] W. Vogelsang, The spin-dependent two-loop splitting functions , Nucl. Phys. B 475 (1–2) (1996) 47 .  
*Cited on page 65.*
- [74] T. N. Pham, Test of SU(3) symmetry in hyperon semileptonic decays, Phys. Rev. D 87 (2013) 016002.  
*Cited on page 65.*
- [75] A. Korzenev et al., QCD analysis of  $g_1^{p;d;n}$  including the COMPASS  $g_1^d$  measurements, Tech. rep., COMPASS (March 2005).  
*Cited on page 65.*
- [76] D. de Florian et al., Extraction of spin-dependent parton densities and their uncertainties, Phys. Rev. D 80 (2009) 034030.  
*Cited on pages 65, 75, 82, and 83.*
- [77] G. Altarelli et al., On positivity of parton distributions, Nucl. Phys. B 534 (1–2) (1998) 277 .  
*Cited on page 66.*
- [78] S. Forte et al., Polarized parton distributions from charged-current deep-inelastic scattering and future neutrino factories, Nucl. Phys. B 602 (3) (2001) 585 .  
*Cited on page 66.*
- [79] V. Andrieux et al., Spin asymmetry  $A_1^p$  and the spin structure function  $g_1^p$  in bins of  $x$  and  $Q^2$ , Tech. rep., COMPASS (Apr 2013).  
*Cited on page 67.*
- [80] P. L. Anthony et al., Deep inelastic scattering of polarized electrons by polarized  $^3\text{He}$  and the study of the neutron spin structure, Phys. Rev. D 54 (1996) 6620.  
*Cited on page 67.*
- [81] K. Abe et al., Measurements of the proton and deuteron spin structure functions  $g_1$  and  $g_2$ , Phys. Rev. D 58 (1998) 112003.  
*Cited on page 67.*
- [82] K. Abe et al., Precision determination of the neutron spin structure function  $g_1^n$ , Phys. Rev. Lett. 79 (1997) 26.  
*Cited on page 67.*
- [83] P. Anthony et al., Measurement of the deuteron spin structure function  $g_1^d(x)$  for  $1 \text{ (GeV}/c)^2 < Q^2 < 40 \text{ (GeV}/c)^2$ , Phys. Lett. B 463 (2–4) (1999) 339 .  
*Cited on page 67.*

- [84] P. Anthony et al., Measurements of the  $Q^2$ -dependence of the proton and neutron spin structure functions  $g_1^p$  and  $g_1^n$ , Phys. Lett. B 493 (1–2) (2000) 19 .  
*Cited on page 67.*
- [85] A. Airapetian et al., Precise determination of the spin structure function  $g_1$  of the proton, deuteron, and neutron, Phys. Rev. D 75 (2007) 012007.  
*Cited on page 67.*
- [86] K. Ackerstaff et al., Measurement of the neutron spin structure function  $g_1^n$  with a polarized  $^3\text{He}$  internal target, Phys. Lett. B 404 (3–4) (1997) 383 .  
*Cited on page 67.*
- [87] X. Zheng et al., Precision measurement of the neutron spin asymmetry  $A_1$  and spin-flavor decomposition in the valence quark region, Phys. Rev. Lett. 92 (2004) 012004.  
*Cited on page 67.*
- [88] K. Dharmawardane et al., Measurement of the  $x$ - and  $Q^2$ -dependence of the asymmetry  $A_1$  on the nucleon, Phys. Lett. B 641 (1) (2006) 11 .  
*Cited on page 67.*
- [89] A. Martin et al., Uncertainties on  $\alpha_s$  in global PDF analyses and implications for predicted hadronic cross sections, The European Physical Journal C 64 (4) (2009) 653.  
*Cited on page 73.*
- [90] S. D. Bass et al., The nucleon's octet axial-charge  $g_A^{(8)}$  with chiral corrections, Phys. Lett. B 684 (4–5) (2010) 216 .  
*Cited on page 75.*
- [91] E. Ageev et al., Gluon polarization in the nucleon from quasi-real photoproduction of high- $p_T$  hadron pairs, Phys. Lett. B 633 (1) (2006) 25 .  
*Cited on pages 80 and 81.*
- [92] M. Stolarski, A new LO extraction of gluon polarisation from COMPASS DIS data, in: XXII Deep Inelastic Scattering, Warsaw, POLAND, University of Warsaw, 2014.  
*Cited on pages 80 and 81.*
- [93] A. Airapetian et al., Leading-Order determination of the gluon polarization from high- $p_T$  hadron electroproduction, JHEP 1008 (2010) 130.  
*Cited on pages 80 and 81.*
- [94] B. Adeva et al., Spin asymmetries for events with high  $p_T$  hadrons in DIS and an evaluation of the gluon polarization, Phys. Rev. D 70 (2004) 012002.  
*Cited on pages 80 and 81.*
- [95] E. Leader et al., Determination of polarized parton densities from a QCD analysis of inclusive and semi-inclusive deep inelastic scattering data, Phys. Rev. D 82 (2010) 114018.  
*Cited on pages 81, 82, and 83.*
- [96] D. de Florian et al., Evidence for polarization of gluons in the proton, Phys. Rev. Lett. 113 (2014) 012001.  
*Cited on pages 81, 82, and 83.*
- [97] E. R. Nocera, Unbiased spin-dependent parton distribution functions, [arXiv:hep-ph/1403.0440] .  
*Cited on pages 81, 82, and 83.*

- 
- [98] E. R. Nocera et al., A first unbiased global determination of polarized PDFs and their uncertainties, [arXiv:hep-ph/1406.5539] .  
*Cited on page 83.*
- [99] D. Stamenov, Private communication.  
*Cited on page 83.*
- [100] S. Larin et al., The  $\alpha_s^3$  approximation of quantum chromodynamics to the Ellis-Jaffe sum rule, Phys. Lett. B 404 (1–2) (1997) 153.  
*Cited on page 87.*
- [101] E. Leader et al., Impact of CLAS and COMPASS data on polarized parton densities and higher twist, Phys. Rev. D 75 (2007) 074027.  
*Cited on page 89.*
- [102] J. Blümlein et al., QCD analysis of polarized deep-inelastic scattering data and parton distributions, Nucl. Phys. B 636 (1–2) (2002) 225 .  
*Cited on page 89.*
- [103] D. de Florian et al., Sea quark and gluon polarization in the nucleon at NLO accuracy, Phys. Rev. D 71 (2005) 094018.  
*Cited on page 89.*
- [104] M. Glück et al., Models for the polarized parton distributions of the nucleon, Phys. Rev. D 63 (2001) 094005.  
*Cited on page 89.*
- [105] Y. Goto et al., Polarized parton distribution functions in the nucleon, Phys. Rev. D 62 (2000) 034017.  
*Cited on page 89.*
- [106] A. Deur et al., High precision determination of the  $Q^2$ -evolution of the Bjorken Sum, [arXiv:nucl-ex/1405.7854v3] .  
*Cited on page 89.*

# Appendix A

## Influence of $F_1$ on NLO QCD fit

Two different ways of treating the CLAS data in the fit were tried by using the published values of either  $g_1$  or  $(g_1/F_1)$  to evaluate the impact of  $F_1$  parametrisation. Similar results are obtained in both cases for all distributions but the gluon  $\Delta g(x)$ . However, it is found that the impact is negligible given the accuracy to which the inclusive data constrain the  $\Delta g$  distribution, see Fig. A.1.

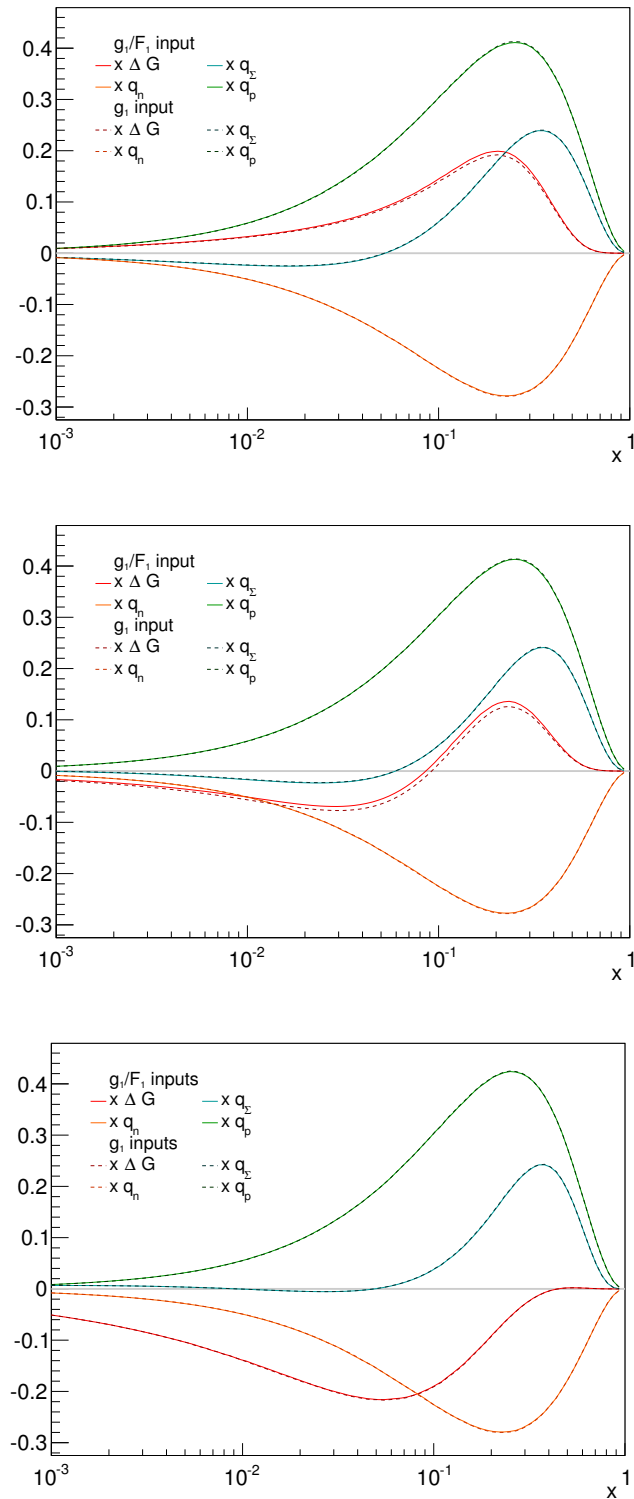


Figure A.1: Results from the NLO QCD fit when using  $g_1$  and  $F_1 \cdot (g_1/F_1)$  for the CLAS data for three sets of functional forms giving a positive  $\Delta G$  (ffP, top), a compatible  $\Delta G$  with zero (ff0, middle) and a negative  $\Delta G$  (ffN, bottom).

# Appendix B

## QCD fits parameters

parameters	$\Delta g(x) < 0$ (ffN)	$\Delta g(x)$ with a node (ff0)	$\Delta g(x) > 0$ (ffP)
$\eta_g$	$-0.669^{+0.122}_{-0.137}$	$-0.135^{+0.191}_{-0.198}$	$0.267^{+0.086}_{-0.084}$
$\alpha_g$	$-0.119^{+0.150}_{-0.141}$	$0.175^{+0.277}_{-0.268}$	$2.001^{+0.584}_{-0.498}$
$\beta_g$	7.5*	7.5*	7.5*
$\gamma_g$	0*	$-6.512^{+1.473}_{-2.175}$	0*
$\eta_s$	$0.348^{+0.011}_{-0.010}$	$0.302^{+0.017}_{-0.017}$	$0.278^{+0.016}_{-0.016}$
$\alpha_s$	$1.789^{+0.167}_{-0.156}$	$-0.110^{+0.140}_{-0.118}$	$-0.298^{+0.087}_{-0.084}$
$\beta_s$	$3.985^{+0.279}_{-0.263}$	$3.175^{+0.237}_{-0.214}$	$2.910^{+0.189}_{-0.166}$
$\gamma_s$	0*	$-13.044^{+1.079}_{-1.183}$	$-13.064^{+1.001}_{-1.027}$
$\eta_3$	$F + D = 1.269^*$	$F + D = 1.269^*$	$F + D = 1.269^*$
$\alpha_3$	$-0.081^{+0.031}_{-0.030}$	$-0.106^{+0.031}_{-0.030}$	$-0.108^{+0.031}_{-0.030}$
$\beta_3$	$2.193^{+0.104}_{-0.102}$	$2.170^{+0.104}_{-0.101}$	$2.170^{+0.104}_{-0.101}$
$\eta_8$	$3F - D = 0.587^*$	$3F - D = 0.587^*$	$3F - D = 0.587^*$
$\alpha_8$	$0.581^{+0.153}_{-0.149}$	$0.405^{+0.181}_{-0.311}$	$0.351^{+0.184}_{-0.306}$
$\beta_8$	$3.125^{+0.441}_{-0.418}$	$2.785^{+0.476}_{-0.653}$	$2.645^{+0.465}_{-0.627}$
$\chi^2/ndf$	692.4/652	675.5/650	681.9/651

Table B.1: Parameters of the NLO QCD fits defined at 1 (GeV/c)<sup>2</sup> for the three functional forms. The parameters marked with an asterisk are fixed. The errors on the parameters have been determined by MINOS with  $\Delta\chi^2=1$ . However these errors are not the ones considered in physics discussions.





## Résumé :

Cette thèse présente un travail relatif à l'étude de la structure en *spin* longitudinal du nucléon. Le but est de déterminer la contribution des constituants du proton, quarks et gluons, à la formation de son *spin* 1/2. L'analyse s'appuie sur les données de l'expérience COMPASS qui bénéficie d'un faisceau de muons polarisés à 200 GeV diffusé sur les protons polarisés d'une cible d'ammoniac ( $\text{NH}_3$ ) de 1,2 m de long. On mesure l'asymétrie de *spin* longitudinal des sections efficaces de diffusion profondément inélastique. On extrait la fonction de structure en *spin* du proton,  $g_1^p$ , étendant la couverture cinématique mondiale à des régions inexplorées jusqu'à maintenant ( $0,0036 \leq \langle x \rangle \leq 0,57$ ;  $1,03 \leq \langle Q^2 \rangle / (\text{GeV}/c)^2 \leq 96$  et  $23 \leq \langle W^2 \rangle / (\text{GeV}/c)^2 \leq 320$ ).

Les résultats, d'une grande précision statistique, sont inclus dans une analyse des données mondiales de  $g_1^p$ ,  $g_1^d$  and  $g_1^n$  (proton, deutéron et neutron) au 2<sup>ème</sup> ordre de QCD afin de paramétrer les distributions de quarks et de gluons polarisés. L'étendue de la couverture cinématique en  $x$  et  $Q^2$  des données mondiales de  $g_1$ , un élément déterminant pour la sensibilité à la polarisation des gluons  $\Delta G$ , s'avère trop limitée pour constituer une extraction précise de celle-ci. Néanmoins, l'analyse QCD permet de déterminer la contribution du *spin* des quarks au *spin* du proton à  $0.26 < \Delta\Sigma < 0.33$  à  $\langle Q^2 \rangle = 3$   $(\text{GeV}/c)^2$  dans le schéma  $\overline{\text{MS}}$ . L'étude montre que l'incertitude principale sur  $\Delta\Sigma$  est liée au choix des formes fonctionnelles utilisées dans la régression des données. Enfin, la règle de somme de Bjorken, qui constitue un test de QCD, est vérifiée avec une précision de 9% en utilisant les données de COMPASS uniquement.

## Mots-clés :

Fonction de structure en *spin* du proton; Expérience COMPASS; Diffusion profondément inélastique; Faisceau polarisé; Cible polarisée; *Spin* longitudinal du nucléon; Régression au 2<sup>ème</sup> ordre de QCD; Polarisation des quarks et des gluons; Règle de somme de Bjorken.

## Abstract :

The work presented in this thesis is related to the study of the longitudinal spin structure of the nucleon. The aim is to determine the contribution to the spin 1/2 of the proton in terms of its constituents, quarks and gluons. The analysis is performed on the data taken with the COMPASS experiment, which benefits from a polarised muon beam at 200 GeV scattered off polarised protons from an ammonia target of 1.2 m long. The double longitudinal spin asymmetry of deep inelastic scattering cross-section. The spin-dependent structure function of the proton  $g_1^p$  is derived from these measurements, which extend the kinematic world coverage to unexplored region so far ( $0.0036 \leq \langle x \rangle \leq 0.57$ ,  $1.03 \leq \langle Q^2 \rangle / (\text{GeV}/c)^2 \leq 96$  and  $23 \leq \langle W^2 \rangle / (\text{GeV}/c)^2 \leq 320$ ).

The results obtained with a high statistical precision are included in a Next-to-Leading order QCD analysis of world  $g_1^p$ ,  $g_1^d$  and  $g_1^n$  (proton, deuteron and neutron) data to parametrise the polarised quark and gluon distributions. The  $g_1$  world coverage of the  $x$  and  $Q^2$  kinematic domain, which is a key point in the sensitivity to the gluon polarisation  $\Delta G$ , turns out to be too limited for an accurate  $\Delta G$  determination. Nevertheless, the QCD analysis allows to determine the quark spin contributions to the proton spin to  $0.26 < \Delta\Sigma < 0.33$  at  $\langle Q^2 \rangle = 3$   $(\text{GeV}/c)^2$  in the  $\overline{\text{MS}}$  scheme. The dominant uncertainty on  $\Delta\Sigma$  is related to the choice of functional forms assumed in the fit. Finally, the Bjorken sum rule, which constitutes a fundamental test of QCD, is verified on the COMPASS data alone with a precision of 9%.

## Keywords :

Spin-dependent structure function of the proton; COMPASS experiment; Deep inelastic scattering; Polarised beam; Polarised target; Longitudinally polarised nucleon; NLO QCD fit; Quark gluon polarisations; Bjorken sum rule;